The Thesis Committee for Esben Skjold Pedersen
Certifies that this is the approved version of the following Thesis:

Carbonate Factory Response and Recovery after Ocean Anoxic Event 1a, Pearsall Formation, Central Texas

APPROVED BY
SUPERVISING COMMITTEE:

Charles Kerans, Supervisor

Toti E. Larson, Co-Supervisor

Daniel O. Breecker

Carbonate Factory Response and Recovery after Ocean Anoxic Event 1a, Pearsall Formation, Central Texas

by

Esben Skjold Pedersen

Thesis

Presented to the Faculty of the Graduate School of

The University of Texas at Austin

in Partial Fulfillment

of the Requirements

for the Degree of

Master of Science in Geological Sciences

The University of Texas at Austin

August 2020

Dedication

To my parents for their endless support.

To my sister, aunt, and uncle for opening my eyes to the world of the geological sciences.

Acknowledgements

Firstly, I would like to thank my co-supervisors, Charlie Kerans and Toti Larson, for the opportunity to continue my education as a graduate student at the University of Texas at Austin, and their wisdom both within and outside of the realm of geoscience. I would also like to thank Dan Breecker for serving on my committee, and for his advice during my time at UT.

I am grateful to Equinor for investing in my research and education in the geological sciences while as a graduate student. I would like to thank Rob Forkner in particular, for his guidance and direction.

I would like to thank the Staff at the Bureau of Economic Geology, including Nathan Ivicic, Brandon Williamson, and Rudy Lucero for their help and problem solving in the core warehouse, especially during COVID-19 restrictions, and to Evan Sivil for his help with pXRF dataset acquisition and guidance. I also deeply appreciate the conversations I have shared with Kelly Hattori and Ben Smith, and the instruction that they have provided.

Thank you to all the students and researchers of RCRL and MSRL, both the individuals that I have been fortunate to overlap with during my term at UT as well as those who helped pave the way. Thank you for all the learning and instruction we have shared. The experiences I have gained are invaluable and I will cherish many memories of times in the field with you all.

Abstract

Carbonate Factory Response and Recovery after Ocean Anoxic Event 1a, Pearsall Formation, Central Texas

Esben Skjold Pedersen, M.S. Geo. Sci.

The University of Texas at Austin, 2020

Co-Supervisors: Charles Kerans and Toti Larson

Ocean Anoxic Events (OAEs) are major carbon cycle perturbations that occurred several times in the Mesozoic. OAEs are commonly found to have been caused by a combination of climatic warming and increased surface weathering delivering surface nutrients to the oceans. This feedback loop leads to the expansion of the oxygen minimum zone of the waterbody and increased influx of terrigenous material. The resultant dysoxic to euxinic conditions are thought to have played a prominent role in the suppression of the benthic carbonate factory and deposition of organic-rich mudstones. The establishment of these oceanographic conditions are postulated to have imparted a lasting effect on the deposition of stressed-carbonate facies during the recovery phase of OAEs. Major questions regarding OAE events remain, including the degree of variability in the impact that OAEs have on carbonate factories and the drivers for this variability, on both global and regional scales.

This study builds upon previous work and further investigates the regional Early Cretaceous (Aptian) OAE-1a signal that is recorded in the Pearsall Formation in Central

Texas, with a particular focus on the record of carbonate factory recovery observed in transects from the San Marcos Arch to the Pearsall Arch. Shoreline-proximal data include outcrops and 8 cores with 1530 ft of coverage. Distal cores include 7 subsurface exploration wells (total 1745 ft core) from the San Marcos Arch to the Pearsall Arch, a strike-parallel distance of 210 km. Physical characterization of stratigraphic data was paired with the multivariate statistical analysis of 10 pXRF datasets, involving Principal Component Analysis (PCA) segmentation, which led to the establishment of five end member chemofacies. These chemofacies allow for high-resolution identification of mineralogic variability across OAE-1a, including the documentation of pulses of terrigenous input as well as cycles of dysoxic to euxinic oceanographic conditions at a sub-lithofacies scale. When paired with the development and application of a deep learning neural network trained by a type-pXRF training dataset, this study outlines a new methodology that allows for the direct comparison of pXRF data across core control through a unified chemofacies schema. The oceanographic conditions identified with this workflow are then used to delineate oceanographic variability and pulses of terrigenous enrichment in association with the recovery from OAE-1a. The characterization of these geochemical processes is particularly relevant in the mudrock component of depositional systems, where biologic productivity, bottom-water redox conditions, and any subsequent diagenesis are critical determinants for the ultimate preservation of TOC in organic-rich shales. TOC rich shale intervals then create potential for an economical petroleum source rock and successive charge of either conventional or unconventional reservoirs.

The incidence of OAE-1a is found to be a fundamental driver of facies evolution and faunal composition in the three composite sequences studied: the James (Aptian) composite sequence, the Bexar (Aptian-Albian) composite sequence, and the Glen Rose composite sequence (Albian) (cf. Phelps et al., 2014). OAE-1 is coincident with the

drowning of the antecedent Sligo reef margin and deposition of the Pine Island Shale. This drowning event was a result of environmental stressors posed by the OAE and the resultant suppression of sedimentation rates on the platform as the carbonate factory was substantially weakened. Partial recovery of the carbonate factory from OAE-1a is expressed in the deposition of the Cow Creek Member before punctuation of deposition due to the subaerial exposure event at the top-James composite sequence boundary. A second phase of recovery is documented in the Bexar and Glen Rose composite sequences, including reef systems in the platform interior that are coeval with transgression and deposition of the Hensel Formation, as well as the progradation of Lower Glen Rose carbonates and the aggradation of microbial-coral-rudist bioherms in highstand depositional sequences of the Glen Rose Formation.

Recovery of the carbonate factory was fundamentally different between the San Marcos Arch and Pearsall Arch areas. Earliest recovery fauna in the Cow Creek Member is comprised of monospecific echinoid-mollusk packstones-grainstones in shoreline proximal settings and oyster-oncoid rudstones distally. Combined observations from pXRF data and the heightened prevalence of pyrite in oncoid cortices on the San Marcos Arch compared to the Pearsall area is interpreted to represent a higher degree of dysoxic and/or euxinic conditions on the San Marcos Arch. During later stages of recovery, the Cow Creek in the Pearsall Arch area is shown to have maintained healthier carbonate deposition in comparison to the San Marcos Arch, including the sustained deposition of reefal assemblages, such as the sequence of stromatoporoid boundstone present in the Tenneco Sirianni well. This combined core-outcrop framework demonstrates the superimposed regional variability inherent even in global carbon cycle perturbations such as OAE-1a, driven by the degree of shelf restriction, oceanographic circulation patterns, basin geometry, and the degree of terrigenous influx. The documented differences in

oceanographic conditions and carbonate factory recovery on the regional scale of OAE-1a will aid in better understanding the multi-scaled geochemical and environmental evolution associated with these events, and ultimately pushes towards the development of predictive concepts for future studies.

Table of Contents

List of Tables

List of Figures

Chapter 1: Introduction

INTRODUCTION

Ocean anoxic events (OAEs) are major carbon cycle perturbations that occurred multiple times in the Mesozoic. During the Cretaceous Period, submarine volcanism along mid-ocean ridges and the emplacement of large igneous provinces catalyzed dramatic oceanographic and climatic shifts in the carbon cycle (Larson, 1991; Frey et al., 2000; Jenkyns, 2010). These dramatic shifts in the carbon cycle were coined Oceanic Anoxic Events by Schlanger and Jenkyns (1976). There are a variety of geochemical processes that are characteristic of OAEs. While the initiating circumstance may vary, the events share a common gross positive feedback loop wherein following the initiation of a global warming trend, increasing pCO_2 levels leads to increased acidification of the oceans (due to dissolution of CO_2 and SO_2) and causes increased carbonate dissolution (Arthur et al., 1988; Jenkyns, 2010). Climatic warming then accelerates the hydrologic cycle, leading to increased surface water runoff and nutrient flux to the oceans, increasing surface water biologic productivity (Parente et al., 2008; Jenkyns, 2010). The expansion of the oxygen minimum zone leads to dysoxic to anoxic bottom-water conditions during deposition (Stramma et al., 2008). The combination of bottom-water redox conditions and heightened organic matter production can serve for enhanced levels of TOC entering the rock record. Euxinic bottom-water conditions are the most advanced OAE type-conditions and this terminology refers to anoxic conditions paired with the presence of free H_2S in the water column, which allows for pyrite fixation and the deposition of pyrite framboids (Berner, 1984; Raiswell and Berner 1985).

These events are most commonly associated with the shutdown of precursor benthic carbonate factories and followed by deposition of black shales - some of which are known economic source rocks (Schlager, 1981; Jenkyns, 2010). In Texas, OAE-related source intervals include the Pearsall Formation (OAE-1a through OAE-1b), the Eagle Ford Formation (OAE-2), and the Austin Chalk (OAE-3) (Lowery et al., 2014; Phelps et al., 2014, 2015) (Figure 1.1). Recovery of the benthic carbonate factory following OAEs sets up the potential for encapsulated source-reservoir play systems. Post-OAE Gulf of Mexico reservoirs are known to occur in shelf interior grainstone belts (Cow Creek or James member of the Pearsall Formation) and in association with patch reefs (e.g., Cow Creek Limestone, Bexar Shale, and lower Glen Rose formations) (Hull, 2011; Loucks and Bebout, 1984). While significant research has been done on identifying mechanisms that are responsible for the onset of OAEs, less work has been done on understanding how carbonate factories recover from these perturbations and the superimposed regional variability of that recovery process (Kump and Arthur, 1999; Méhay et al., 2009).

Unlike the onset of OAEs, which appear to be sharp, the recovery of the carbonate factory may be more gradual. Considering post-OAE recovery mechanisms, environmental conditions such as oxygenation will vary along the carbonate platform depending on depth, proximity to shoreline, and basin circulation patterns. Regional variability in shallow shelf oxygenation, nutrient influx, circulation patterns, and or temperature extremes may help explain the disparate carbonate deposition and evolution of fauna seen globally in the recovery phase of these synchronous anomalies. For example, restricted basins may experience relatively longer persistence of stressed fauna while well-circulated basins may be able to re-establish a healthy carbonate factory more quickly. Work documenting differences in oceanographic conditions and carbonate factory recovery on the regional scale of OAE-1a could aid in better understanding the multi-scaled geochemical and

environmental evolution associated with these events, and ultimately moves towards the development and application of predictive concepts that can be applied to other OAE events.

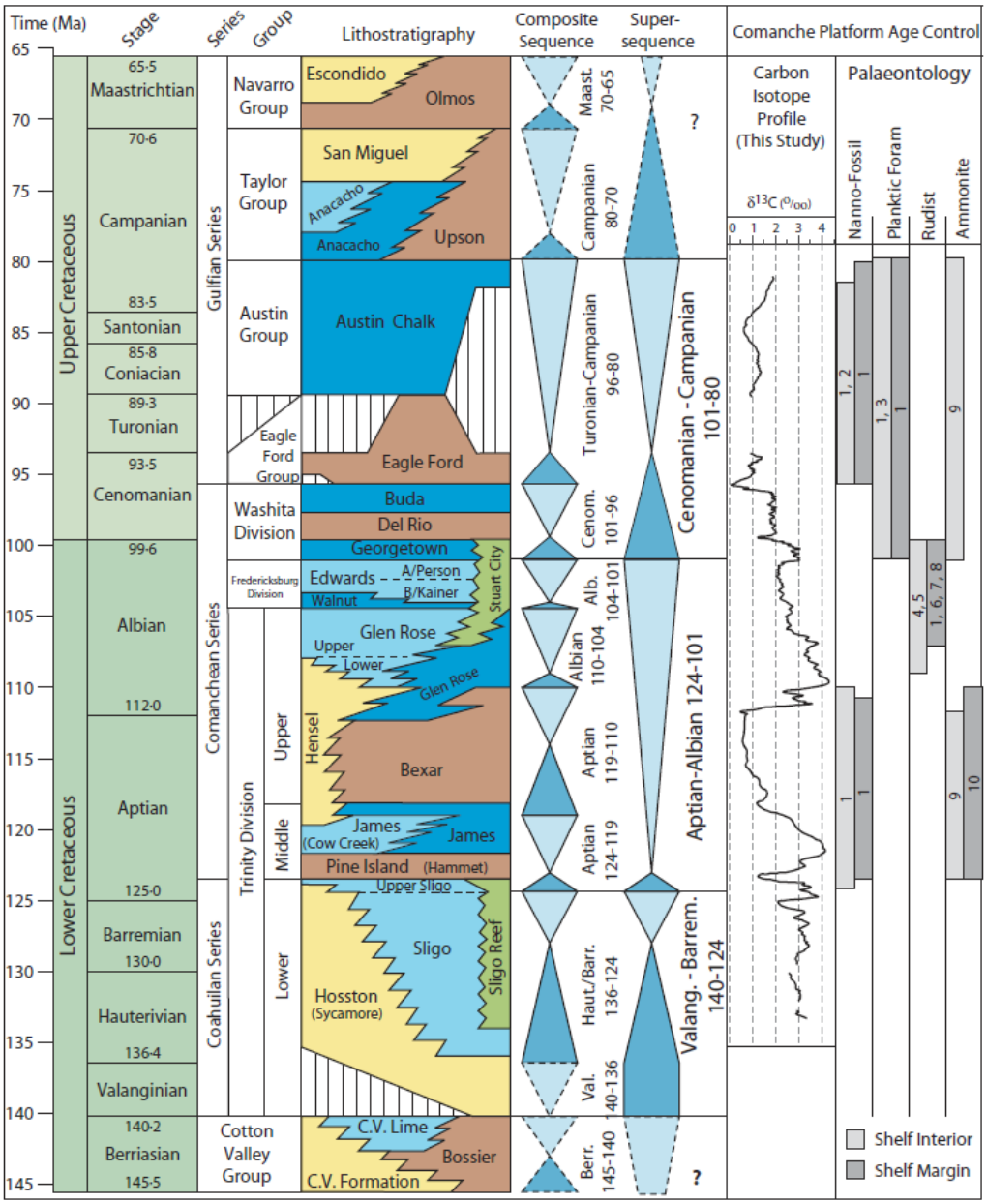

Figure 1.1: Stratigraphic column and carbonate - carbon isotopes of the Comanche Shelf. Includes definition of second-order composite sequences and their associated time-scales, and schematic lithostratigraphic unit relationships (To a first order: yellow = siliciclastics; brown = transgressive mudstones; blue = carbonates; green = platform margin reef systems) (Phelps et al., 2014).

OBJECTIVES

The primary goal of this study is to refine our understanding of the complex response and adaptation of the carbonate factory during major carbonate shutdown and recovery intervals initiated by OAEs. This study characterizes the lithofacies and chemofacies of carbonate deposition within the Pearsall Formation, and considers the superimposed eco-eustatic effects of OAEs on the resultant sequence stratigraphic framework of the Trinity Division (Figure 1.2). This work clarifies the stratal architecture of the Pearsall Formation and refines the timing of events from the preserved peak of the biotic crisis in the Pine Island Member during OAE-1a through the partial recovery phase recorded in the deposition of the Cow Creek Formation until the platform witnessed a second, albeit minor, biotic perturbation marked by OAE-1b in the Lower Glen Rose Formation. This work further aims to introduce a new method for interrogation of bulk elemental abundance pXRF data by multivariate statistical processing and the training of an artificial neural network which will allow for system-wide characterization of core data under a unified chemofacies classification scheme. This unified chemofacies classification overcomes a hurdle of previous pXRF applications, where the classification of chemofacies are generally specific to each well. A unified schema enables wholesale augmentation of the physical stratigraphic data to include inferences of the evolving oceanographic bottom-water conditions preserved in trace element concentrations. When combined, this integrative approach empowers observations between the San Marcos and Pearsall areas, and allows for comparisons to be drawn about the evolving carbonate factory recovery between the two localities.

STUDY AREA

The area of interest for this study extends across south-central Texas from the Pearsall Arch to the San Marcos Arch and north to the outcrop belt near Austin and Dripping Springs (Figure 1.2). The San Marcos Arch area has received the greatest attention to date and studies there have defined the geochemical trends of OAE-1a and OAE-1b along shelf transects (Phelps et al., 2014; Phelps et al., 2015; Forkner et al., 2019). The current study area is designed to connect the San Marcos Arch core control with the Pearsall Arch dataset, which has been observed as maintaining the healthiest carbonate factory across the OAE interval, with shoaling upward cycles in the Cow Creek capped by coral-stromatoporoid boundstones deposited in patch-reef complexes (Loucks, 1976; Loucks and Bebout, 1984). This shoreline-parallel transect allows for detailed facies mapping and improved understanding of the evolution of facies in the recovery interval both off-structure and onto shoaling environments found in the Pearsall Arch area (Hull, 2011).

The Pearsall/San Marcos area provides a unique window into the complex and evolving stratigraphy across Ocean Anoxic Event timelines, with several outcrops and borehole penetrations that allow for detailed characterization through integration of outcrop sections, well log correlations, and core characterization.

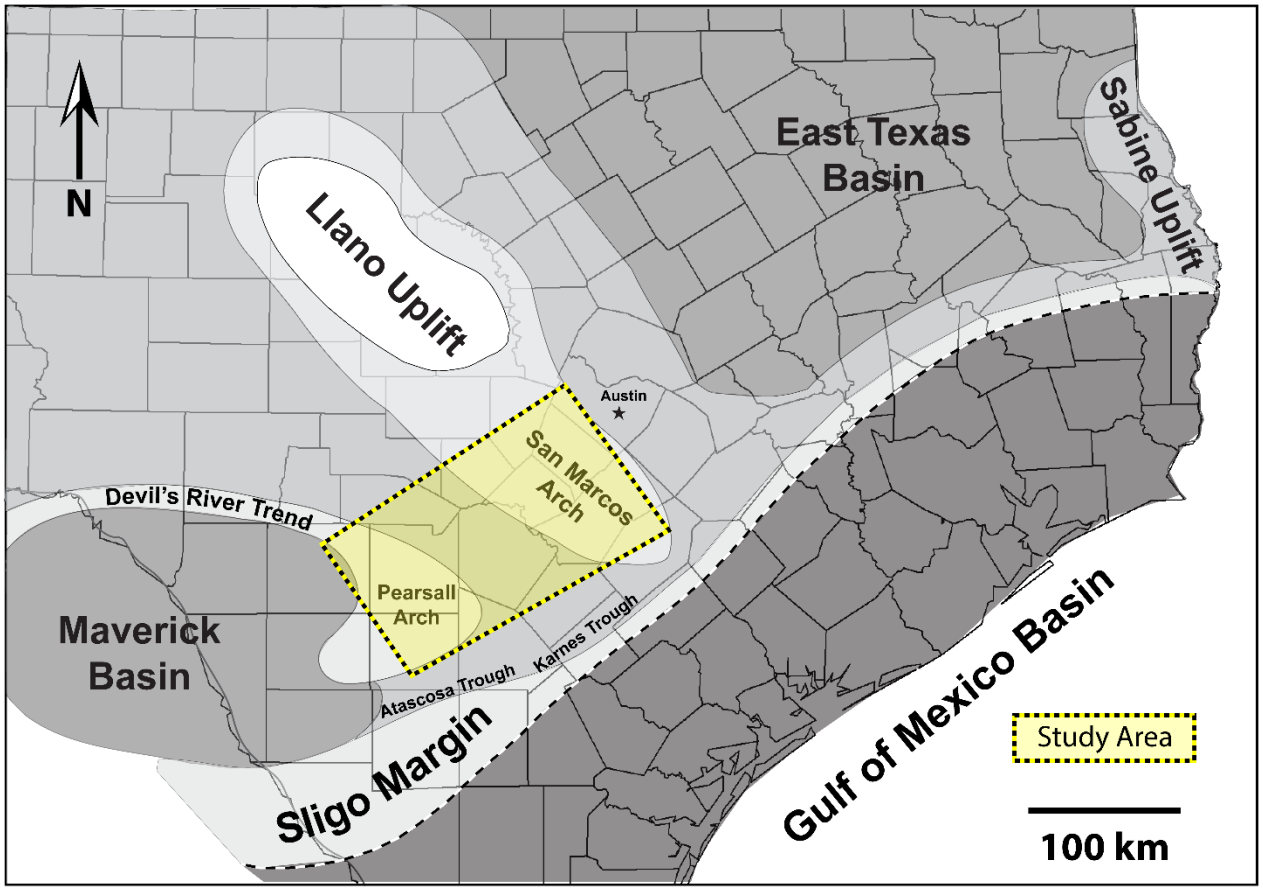

Figure 1.2: Regional map of the Comanche Shelf in Texas showing pertinent structural architecture. The area of interest for this study is highlighted in yellow (After Phelps, 2011).

METHODS, DATA, AND SAMPLING TECHNIQUES

Data for this investigation were acquired from outcrop, wireline, and core data (Figure 1.3). Stratigraphic data were selected to inform the regional facies architecture extending from the San Marcos Arch to the Pearsall Arch, and pXRF core data were selected based on available stratigraphic coverage to help develop our characterization of the complex geochemical signatures preserved in cored intervals.

Stratigraphic Data

Wireline logs available are similar to those reported by Hull (2011) and Phelps (2011) as few new wells have been drilled that penetrate the Pearsall Formation in the time since the publication of those reports. Most digital and raster wireline logs are SP-Resistivity logs. Core descriptions were used to compare lithology to wireline characteristics and to facilitate the development of a cross section with modeled facies relationships between core control.

Type	Number	Operator	Name	County
Outcrop	1	-	Pedernales Falls	Blanco
Outcrop	2	-	Sycamore Creek	Blanco
Outcrop	3	-	Reimers Ranch	Travis
Outcrop	4	-	Guadalupe River State Park	Kendall
Core	1	HTGCD	Hamilton Pool	Travis
Core	2	HTGCD	Skipton	Hays
Core	3	HTGCD	DSISD #1	Hays
Core	4	HTGCD	Old Hundred	Hays
Core	5	HTGCD	ESD Pump Station	Hays
Core	6	Shell	Narrows #2	Blanco
Core	7	GBRA	Guadalupe River Damsite 7-1	Kendall
Core	8	US Army Corps of Engineers	Canyon Dam	Comal
Core	9	Magnolia	Mercer	Caldwell
Core	10	Gulf Oil	Dix	Guadalupe
Core	11	Stanolid	Schmidt	Comal
Core	12	Tenneco	McKenzie #1	Wilson
Core	13	Tenneco	Suggs #1	Atascosa
Core	14	Tenneco	Climer #1	Atascosa
Core	15	Tenneco	Edgar #1	Frio
Core	16	Tenneco	Sirianni #1	Frio
Core	17	Tenneco	Goad #1	Frio
Wireline	1	Socony Mobil	Murphy P. Fullmann #1	Guadalupe
Wireline	2	Enre Corporation	Rainbolt J.D. Nixon	Guadalupe
Wireline	3	Murphy Baxter	Gorham Wildcat	Wilson
Wireline	4	Sohio Petroleum	Gayle U. Southern	Wilson
Wireline	5	Tenneco	Wilbeck #1	Frio
Wireline	6	Tenneco	Roberts #1	Frio
Wireline	7	Tenneco	Machen #1	Frio

Table 1.1: Stratigraphic data points and location. Numbers correspond to symbols on Figure 1.3.

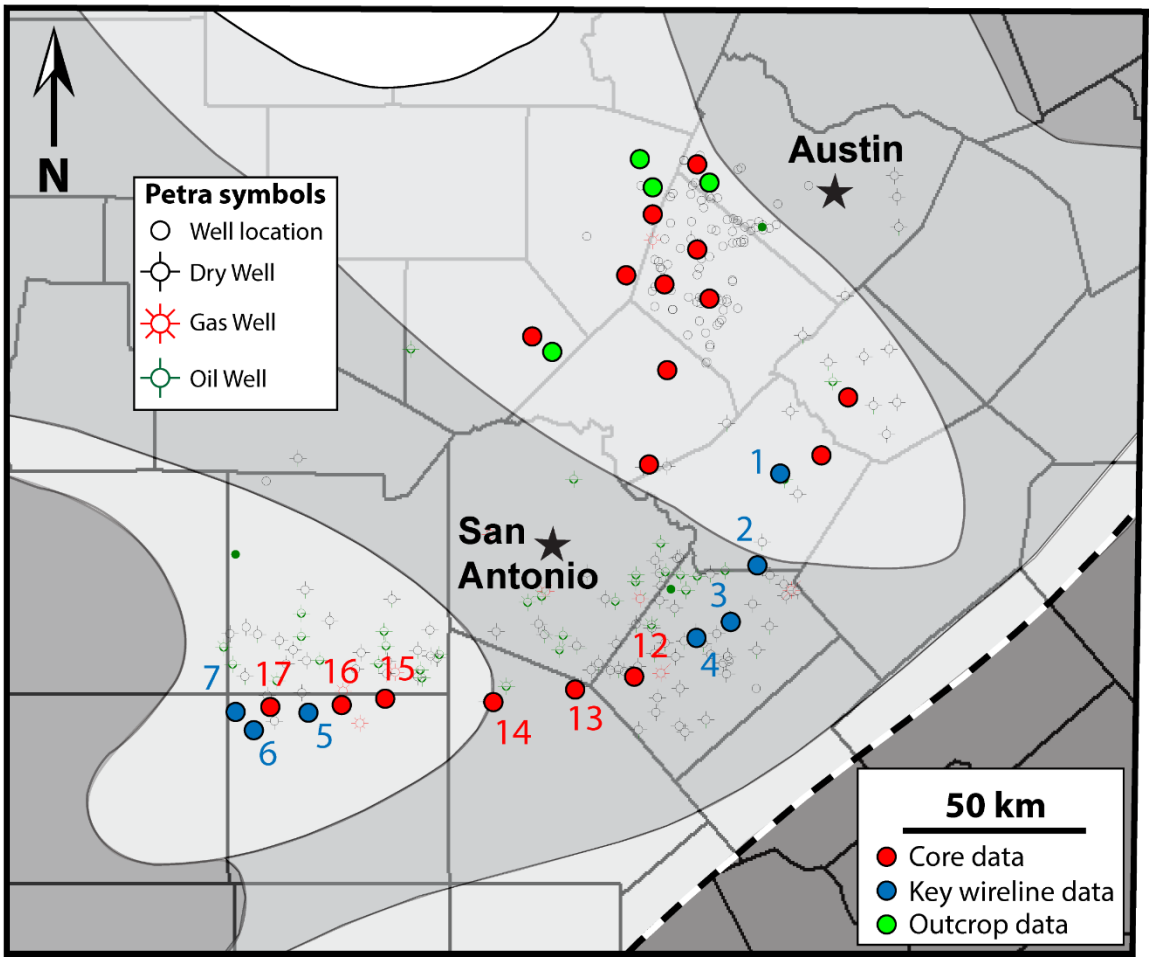

Figure 1.3: Map of South and Central Texas counties and the location of data available for this study. Supporting well logs and locations are denoted by native Petra well symbology.

Cores selected for this study are shown in Figure 1.3. Cores of interest are those that include stratigraphic intervals beginning with the upper Sligo through the lower Glen Rose formations near the San Marcos Arch and the Pearsall Arch (Table 1.1). A total of 1,241 additional feet of core were described for this study, which builds on a robust foundation of previous work to sum 4,834 total feet of core (described by the combined RCRL/STARR group) to develop this stratigraphic framework. Descriptions of new and re-described cores are integrated with previous core descriptions by Loucks (1976), Hull (2011), Phelps (2011), Playton, and Kerans. Core descriptions document lithofacies, sedimentary structures, visually estimated bulk mineralogy, faunal assemblages, and diagenetic features (Dunham, 1962). All cores described in this study are publicly available for viewing upon request and are in permanent collection at the Bureau of Economic Geology's core viewing facility in Austin, Texas. Outcrop measured sections and photogrammetry of the Cow Creek Member of the Pearsall Formation are located within state parks in Blanco, Travis, and Kendall counties (Figure 1.3; Table 1.1).

Approximately 155 petrographic thin-sections were studied to corroborate lithofacies allochem composition and rock fabric descriptions used in core descriptions, and to collect detailed data on facies and mineralogy.

X-Ray Fluorescence Data

Elemental concentration data were gathered using Bruker Tracer IV & V ED-XRF portable energy-dispersive X-ray fluorescence (pXRF) instruments. The cores were scanned in intervals of 5 cm (2 in) along the face of slabbed cores. Sample locations have been marked by small numbered stickers for spatial reference and posterity. In preparation, the surface of each slabbed core was scrubbed with a brush and warm tap water to remove any residue or buildup that may have been present. Such contaminants could include

surficial salts precipitated slowly over time in storage by brine residuum in the pore-space. After satisfactory surface preparation, the helium-purged pXRF instrument was pressed directly onto the face of the slabbed core at each marked interval (Figure 1.4). Major and trace elements were measured for 60 seconds, using excitation voltages of 15kV and 40kV, respectively. Trace element measurements were used in conjunction with 0.006-in Cu, 0.001-in Ti, and 0.012-in Al filters. Major elements included are: Na, Mg, Al, Si, P, S, K, Ca, Ti, Mn, and Fe. Trace elements included are: Co, Ni, Cu, Zn, Ga, As, Pb, Se, Th, Rb, U, Sr, Y, Zr, Nb, and Mo. Raw output data (% for major elements, and ppm for trace elements) was calibrated in accordance with the semi-quantitative methods outlined by Rowe et al., 2012. Cores with XRF data available for this study and their geographic locations are shown in Table 1.2 and Figure 1.5. XRF data used in this study is comprised of both new and pre-existing data that are the summation of the ever-growing suite of geochemical datasets available for the Cretaceous Northwestern Gulf of Mexico. Additional information on a well-by-well basis can be found in the appendix materials.

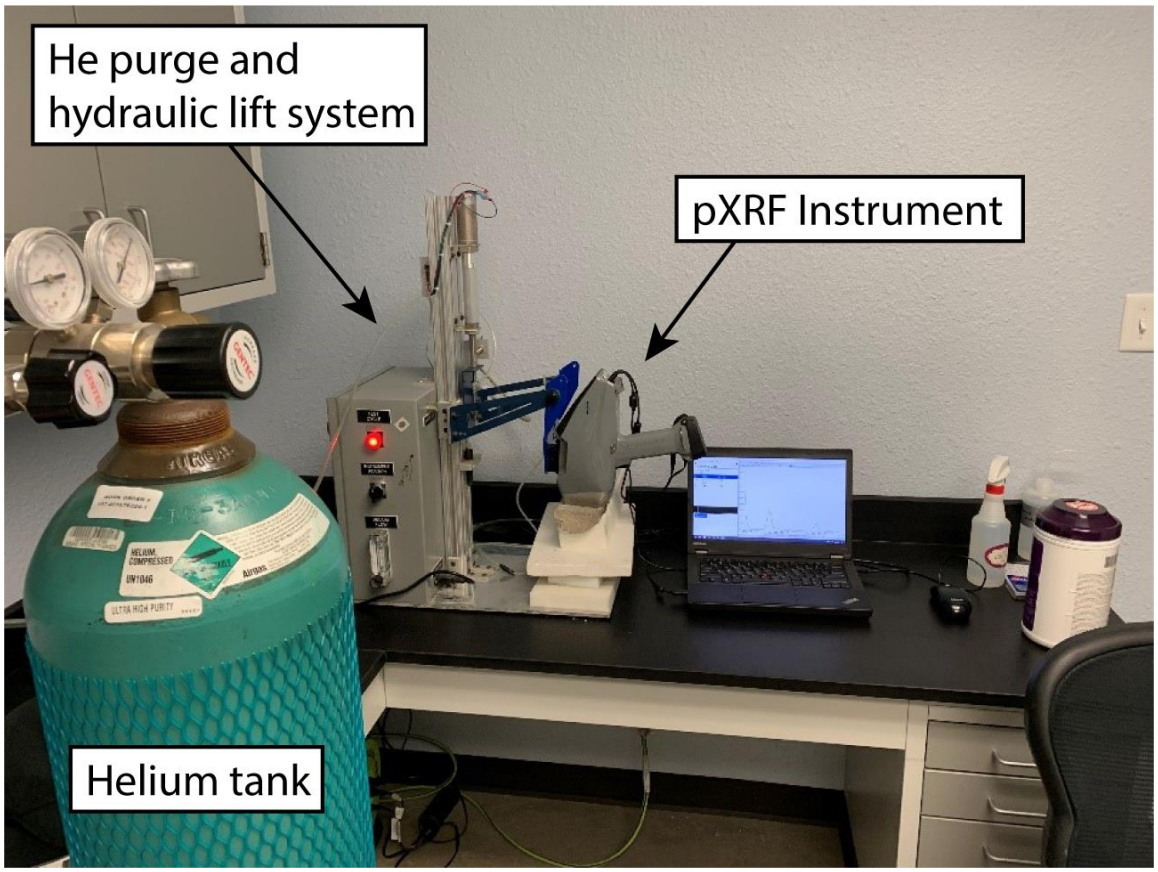

Figure 1.4: Laboratory pXRF setup utilizing the Bruker Tracer V ED-XRF instrument. Raw data is transmitted to the laptop as a live feed and saved for data storage.

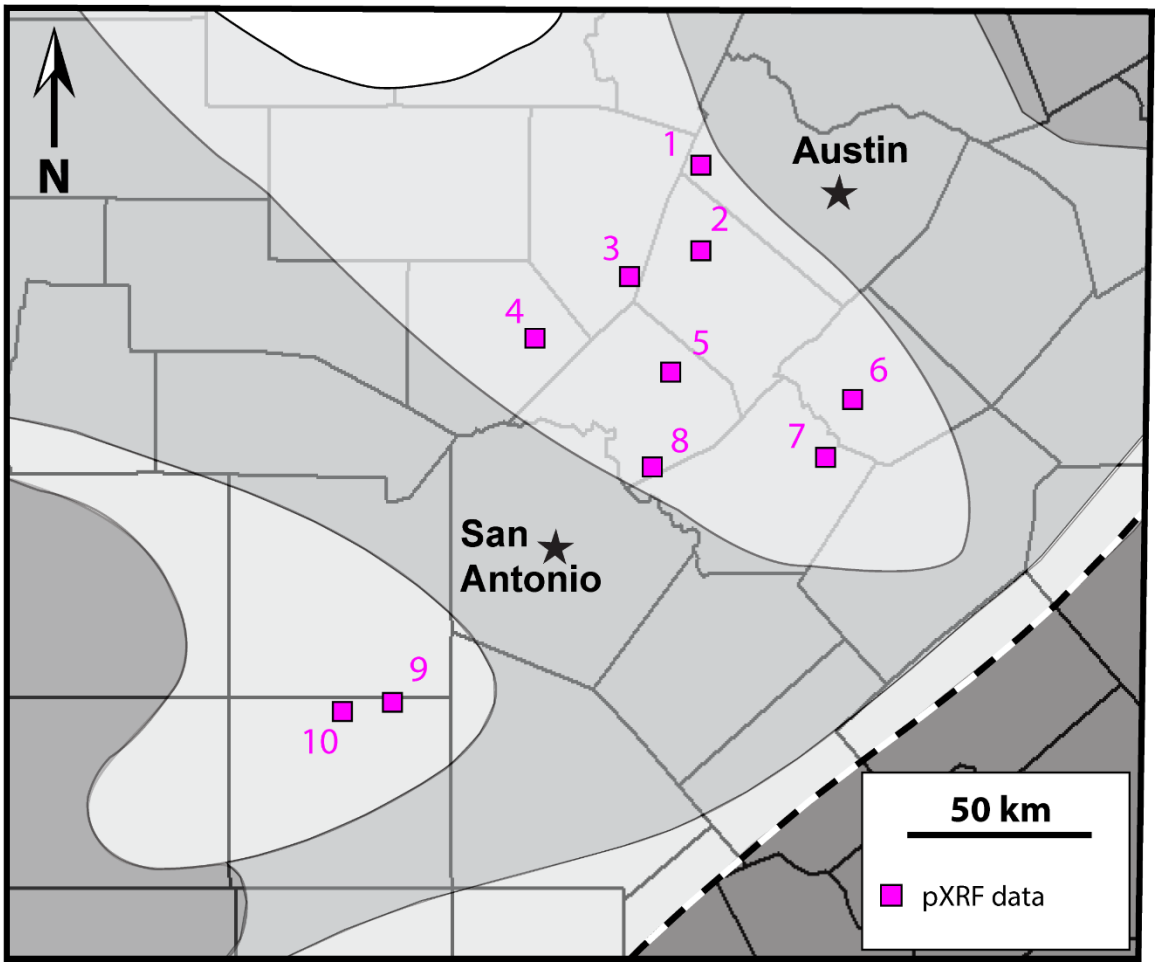

Figure 1.5: Map of available pXRF data used in this study. Numbers correspond to wells listed in Table 1.2.

Number	Well Name	County	Units characterized
1	Hamilton Pool	Travis	Pine Island, Cow Creek
2	DSISD #1	Hays	Cow Creek, Bexar, Lower Glen Rose
3	Narrows #2	Blanco	Pine Island, Cow Creek, Bexar, Lower Glen Rose
4	Guadalupe River Dam site 7-1	Kendall	Pine Island, Cow Creek, Bexar, Lower Glen Rose
5	Canyon Dam	Comal	Pine Island, Cow Creek, Bexar, Lower Glen Rose
6	Mercer	Caldwell	Pine Island, Cow Creek, Bexar, Lower Glen Rose
7	Dix	Guadalupe	Pine Island, Cow Creek, Bexar, Lower Glen Rose
8	Schmidt	Comal	Pine Island, Cow Creek, Bexar, Lower Glen Rose
9	Edgar	Frio	Cow Creek, Bexar, Lower Glen Rose
10	Sirianni	Frio	Cow Creek, Bexar, Lower Glen Rose

Table 1.2: Cores with pXRF data, and the intervals characterized. Numbers correspond to symbols in Figure 1.5.

Multivariate Statistical Analysis

This study includes the application of both supervised and unsupervised multivariate statistics, including Principal Component Analysis, k-means clustering, and multiple linear regression tools in order to identify and classify chemomineral facies. These tools, such as Principal Component Analysis (PCA), allow for the interrogation of large and complex datasets by mathematically reducing the initial dimensionality of a dataset to a series of principal components, which are new variables that describe the cumulative variance of the dataset (Pearson, 1901; Hotelling, 1933). The resultant groups from the k-means clustering of datapoints in PCA space are then classified as endmember chemomineral facies, hereafter referred to as chemofacies, which are units within the core that are observed to have similar major and trace element distributions. Chemofacies segmentation from a chosen type-well, based on continuity of data and the presence of all lithological units of interest, is then used to train a deep neural network (DNN) to enable the direct comparison of our established chemofacies across the remainder of core control within the study area. The methodology of the statistical tools used in this study and their applications, including the construction of the deep neural network are discussed in more detail in Chapter four.

The analysis highlighted in this work was accomplished by a developmental version of CorePy, a python toolkit featuring preparation and automated analysis of core imagery, pXRF data, and supplemental core data (e.g. TOC, rock mechanics etc.). CorePy is being developed in collaboration with Dr. Toti Larson and other Mudrock System Research Laboratory (MSRL) consortium researchers at The University of Texas at Austin's Bureau of Economic Geology (BEG). CorePy makes use of the open source machine learning library Scikit-learn (Pedregosa et al., 2011). See Appendix materials for more information and for a link to the GitHub repository for the most up to date public release of CorePy.

PREVIOUS WORK

This study builds upon a strong foundation of previous work conducted with both outcrop and subsurface data available in the northwestern Gulf of Mexico over the course of several decades. Many of these studies are listed in Table 1.3.

The stratigraphic framework for the Aptian-Albian section here has been made more challenging to interpret as a result of separation between outcrop and subsurface studies, and the preliminary lithostratigraphic definition and naming of units. The earliest research dealing with regional stratigraphy and depositional systems of the Cretaceous shelf/shelf margin in Texas began in the mid 1940's, with the designation of lithostratigraphic formations and the generation of regional subsurface cross sections used to demonstrate the Pearsall Formation (divided into three members: the lowermost Pine Island Shale Member, the Cow Creek Member, and the Bexar Shale Member) in the South Texas subsurface based on wireline signatures (Imlay, 1945). This work was followed in the 1950's by workers associated with Shell Oil, who conducted extensive outcrop-based studies investigating stratigraphic relationships in Central and North Texas (Lozo and Stricklin, 1956; Lozo et al., 1959; Lozo and Smith, 1964). The foundation of outcrop research led to further studies of both subsurface and outcrop nature (Stricklin et al., 1971; Perkins, 1974; Loucks, 1976; Bebout, 1977; Bebout and Loucks, 1977; Loucks, 1977; Bebout and Schatzinger, 1978; Bay, 1980; Inden and Moore, 1983). Later holistic re-examination resulted in the advancement of several more recent sequence stratigraphic interpretations (Amsbury, 1996; Moore, 1996; Kerans, 2002; Kerans and Loucks, 2002; Scott et al., 2002; Mancini and Ward, 2007; Ward and Ward, 2007). Some of the most recent work on the Comanche Platform has sought to provide a large scale compilation of the valuable foundational works of the many previous workers in a move towards the

wholesale translation of lithostratigraphic units into a uniformed sequence stratigraphic framework (Phelps et al., 2014; Phelps et al., 2015).

Regional Geologic Framework

The Cretaceous geology of south-central Texas is dominated by the long-lived Sligo and Comanche carbonate platforms, beginning in the Hauterivian, and persisting through the Albian (Figure 1.1). This study focuses on the Pearsall Formation of late Aptian age, which coincides with the maximum flooding surface of the James Composite sequence (124-119 Ma) linked to the carbonate platform "drowning event" spelling the end of the rudist-dominated, flat-topped Sligo carbonate platform (Phelps et al., 2014). Lithostratigraphically, the Pearsall Formation is comprised of the Pine Island (Hammett Shale in outcrop), Cow Creek, and Bexar members (Loucks, 1976) (Figure 1.1). The Pearsall Formation extends around the Gulf of Mexico, and nomenclature was determined regionally. In Mexico, the Pearsall is referred to as the La Peña Formation, and in East Texas, the Cow Creek member is known as the James Limestone.

Several structural events affected Pearsall deposition during the Aptian and Albian, beginning with emplacement of the Llano uplift of Precambrian age and the Ouchita Orogeny in the Carboniferous (Ewing, 2003). The proto-Gulf of Mexico began to open during the Jurassic, and paired with the counterclockwise rotation of the Yucatan and the connection of the Gulf of Mexico to the oceanic system by the Cretaceous established the framework for a flooded shelf and distal basin environments for carbonate deposition (Goldhammer and Johnson, 2001; Pindell and Kennan, 2001; Ewing, 2003; Ewing, 2010). Relative paleo-topographic highs of the San Marcos Arch and the Pearsall Arch allowed for the nucleation and accumulation of shallow water carbonate deposition upon the stabilized Ouachita basement, with accompanied clastic sedimentation sourced from the

exposed Llano uplift (Loucks, 1976; Goldhammer and Johnson, 2001). The San Marcos Arch area experienced relatively slowed subsidence rates throughout the Mesozoic (Loucks, 1976; Winkler and Buffler, 1988; Orgeron, 1995; Waite, 2009). Slowed subsidence of the Pearsall Arch paired with the increased subsidence of the adjacent Maverick Basin, as well as increased subsidence in the Atascosa and Karnes troughs led to the preservation of a local high in the Pearsall Arch Area during Pearsall Formation deposition (Loucks, 1976; Hull, 2011). Subsidence of the Maverick Basin center was controlled by salt withdrawal and an underlying Triassic-aged rift system (Ewing, 2003; Ewing, 2010; Hull, 2011). Structural elements following the deposition of the Pearsall Formation include the Balcones Fault Zone to the north, and Cenozoic growth faults outboard of the Sligo shelf margin to the south and east (Ewing, 2003).

Ocean Anoxic Events

During the peak OAE conditions, the benthic carbonate factory experiences acute suppression and carbonate sedimentation rates were drastically reduced (Li et al., 2008; Hull, 2011; Phelps et al., 2014). OAEs were capable of strongly influencing intervals of carbonate deposition due to the intrinsic sensitivity of carbonate systems to both physical sea level and chemical oceanographic controls (Follmi et al., 1994; Weissert et al., 1998). One example of the identification of the ecological impacts of OAEs is the marked disruption of the calcareous nannoplankton community ahead of peak OAE dysoxic conditions (Leckie et al., 2012). This “nannoconid crisis”, associated with OAE-1a, sees the overturn of planktonic abundances to favor those more well adapted to the eutrophic nutrient levels and excess CO_2 consistent with OAE-1a (Erba, 1994; Erba 2004; Erba et al., 2010).

Carbon isotope profiles are commonly used to correlate stratigraphic frameworks globally, so-called chemostratigraphy. Chemostratigraphy follows the premise that shifts of the carbon isotope composition of seawater across geologic timescales become incorporated into carbonate sediments or organic matter during deposition, effectively recording the $\delta^{13}C$ ratio of the seawater at the time of deposition (Jenkyns, 1995; Vahrenkamp, 1996; Huck et al., 2010; Vahrenkamp, 2010, Phelps 2015). The $\delta^{13}C$ records compiled by Phelps et al., (2015) show a significant and coeval excursion of greater than 2‰ across the latest Sligo platform coincident with global OAE-1a records and the emplacement of the Ontong-Java large igneous province (LIP) (Figure 1.6) (Bralower, 1999). These $\delta^{13}C$ excursions to more positive values reflect increased sequestration of isotopically light organic carbon during deposition of organic rich sediments that leaves the residual dissolved carbon pool of the ocean more enriched in the heavier ^{13}C isotope (Schangler and Jenkyns, 1976; Scholle and Arthur, 1980).

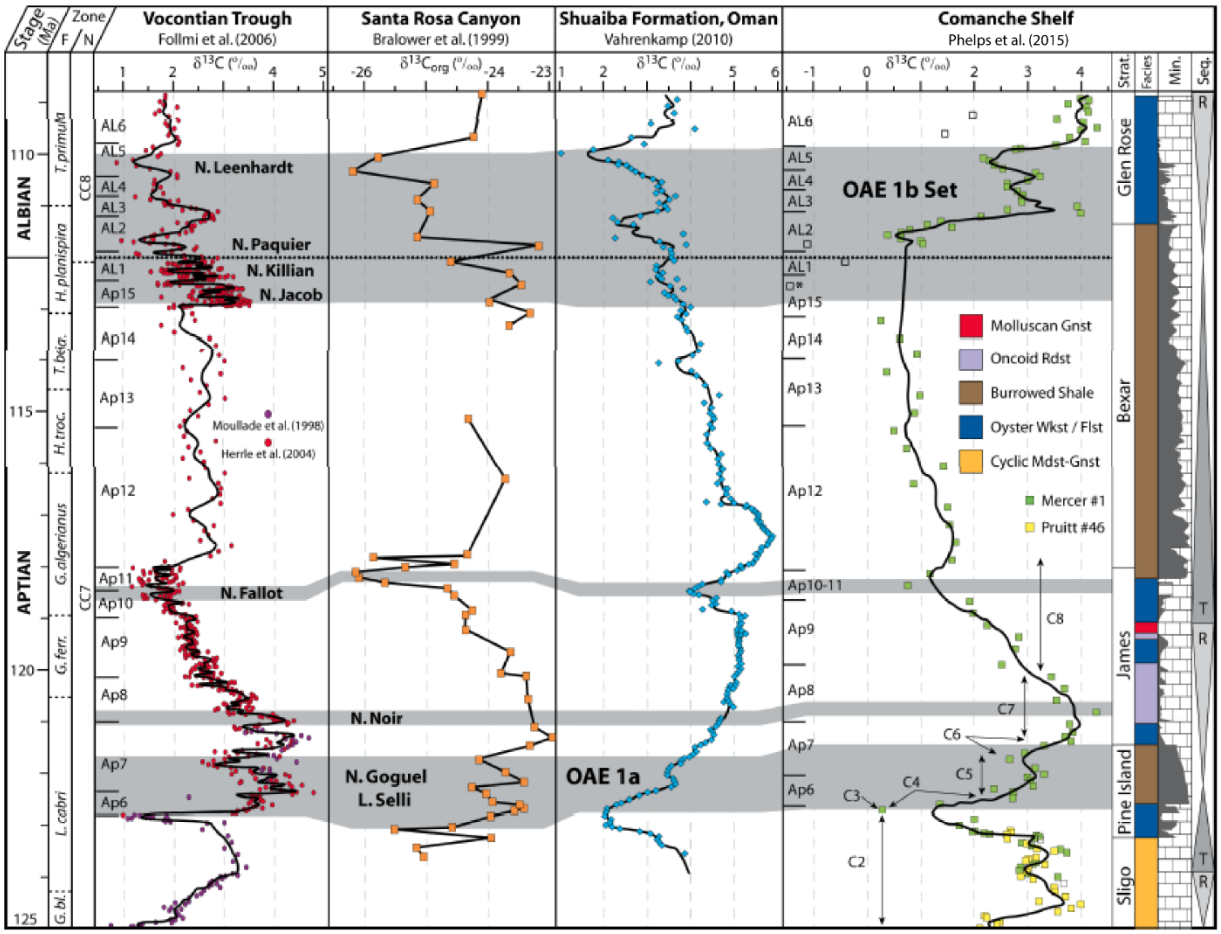

Figure 1.6: Correlation of Comanche Shelf $\delta^{13}C$ data to reference Aptian profiles (Figure modified from Phelps et al., 2015). Chemostratigraphic segments are from Menegatti et al. (1998) and Herrle et al. (2004).

Chapter 2: Regional Structure and Stratigraphy

SEQUENCE STRATIGRAPHIC ARCHITECTURE

Three transgressive-regressive (T-R) composite sequences (second-order) recognized in the Aptian and Albian portions of south and central Texas are termed the James, Bexar, and Glen Rose composite sequences, retaining nomenclature outlined in Phelps et al., (2014). The following sections in this chapter describe the characteristics of each delineated composite sequence. Internal characteristics discussed include the lithostratigraphic units involved, lithofacies distributions, stratal geometries, sequence boundaries, and the character of superimposed third order depositional sequences.

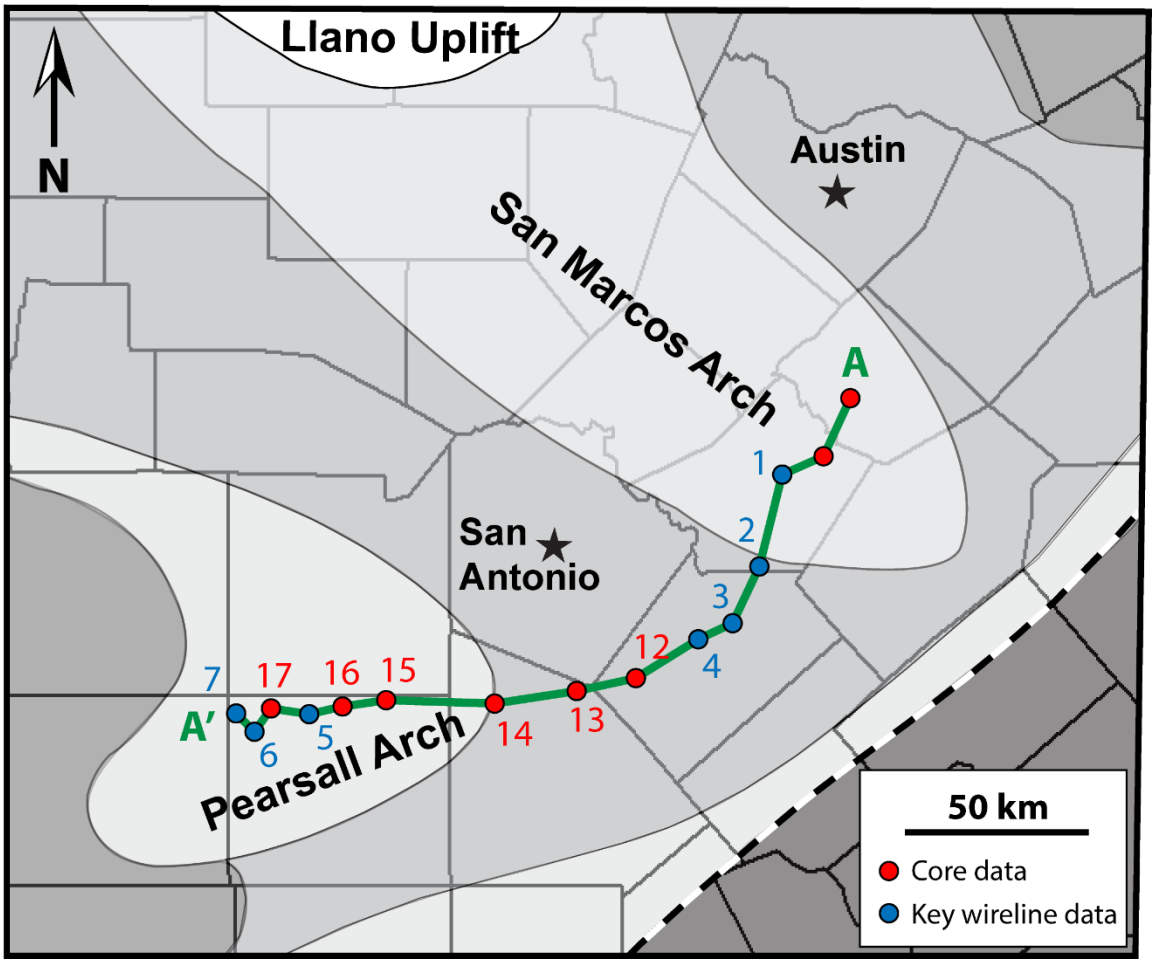

Figure 2.1: Map of cross section from the San Marcos Arch to the Pearsall Arch. Core control points are denoted in red; wireline control points are denoted in blue. Numbered data points refer to Table 1.1. Shading represents schematic relative paleotopography (darker = deeper).

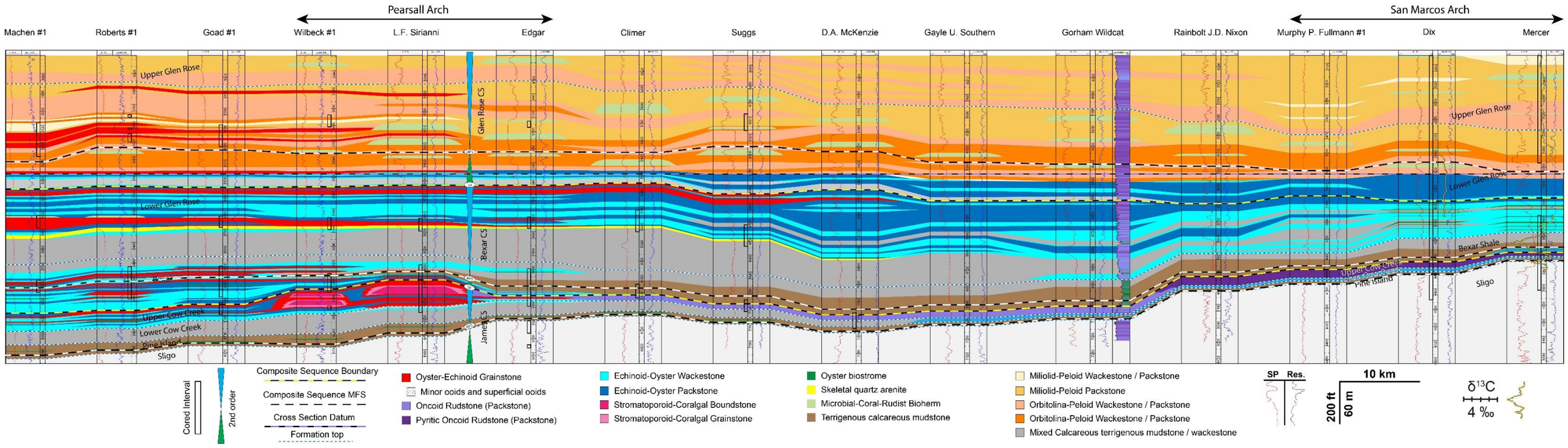

Figure 2.2: Regional cross section from the San Marcos Arch to the Pearsall Arch displaying Aptian and Albian stratigraphy. A Glen Rose marker is used as a datum to show the representative depositional architecture of the Pearsall Formation. The cross section was constructed using a combination of core control (outlines) and wireline logs. Facies projections away from well control are conceptual. ($\delta^{13}C$ data is after Phelps et al., 2015)

JAMES COMPOSITE SEQUENCE (EARLY TO MIDDLE APTIAN)

Lithostratigraphic units in the James composite sequence include the uppermost Sligo Formation, Pine Island Shale, and the Lower and Upper Cow Creek members of the Pearsall Formation (Figure 2.3). This early Aptian composite sequence captures roughly 5 million years of deposition, ranging from 124 to 119 Ma (Figure 1.1) (Phelps et al., 2014).

Transgression initiated with this composite sequence is noted by the onset of backstepping oolitic shoals of the upper Sligo Formation and the increase of carbonate mud in high frequency cycle (HFC) stacking patterns (Phelps et al., 2014). This sequence boundary was also noted by Goldhammer et al., (1991) and was put at the turn-around from progradation/aggradation (Cupido Fm.) to retrogradation (Cupidito Fm.). According to Phelps et al., (2014), unpublished seismic lines across the shelf-margin show initial aggregational reef geometries with younger reflectors onlapping and draping the reef-margin, which reveals an unsuccessful attempt of the reef margin to keep pace with the initial rise in relative sea-level prior the wholesale drowning of the reef-margin. The maximum flooding surface (MFS) of this composite sequence is located within the Pine Island Shale Member, coinciding with the heightened concentration of terrigenous mudstones and fissile shales relative to carbonate. In wells with cored intervals, the Pine Island Shale is commonly bagged or not recovered due to the fissile nature of the unit. Environmental stresses are likely to have played a prominent role in the Sligo reef-margin drowning event. Deposition of the following Pine Island Shale correlates with peak OAE-1a conditions recognized globally (Föllmi et al., 2006; Vahrenkamp, 2010; Phelps et al., 2015). Two third-order sequences within the James composite sequence are recognized and will be referred to here-after as the Aptian-10 and Aptian-20 sequences to maintain consistency with the framework outlined in Phelps et al., (2014). The Aptian-10

incorporates the uppermost Upper Sligo Formation, as well as the Pine Island and Lower Cow Creek Members of the Pearsall Formation. The uppermost ~15 meters of the Sligo Formation comprises the Transgressive Systems Tract (TST) of the third order sequence, followed by maximum flooding of the sequence that aligns with the MFS of the second order composite sequence. Following the blanketing of the carbonate platform by Pine Island shales, the transition upwards into the Lower Cow Creek member is gradual and transitional, with intercalated oyster rudstones and *Planolites*-burrowed mudstones. Upward coarsening seen in the Upper Cow Creek member is characterized by echinoid-mollusk shoreface facies in shoreline proximal wells, and an oncoidal rudstones distally. In some shoreline-proximal instances, the transition from the Lower Cow Creek to the Upper Cow Creek is sharp, representing high energy scouring processes associated with the progradation of the siliciclastic shoreface system back across the shelf. The Highstand Systems Tract (HST) of the Aptian-10 is associated with the first consistent carbonate-rich deposition following OAE-1a and is characterized by a monospecific faunal assemblage comprised of dominantly oyster and echinoid allochems. The Aptian-20 third-order sequence consists of the Upper Cow Creek Member and is characterized by initial TST deposition of echinoid-mollusk wackestones that interrupt the regressive molluscan shoreface clinoforms of the James-10 before the transition to HST and resumed progradation of molluscan shoreface clinoforms until regional depositional hiatus and exposure associated with the composite sequence boundary (Phelps et al., 2014). The sequence boundary at the top of the Upper Cow Creek member is characterized by a pronounced exposure surface and depositional hiatus expressed as karst dissolution pits and caliche profiles as well as marine hardground surfaces described in several cores and outcrop locations that cap the Cow Creek surface (Lozo et al., 1958; Inden & Moore, 1983; Kerans et al., 2014). An exposure surface of correlative age has been found to have been

associated with a relative sea-level drop on the order of 40 meters in the Eastern Tethys, based on seismic interpretations (Mauer et al., 2012; Bover-Arnal et al., 2014).

The HST of the James composite sequence differs between the San Marcos Arch and Pearsall Arch Areas. While both regions are characterized by echinoid-mollusk shoreface and shoaling facies updip and oncolite rudstones distally, the Pearsall Arch dataset also contains localized stromatoporoid-coralgal patch reefs, such as the interval penetrated by Tenneco #1 Sirianni in Frio County. Furthermore, the oncoids of the San Marcos Area are more highly pyritic than those of the Pearsall Arch area, pointing to the prolonged sediment-starved nature of the San Marcos Arch during this sequence in comparison to the Pearsall Arch area.

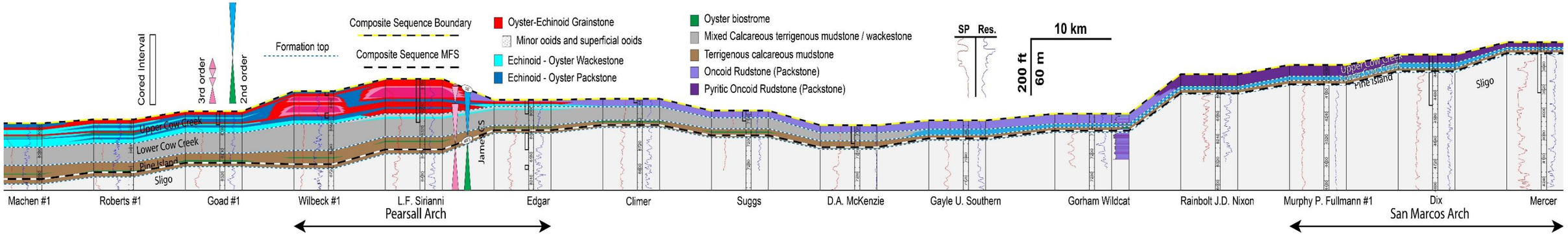

Figure 2.3: Regional sequence stratigraphic cross-section of the James composite sequence. The base of the cross-section does not extend to the bottom of the composite sequence due to a lack of core control. Facies projections away from well control are conceptual.

BEXAR COMPOSITE SEQUENCE (MIDDLE APTIAN TO EARLY ALBIAN)

Lithostratigraphic units found in the Bexar composite sequence include the Bexar Member of the Pearsall Formation, sandstones of the Hensel Formation, and the Lower Glen Rose Formation (Figure 2.4). This middle Aptian to early Albian composite sequence captures roughly 9 million years of deposition, ranging from 119 to 110 Ma (Figure 1.1).

Transgression of the Bexar Member once again blanketed the shelf with mudstones, with the deposition of an initial terrigenous shale followed by the transition into burrowed carbonate mudstones. Regression led to the slow increase in carbonate content as well as the increased interfingering of oyster rudstones, and eventually, the transition to echinoid-mollusk wackestones to packstones (Loucks, 1976; Hull, 2011). Recent re-identification of the OAE-1b signal by biomarker tracing and detailed nannofossil biostratigraphy has placed the OAE within this highstand, in the transition between the Bexar and the lowermost portion of the Glen Rose (Forkner et al., 2019). The OAE-1b is not characterized by the same enduring, platform-wide biotic crisis and deposition of mudrock noted for the OAE-1a in the James composite sequence. While collapses of nannoplankton abundances were identified and seem to be similar to such nannoplankton indicators for other OAEs (including OAE-1a), the environmental perturbation associated with OAE-1b was either limited in duration or severity, as shown in the explicit lithofacies stacking pattern across the OAE (Forkner et al., 2019).

Hensel Formation sandstones can be observed above the James composite sequence boundary and subaerial exposure surface, especially in shoreline proximal wells and outcrops such as Hamilton Pool and DSISD #1 (Figure 1.3; Appendix materials). The time-transgressive nature of the Hensel Formation records terrestrial to marginal marine deposition during the prolonged exposure of the Llano uplift, that was capable of

consistently supplying sediment across the shelf throughout the composite sequences. The Hensel Formation is the updip equivalent of the shoreline-equivalents of middle to outer ramp carbonates and mudstones of the Bexar composite sequence (Phelps et al., 2014).

Within the Bexar composite sequence, three third-order sequences have been identified, and will be referred to here-after as the Aptian-30, Aptian-40, and Aptian-50 sequences (Hull, 2011; Phelps et al., 2014). The identification of these third order sequences is difficult on the San Marcos Arch. These sequences are instead best resolved over the Pearsall Arch area. Some previous studies did not recognize the third order cyclicity presented in the Bexar composite sequence and instead included the Bexar Shale as a transgressive facies of Lower Glen Rose sequences (Scott, 1993; Mancini and Puckett, 2002; Mancini and Scott, 2006). In the Pearsall Arch area, these sequences are characterized by transgressive carbonate and terrigenous facies overlain by progradational shoal-water complexes (Loucks, 1976; Loucks and Bebout 1984, Hull, 2011). The Aptian-30 sequence is within the Bexar Member and is comprised of lower argillaceous lime wackestones and siliciclastic mudstones that are dominantly terrigenous and thin in the updip direction (Hull, 2011). The maximum flooding surface for the Aptian-30 sequence is located within the most dominantly terrigenous interval. The highstand of the sequence builds into a thin grainstone that progrades west into the Maverick Basin. The Aptian-40 sequence is similarly constrained by transgressive lithofacies at the base and a progradational shoal-water complex above. This shoal-water complex is dominantly located in Zavala County, where it progrades into the Maverick Basin (Hull, 2011). Aptian-50, the final Bexar third-order sequence, is composed of the uppermost Bexar Member and Lower Glen Rose. This sequence marks the transition from the more argillaceous and terrigenous Bexar into the cleaner carbonate mudstones and wackestones in the Lower

Glen Rose (Bay, 1980). This transitional interface is a gradational contact, similar to the contact between the Bexar and the Lower Glen Rose on the San Marcos Arch.

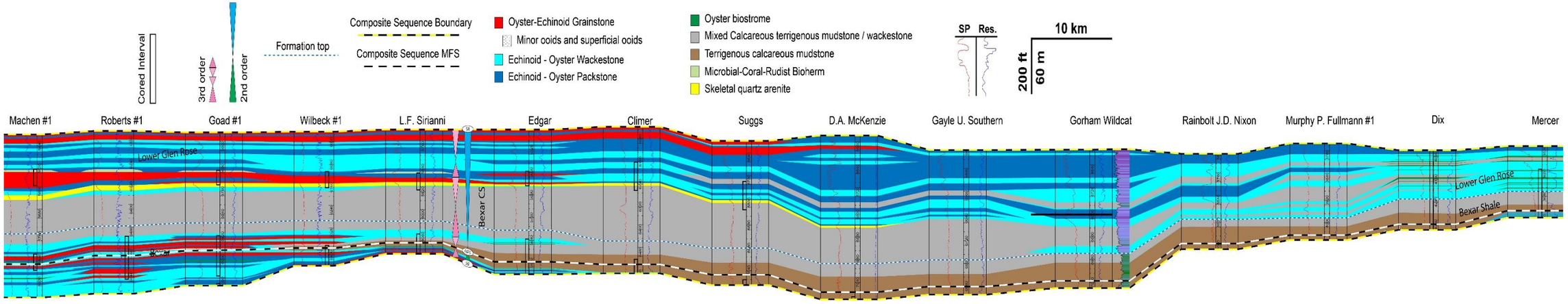

Figure 2.4: Regional sequence stratigraphic cross-section of the Bexar composite sequence. Facies projections away from well control are conceptual.

GLEN ROSE COMPOSITE SEQUENCE (EARLY ALBIAN TO MIDDLE ALBIAN)

Lithostratigraphic units found in the Glen Rose Composite sequence include Hensel Formation sandstones and Lower and Upper Members of the Glen Rose Formation (Figure 2.5). The full Glen Rose composite sequence ranges from the early to middle Albian, consisting of roughly 6 million years of deposition, ranging from 110 to 104 Ma (Figure 1.1). This study does not cover the full composite sequence, and instead investigates a partial Glen Rose composite sequence to describe the emergence of patch reef complexes in the Lower Glen Rose. This subdivision includes the Albian-10 and partial Albian-20 third order sequences. Division of the Lower and Upper Glen Rose members of the Glen Rose Formation is defined by a zone of *Eoursivivas harveyi* bivalves, coined as the "corbula zone" that splits the two members into roughly even thicknesses (Perkins, 1974; Stricklin et al., 1971; Stricklin and Amsbury, 1974; Scott et al., 2007; Ward and Ward, 2007). Aconcha (2008) offers a method of identification for the Maverick Basin wireline expression of a datum similar in depth to this "corbula zone" by the detection of a high density anhydrite layer that separates the more dolomitic Upper Glen Rose from the less dolomitic Lower Glen Rose. Below the "corbula zone" is a zone of *Salenia texana*, a small stirodont echinoid that is associated with the interpretation of the opening and deepening of the shelf by Perkins (1974). Due to the distally steepened ramp bathymetric profile inherited due to the substantial transgression of the shelf during James and Bexar composite sequences, facies patterns progressively shallow landwards from outer-ramp oncoid floatstone to middle-ramp cyclic subtidal shelf wackestone/packstone and, lastly, to inner-ramp peritidal sand flats and mud flats (Phelps et al., 2014). Miliolid bearing cyclic subtidal shelf facies indicate mildly restricted conditions while *Orbitolina* bearing facies indicate episodic transgression across the shelf during flooding events and are often associated with

the MFS of sequences (Phelps et al., 2014). The Albian-10 third order sequence is comprised of the Lower Glen Rose and extends slightly past the contact with the Upper Glen Rose, to a regional solution collapse breccia roughly 1 meter above the "corbula zone" (Phelps et al., 2014). Maximum flooding of the Albian-10 coincides with the composite sequence MFS and is located within a landward migration of *Orbitolina*-peloid wackestones and packstones (Phelps et al., 2014) (Figure 2.5). The location of this MFS places the majority of subsequent microbial-coral-rudist bioherms (Figure 2.5) within the early highstand systems tract, similar to the buildups described by Aconcha (2008) in the Maverick Basin, which are considered to be of correlative age. The Albian-20 third order sequence is comprised of the Upper Glen Rose above the "corbula zone" and solution collapse breccia. Similarly to the Albian-10, flooding packages in the Albian-20 are identified by the deposition of *Orbitolina*-peloid wackestones and packstones. The upper Albian-20 boundary is above the vertical extent of the cross section presented in this study. Middle ramp facies of the Albian-20 are commonly comprised of progradational, cyclic subtidal shelf packstones to grainstones, while monopleurid biostromes commonly form the late highstand of the sequence (Phelps et al., 2014).

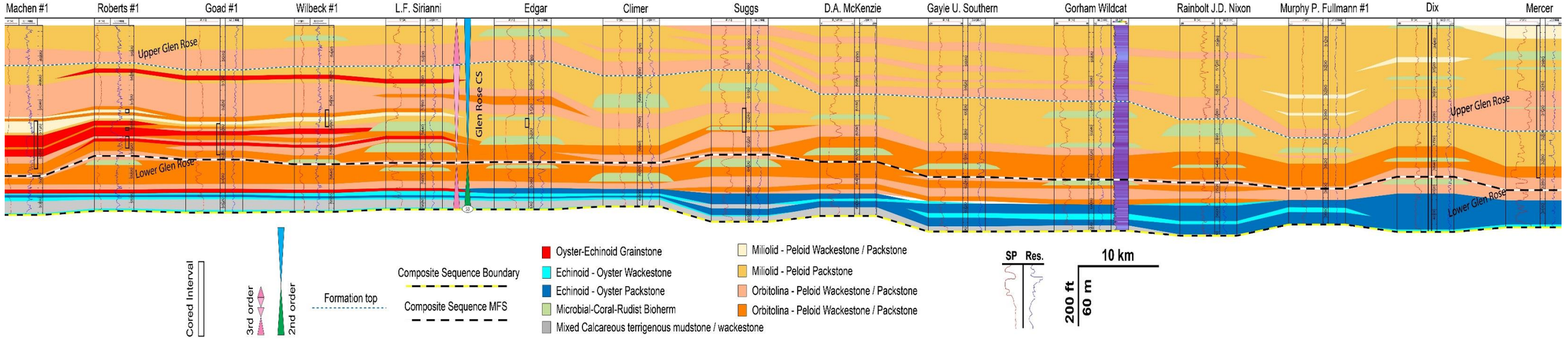

Figure 2.5: Regional sequence stratigraphic cross-section of the Glen Rose composite sequence. Facies projections away from well control are conceptual.

Chapter 3: Lithofacies Associations

General Statement

The 11 lithofacies associations outlined in this chapter are a generalized representation of the facies occurrences observed in the James, Bexar, and Glen Rose composite sequences. Additional detail and lithofacies analysis for the outer-ramp mudrock component of the Pearsall Formation can be found in Hull (2011).

OYSTER RUDSTONE (PACKSTONE)

The oyster rudstone facies forms correlative biostromes predominantly within the Pine Island and Bexar intervals (Loucks, 1976), as well as the Lower Glen Rose on the San Marcos Arch. These low diversity biostromes are found on the middle ramp of both the San Marcos Arch and Pearsall Arch (Phelps 2011; Hull 2011). This facies is characterized by the presence of large, and commonly disarticulated and fragmented oyster shells (> 5cm) (Figure 3.1). Some shells may be interpreted to be in living positions, but most appear to be transported, likely reworked by storms. The oyster rudstone facies exhibits low biodiversity and occurs in close association with OAE's 1a and 1b. The consistently monospecific fauna observed following peak OAE conditions points to the creation of a stressed ecological system, wherein predominantly oysters were able to adapt to the eutrophic and brackish water column.

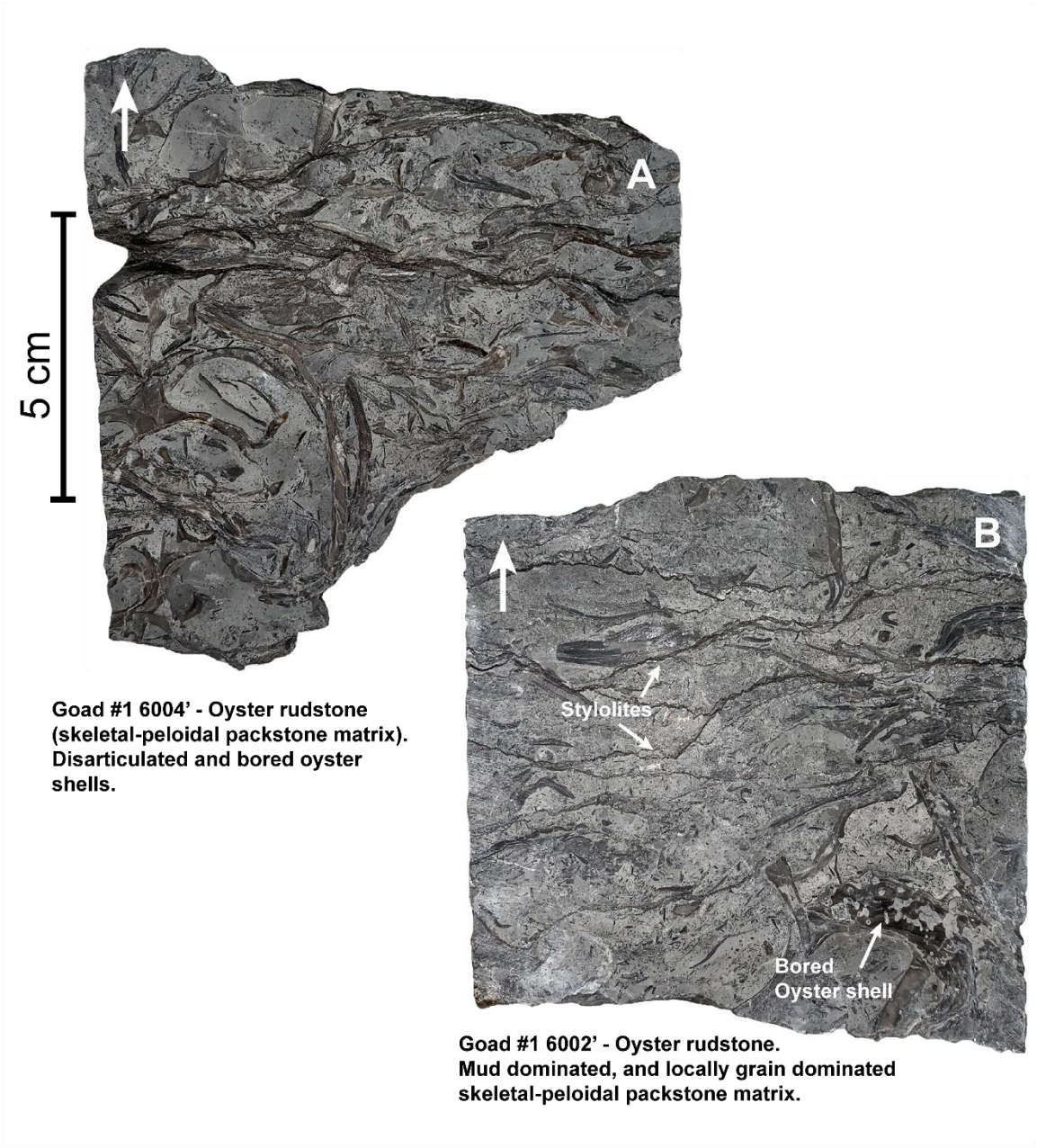

Figure 3.1: Oyster rudstone (packstone) facies plate.

ONCOID RUDSTONE (PACKSTONE)

The oncoid rudstone is found within the Lower and Upper Cow Creek Members of the Pearsall Formation in both the San Marcos Arch and the Pearsall Arch areas. Oncoid grains range from 2 to 5 millimeters in diameter, with irregular laminae sets consisting of several stages of erosion and subsequent accretion (Figure 3.2). The size of the coated grains appears to increase upwards towards the top of cycles, with coated grains in the sub-millimeter range generally displaying more circular and well laminated cortices. Quartz silt is commonly observed to be present within oncoid laminae, some of which is attributed to the degradation of encrusting foraminifera with the quartz as part of the agglutinated shell wall. Petrography reveals a complex faunal association within the oncoids, with oyster and echinoid fragments serving as nuclei, and encrusting foraminifera, worm tubes, and oysters attaching themselves to the exteriors of oncoid grains (Figure 3.2). The larger oncoids appear to have a greater degree of alteration from encrusting foraminifera etc., which is likely attributed to a longer growth period before final burial. Enhanced faunal transformation of oncoids, such as dense encrustation, is likely associated with accentuated depositional breaks allowing for sustained alteration in a firm-ground like setting (Wilson and Palmer, 1990; Taylor and Wilson, 2003).

Oncoid cortices also contain pyrite throughout (up to 10%), indicating periods of growth linked to reducing bottom-water conditions. The micritic matrix that surrounds the oncoids is notably lacking of pyrite, differentiating the matrix and the constituent coated grains as likely having been deposited under different oceanographic regimes. Furthermore, shelter cavities related to percolation of mud from the surface down through the oncoid grain frameworks is common throughout all thin sections analyzed. These observations indicate that the mud-matrix emplacement is from late infiltration, post-dating the reducing conditions experienced during oncolite accumulation. The matrix itself is

generally barren in terms of allochems, other than some microfauna such as what appear to be worm tubules. Compared with the pyritiferous oncolites of the San Marcos area, those of the Pearsall Arch are free of pyrite, suggesting a more consistently oxygenated setting. It is likely that the pyritiferous oncoids of the San Marcos Arch mark periods of sustained-to-cyclic periods of euxinia during Cow Creek Member deposition.

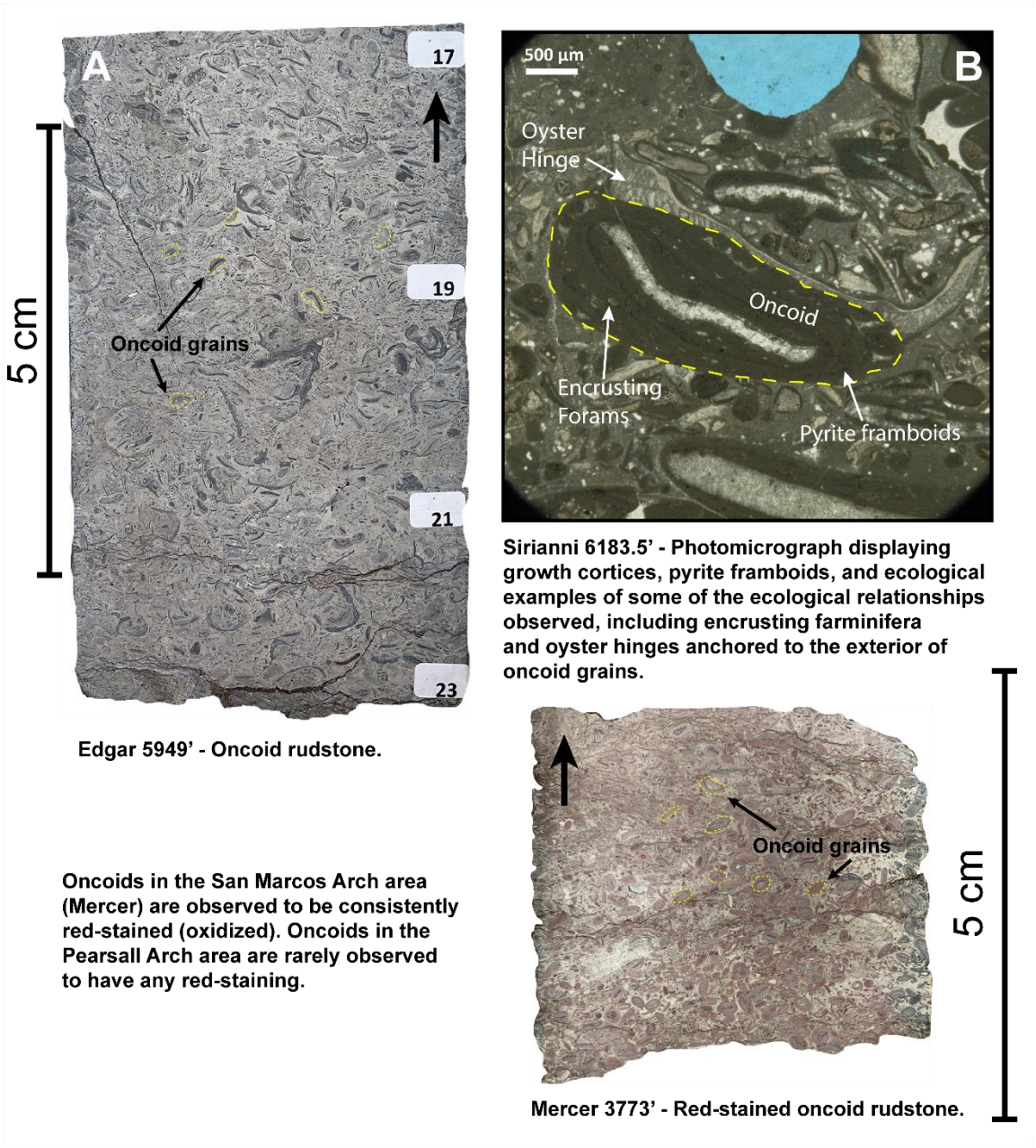

Figure 3.2: Oncoid rudstone (packstone) facies plate.

ECHINOID-MOLLUSK GRAINSTONE

Grain size ranges from fine to coarse, with skeletal fragments comprised predominantly of oyster and echinoid debris, as well of gastropods and bivalves (Figure 3.3). Grain sorting ranges from very poorly sorted to well sorted, and grains are moderately well-rounded to well-rounded. Echinoid-mollusk grainstones are found in beach, spit, and shallow subtidal sand flat environments as part of a land-attached, high-energy, overall progradational shoreface system (Lozo et al., 1958; Inden and Moore, 1983; Kerans and Loucks, 2002; Owens, 2009). Commonly seen with a component of quartz (Silt to pebble in size), especially in cores and outcrops proximal to the Llano uplift (Inden and Moore, 1983). The echinoid-mollusk dominated faunal assemblage is characteristic of the Cow Creek Member of the Pearsall Formation, but persists through the Bexar and into the Lower Glen Rose Member, with increased biodiversity and common serpulid worm-tubes in the Lower Glen Rose.

Loucks (1976) identified intervals of superficially coated, to coated skeletal grainstones within beds in the Upper Cow Creek and Lower Bexar Members of the Pearsall Formation in shoaling assemblages in the Pearsall Arch area, assumed to reflect high-energy wave-agitated settings. Overall, these superficial ooids are rare across the three composite sequences described here.

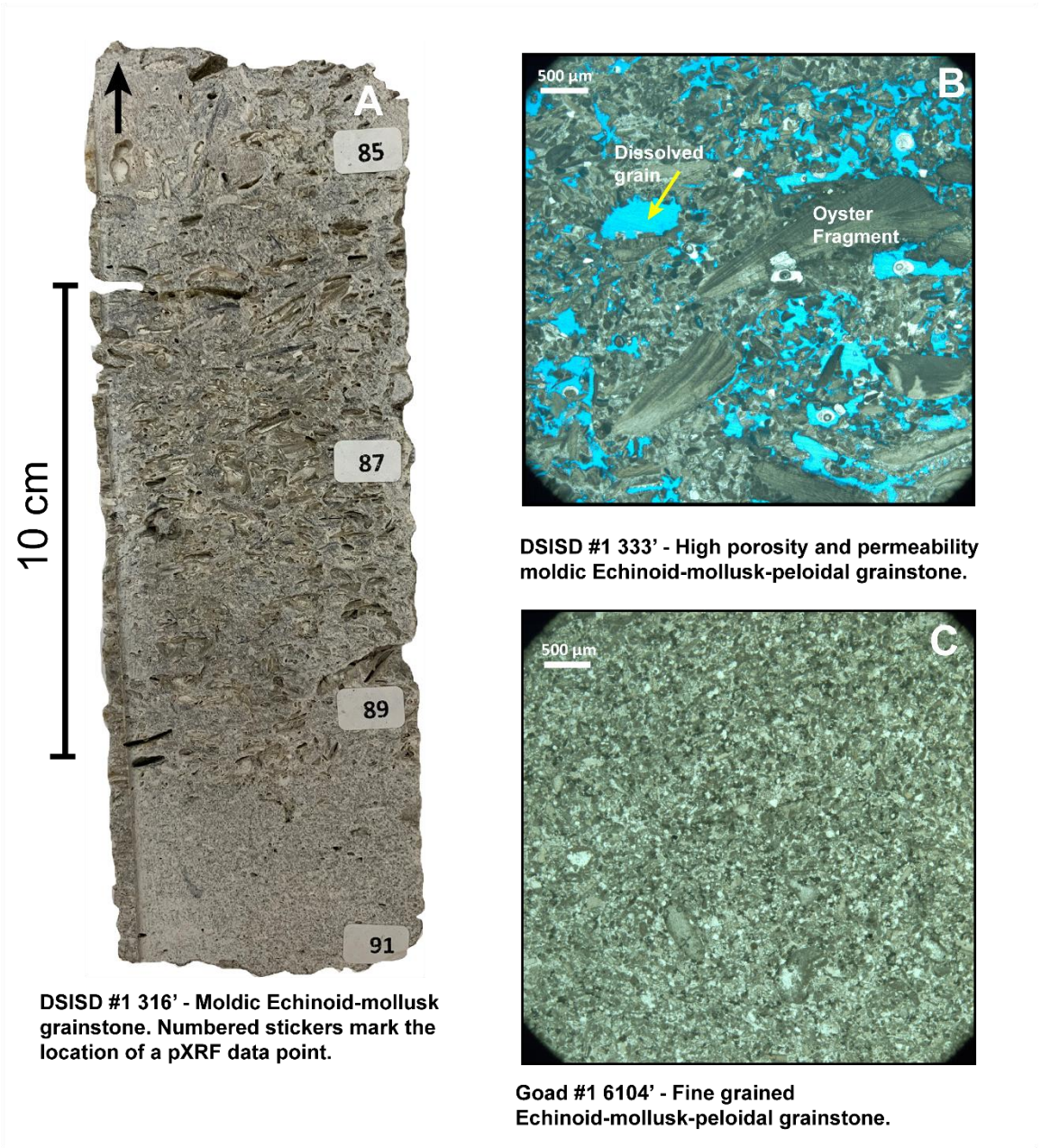

Figure 3.3: Echinoid-mollusk grainstone facies plate.

ECHINOID-MOLLUSK WACKESTONE-PACKSTONE

The Echinoid-mollusk wackestone-packstone facies is found within the Lower Cow Creek, Upper Cow Creek, and Bexar Members of the Pearsall Formation as well as the Lower Glen Rose Formation (Figure 3.4). A high degree of bioturbation is common. Echinoid-mollusk wackestones and packstones are associated as transitional facies between clean carbonate facies and more argillaceous facies, deposited in deeper water than the high-energy grainstones, but generally above storm weather wave base, likely at water depths ranging from 5 to 20 meters.

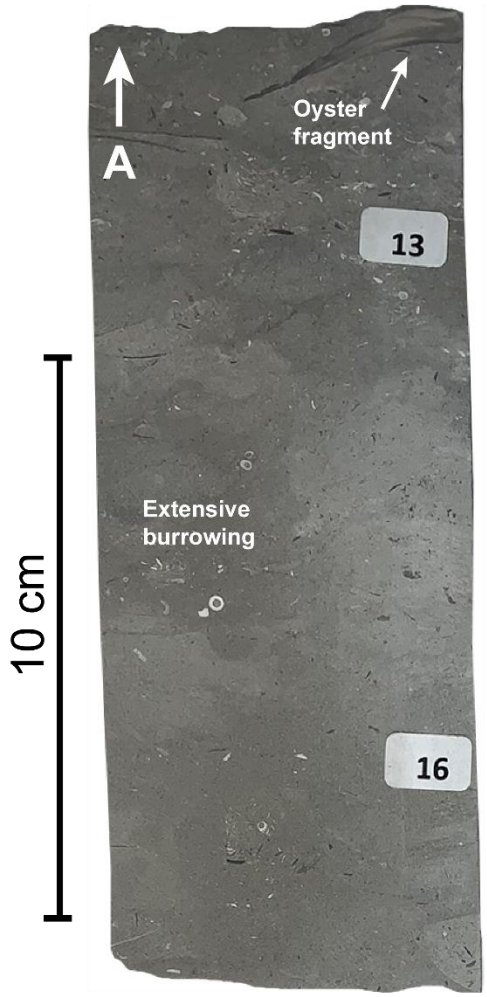

Guadalupe River Damsite 7-1 4123' - Echinoid-mollusk wackestone. Common serpulid worm tubes and mottled burrowing

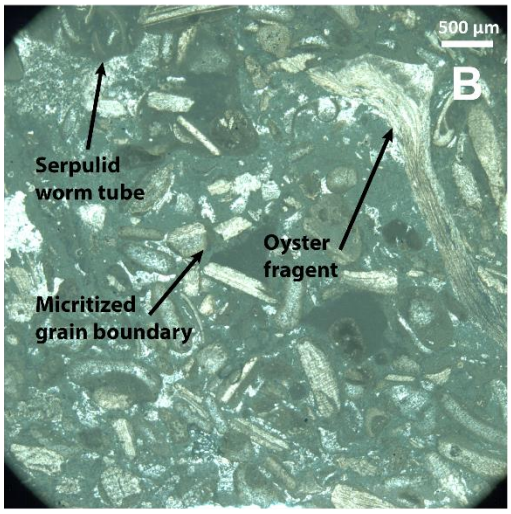

Dix 4123' - Echinoid-mollusk-peloid packstone. Micritic mud matrix, and common micritized skeletal fragments. Serpulid worm tubes common.

Figure 3.4: Echinoid-mollusk wackestone-packstone facies plate.

STROMATOPOROID-CORALGAL BOUNDSTONE-GRAINSTONE

The Stromatoporoid-coralgal boundstone-grainstone facies is found within the Upper Cow Creek Member of the Pearsall Formation in the Pearsall Arch, penetrated by the Tenneco Sirianni well in Frio County. The binding organisms are comprised of stromatoporoids, coral, and spongiopora (Loucks, 1976). The matrix is comprised of wackestone to packstone carbonate with mollusk, echinoid, boring clam allochem associations and serpulid worm tubes (Figure 3.5). The boundstone intervals are interpreted to have formed as a series of discontinuous patch reefs in oxygenated and oligotrophic waters ranging from 1 to 15 meters of water depth. Thickness of these buildups is observed to be up to 30 meters in the Tenneco #1 Sirianni well.

Stromatoporoid-coralgal grainstone and packstone facies are interpreted to have been deposited as flank beds of patch reefs. There is likely some degree of partitioning of grainstones to the higher-energy or windward side of the patch reefs, with packstones deposited preferentially on the lower energy, protected lee side (Loucks, 1976).

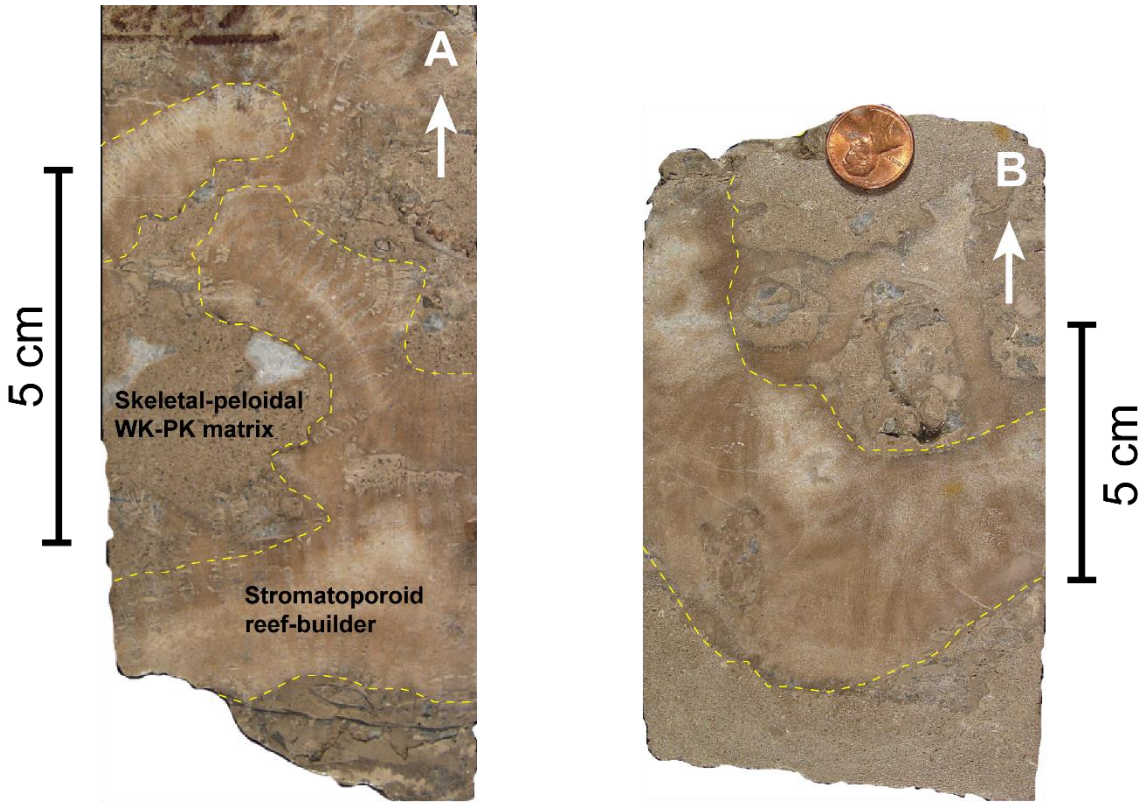

Sirianni 6186' - Stromotoporoid-coralgal Boundstone. Wackestone-Packstone skeletal matrix.

Sirianni 6183.5' - Stromotoporoid-coralgal Boundstone.

Figure 3.5: Stromatoporoid-coralgal boundstone-grainstone facies plate.

TERRIGENOUS MUDSTONE

The terrigenous mudstone facies is observed in the Bexar and Pine Island Members of the Pearsall Formation (Figure 3.6). Comprised of terrigenous muds and clays, this assemblage is generally associated with low bioturbation indices. The terrigenous mudstones are associated with rare oyster fragments, plant fragments, serpulid worm tubes, and pyrite (Phelps, 2011). Ammonite zonation was conducted by Young (1986), and Loucks (1976) observed an increase in (rare) ammonite occurrence and decrease in burrowing stepping downdip from the Pearsall Arch area. This facies has been observed by Loucks (1976) and Amsbury (1996) to contain globigerinid foraminifera in the lowermost potion of the Bexar Member.

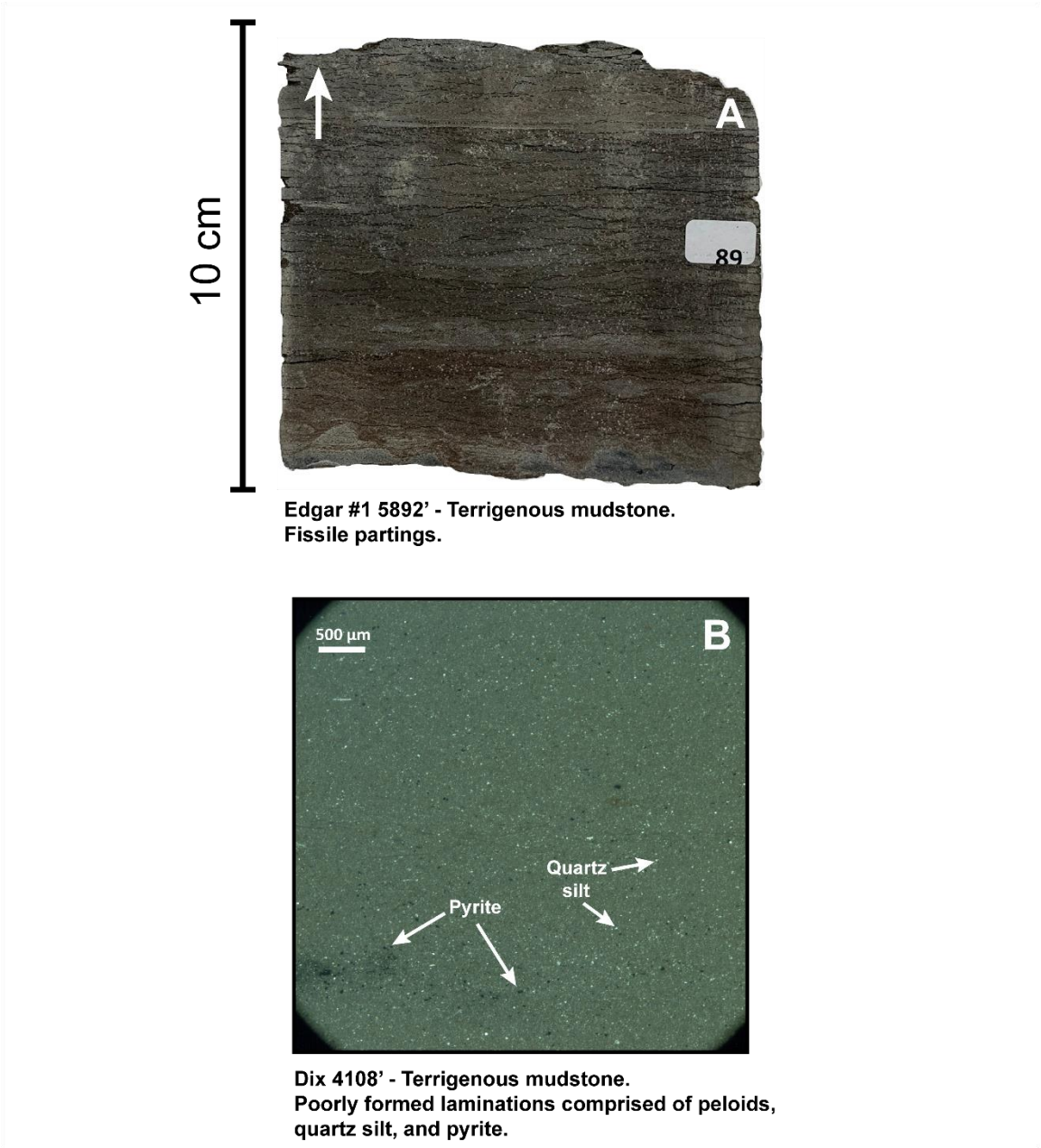

Figure 3.6: Terrigenous mudstone facies plate.

MIXED CALCAREOUS TERRIGENOUS MUDSTONE-WACKESTONE

These facies of mixed calcareous terrigenous mudstones and wackestones are observed to be present in the Lower Cow Creek, Upper Cow Creek, and Bexar members of the Pearsall Formation as well as the Lower Glen Rose Member. This facies assemblage is comprised of interbedded terrigenous mudstones and lime mudstones and wackestones as a transitional facies between the echinoid-mollusk wackestone facies and terrigenous mudstone facies. Carbonate allochems include oysters, mollusks, echinoids, and serpulid worm tubes. Calcareous nodules are common, as well as bioturbation and scour surfaces and hummocky stratification associated with event beds and storm reworking. The MCTM facies was deposited on the open shallow-water shelf within water depth ranges of 5 to 20 meters on the basis of storm event stratification suggesting a position above wave base.

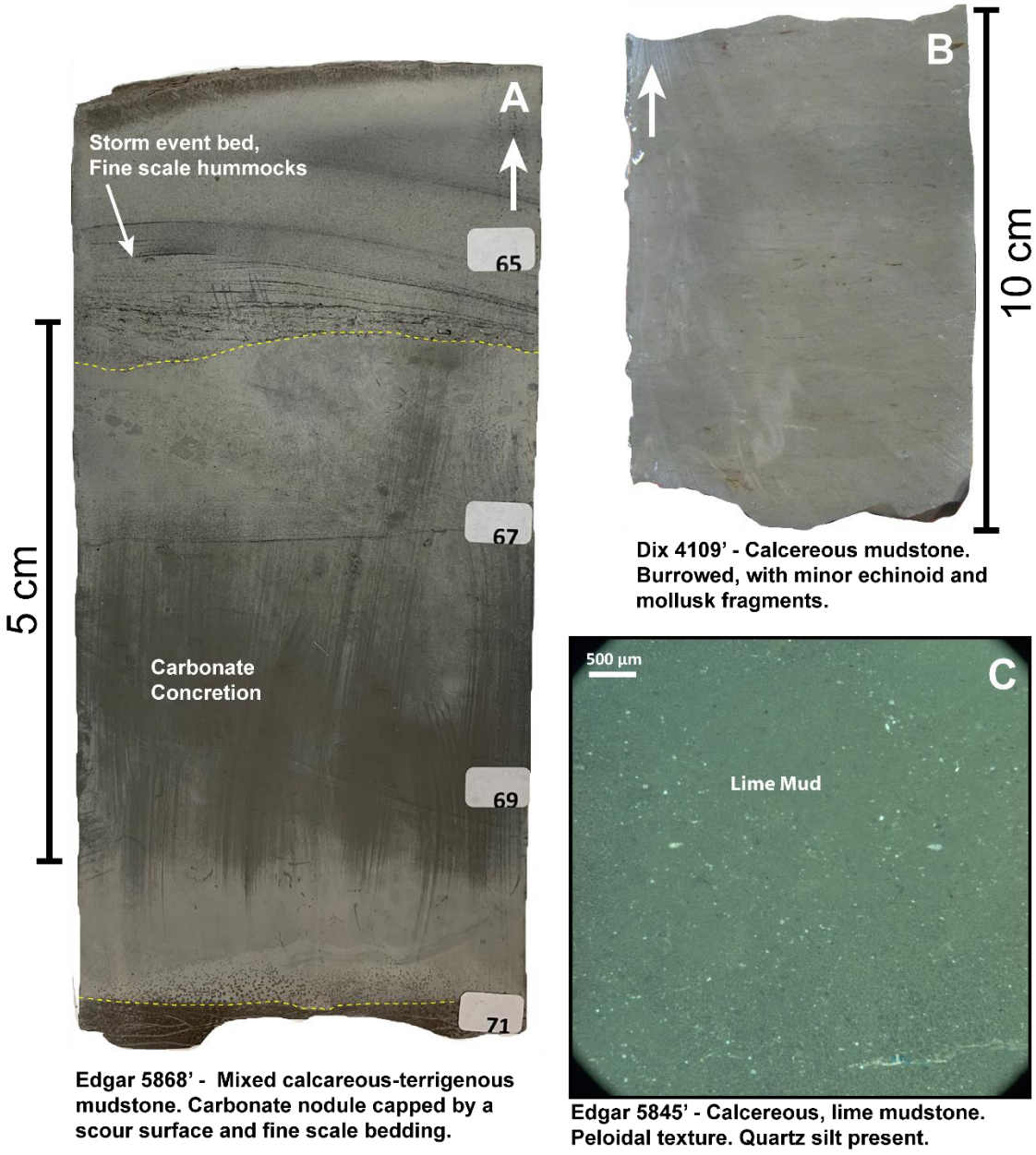

Figure 3.7: Mixed calcareous terrigenous mudstone-wackestone facies plate.

SKELETAL QUARTZ ARENITE

Skeletal quartz arenite is observed within the Lower Glen Rose Member as a laterally continuous unit in the Pearsall Arch area (Bay, 1980). Skeletal fragments included in the arenite are dominantly echinoids and mollusks. Small-scale cross beds and parallel laminae are observed in areas where sedimentary structures were not obfuscated by burrowing. Grains are subrounded to subangular and moderately well sorted. Consistently low mud content indicates wave and current energy was significant to winnow muds from the sediment and distribute the quartz sand across the shelf. Additional detail for the skeletal quartz arenite facies can be found in Bay (1980).

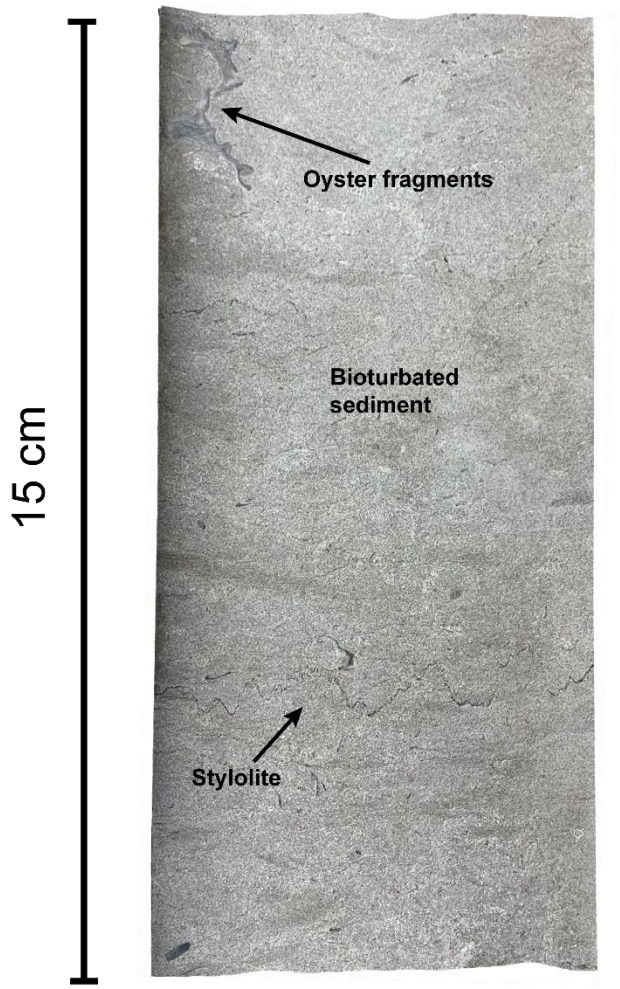

Edgar #1 5642' - Skeletal Quartz Arenite. Rare large disarticulated oyster fragments. Subrounded mollusc and echinoid fragments. Common burrows.

Figure 3.8: Skeletal quartz arenite facies plate.

ORBITOLINA-PELOID WACKESTONE-PACKSTONE

Orbitolina-peloidal wackestones and packstones are found within the Lower and Upper Glen Rose Members, deposited cyclically on the shallow subtidal shelf. Burrowing and bioturbation is common and were likely deposited in open-marine conditions in association with echinoderms and rudists and the growth of coral-rudist bioherms. This facies is observed to be common in pulses during transgressive sequences where the shelf was flooded during base level rise, and Orbitolina-peloid wackestones are chosen as maximum flooding surfaces for third order sequences in the Glen Rose composite sequence (Phelps et al., 2014).

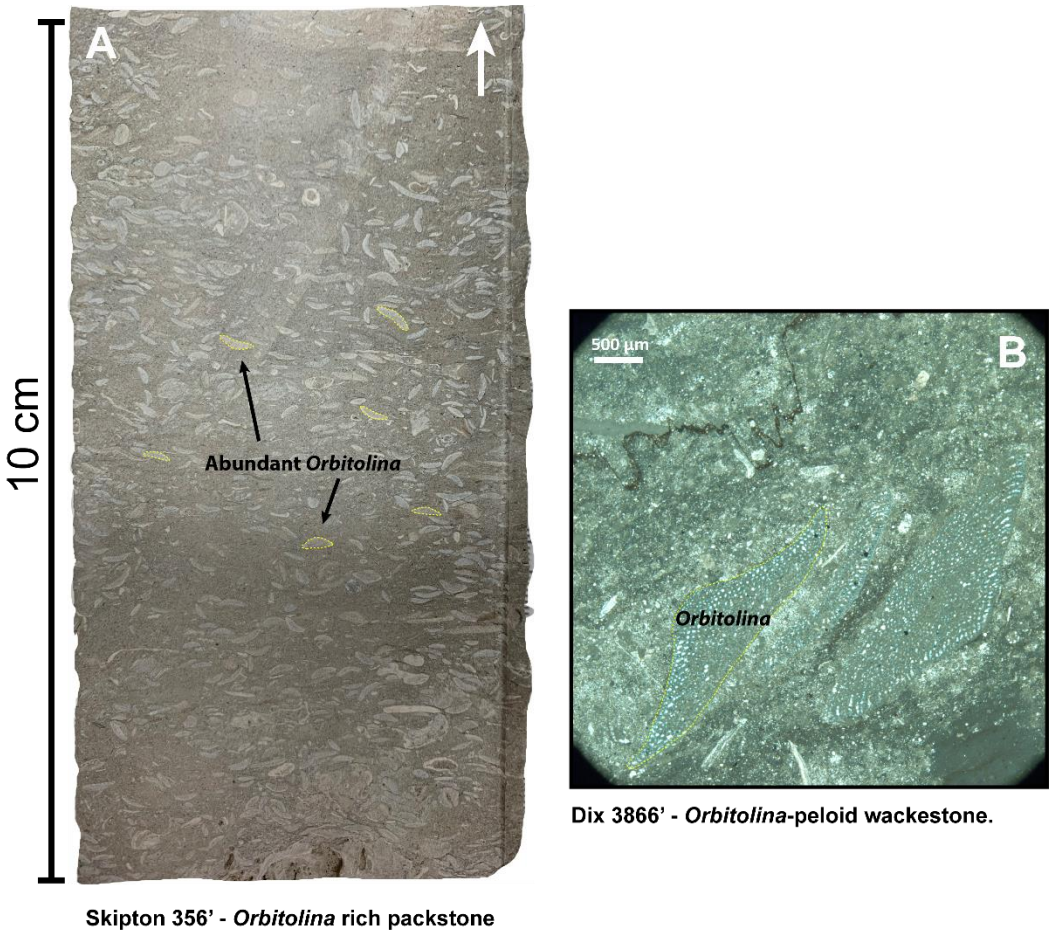

Figure 3.9: Orbitolina-peloid wackestone-packstone facies plate.

MILIOLID-PELOID WACKESTONE-PACKSTONE

Miliolid wackestones and packstones are observed in Lower and Upper Glen Rose Members. Burrows and bioturbation are common and are in association with serpulid worm tubes. Miliolid wackestones and packstones were deposited in shallow, low energy to restricted environments in the shelf interior due to the lack of an abundant and diverse open marine faunal assemblage, and in association with inner ramp peritidal complexes (Bay, 1980; Phelps, 2011). Thin solution-collapse breccias also occur in this interval with the miliolid-rich facies, providing additional support for interpretation of a restricted, elevated salinity setting (Phelps, 2011).

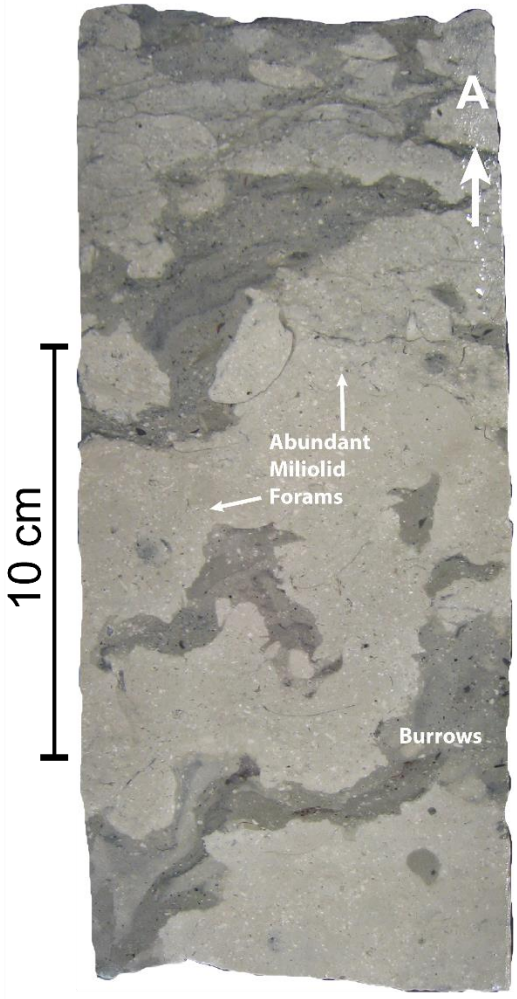

Mercer 3255' - Miliolid mud-dominated packstone. Common gastropods and burrows.

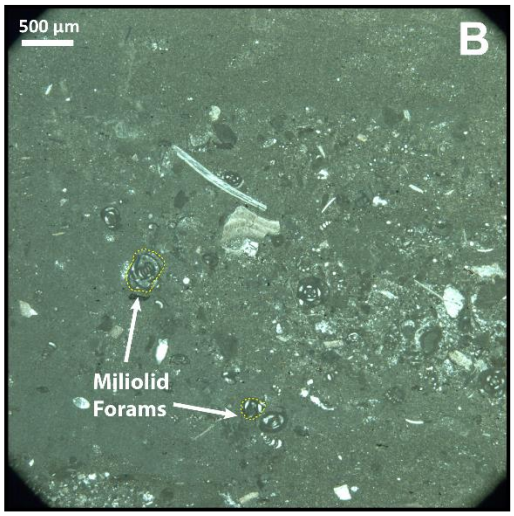

Goad #1 5280' - Miliolid-peloid wackestone.

Figure 3.10: Miliolid-peloid wackestone-packstone facies plate.

MICROBIAL-CORAL-RUDIST BIOHERM ASSEMBLAGES

The microbial-core-rudist bioherm facies encapsulates varied examples of macrofauna that exhibit binding characteristics that are interpreted to have formed a bioherms on the shelf, generating minor positive relief above adjacent lithofacies. The Glen Rose Formation contains coral-stromatoporoid-toucasid-caprinid-monopleurid bafflestones, bindstones, and floatstones (Figure 3.11) (Phelps et al, 2014). The synoptic relief and lateral continuity of these assemblages varies according to the component macrofauna, but likely displayed less than 5 meters of synoptic relief, with less than one kilometer to as much as 10's of kilometers of continuity for monopleurid bafflestones (Phelps et al, 2014). The interpreted water depth for these facies assemblages ranges from 1 to 20 meters, following Perkins (1974). The generally mud-rich matrix and interior setting suggests a moderate to low energy setting.

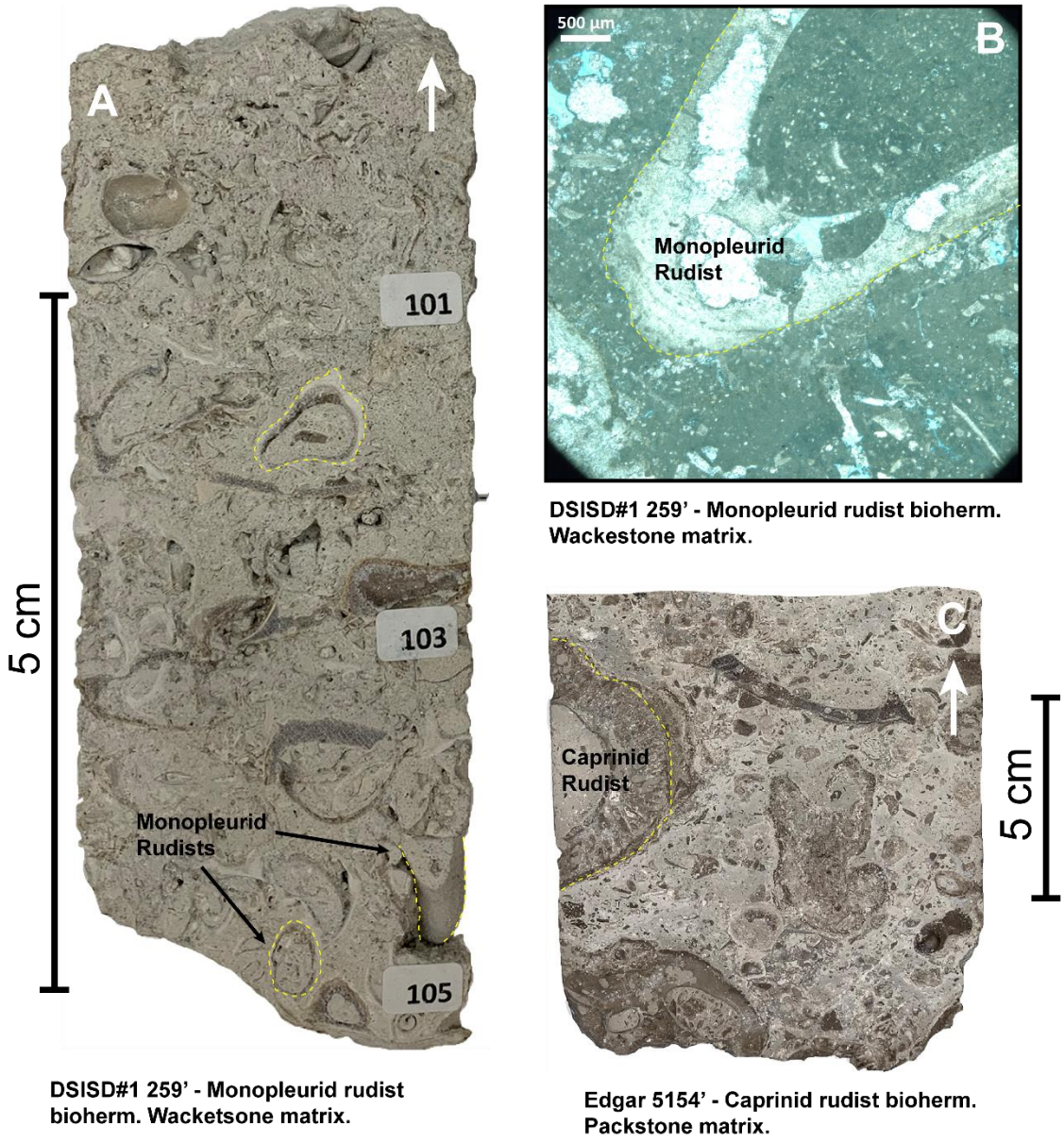

Figure 3.11: Microbial-coral-rudist bioherm assemblages - facies plate.

Chapter 4: Chemofacies Analysis

INTRODUCTION TO CHEMOFACIES

As a result of short scanning times and low operating cost, portable X-ray Fluorescence (pXRF) scanning of geologic core samples has become a burgeoning industry, with the technique capable of generating high resolution datasets containing comprehensive major and trace element abundances present in the rock (Rowe et al., 2012; Larson et al., submitted). Applied to continuous slabbed core and evaluated through statistical segmentation methods, this translates to labeled, depth registered chemomineral data that can be used in conjunction with sedimentological observations and lithological core descriptions to provide additional depth to subsurface interpretations and adds an additional correlation toolkit for use in stratigraphic comparison between core control. This is particularly relevant in mudrock systems, where geochemical processes such as surface water biologic productivity, bottom-water redox conditions, and diagenesis are paramount for two of the things that matters the most to define a good shale reservoir: total organic content and permeability.

In the following subsections, the geochemical and statistical analysis methodology used in this study is outlined through the data processing, multivariate statistics, and interpretation of the Gulf Dix core in Guadalupe county (Figure 1.5, Table 1.2). The Gulf Dix core was chosen as the type-pXRF dataset due to the continuous nature of the core and presence of all lithostratigraphic units. Subsequently, the chemofacies scheme established by Principal Component Analysis (PCA) and k-means cluster analysis is interpreted to be a representative sampling of the Pearsall geologic system in South Texas. Using the Dix pXRF data as a training dataset, this chemofacies scheme is then applied to all pXRF data across the study area by the implementation of a Deep Neural Network (DNN).

Data Processing

Data processing includes organizing and filtering the geochemical dataset before any statistical analysis is applied. Any sample points with missing or incomplete elemental data are discarded, and elemental data below the method detection limit (MDL) is adjusted to respective MDL values per element following detection limits of the Bruker pXRF instruments used. Next, it is important to detect and remove statistical outliers from the dataset. This example uses a simple approach: any measured value that is greater than the mean plus four times the standard deviation is considered an analytical outlier. This approach is then applied to each of the 30 elements accounted for in each data point. Flagged data points are then excluded from subsequent analysis and segmentation processes (Figure 4.1). Next, the data go through a process of standardization, which transforms the values of the element variables to all fall within the same numerical range, having a mean value of zero and a standard deviation of one. This helps account for any errors in the segmentation process that may otherwise arise due to the weighting of attributes within the model. As an example, if a dataset contained Sr values ranging within 20 to 5,000 ppm and Cu values ranging from 5 to 25 ppm, a non-standardized model would determine Cu to be insignificant to Sr.

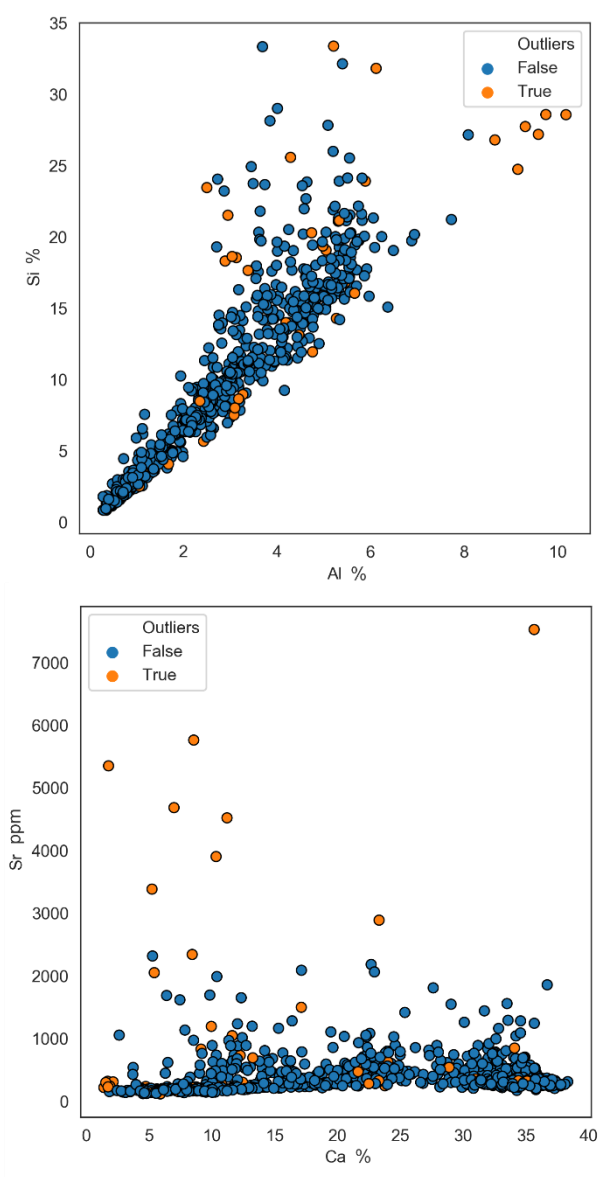

Figure 4.1: Example elemental biplots (Al vs Si, and Ca vs Sr) with outlier datapoints flagged (orange). These outliers will not be considered for PCA segmentation.

Dimensionality Reduction with Principal Component Analysis

Principal Component Analysis (PCA) is a method used to take datasets with a large number of variables, and transform these original variables into “principal components”. PCA generates as many principal components as there are variables in the dataset that describe the total variance present in the data. Ranked with respect to variance captured, principal component one captures the largest amount of variance, principal component two will account for the second largest amount of variance, and so on. The utility of PCA comes from the ability to directly choose the principal components to carry forward into further analysis and interpretation, thereby enabling the ability to simplify the system and remove background noise while maintaining the proponents of the greatest amount of variance unchanged.

Figure 4.2 shows that in the Gulf Dix dataset, 75% of the total variability of the system is contained within the first three principal components (PC). This concept of cumulative explained variance refers to the ratio between the variance explained by individual principal components and the total variance of the system (sum of variances of all principal components). Here, PC-1 alone accounts for nearly 60%, and PC-2 accounts for roughly 11%. Following the premise that minerals are the fundamental control of major elements in sedimentary systems, PC-1 should be expected to be associated with rock sample bulk mineralogy. PC-2 will then involve trace element variability associated with depositional fluid chemistry and later diagenetic overprinting (Larson et al., submitted)

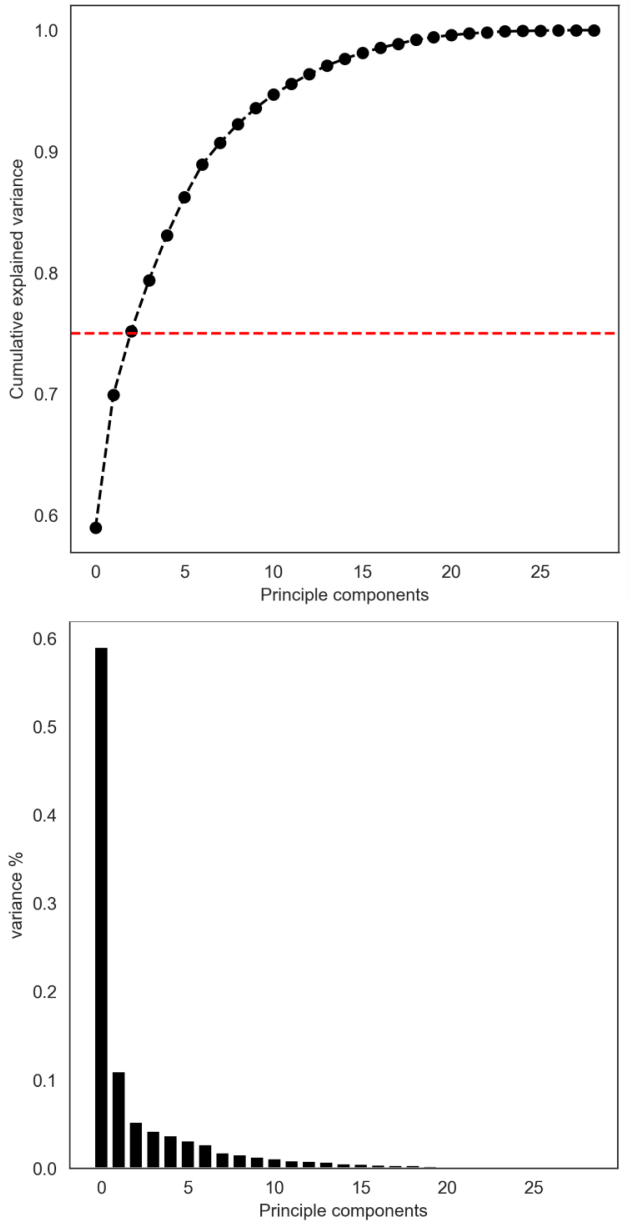

Figure 4.2: Cumulative explained variance of PCA conducted on the Gulf Dix dataset based on the number of principal components included, and the contribution of each individual principal component. An Arbitrary cutoff of 75% cumulative explained variance is marked by a red dashed line.

Segmentation by K-means Clustering

This workflow uses k-means clustering, which is an unsupervised segmentation method utilizing machine learning libraries that iteratively divides the dataset into the prescribed number of clusters. After choosing the number of clusters, those clusters are then given a seed value, or set of starting points. Once the initial seeds are plotted, each data point becomes assigned to the nearest seed based on proximity. The next step is to calculate the centroid for each seed, which is defined as the geometrical center of the data points assigned to each respective seed. The previous steps are then repeated until the system converges and a clustering solution is reached where the distance between the cluster centroids are maximized and distance between points within a cluster are minimized. These final groupings are then defined as representative chemofacies, which are effectively chemofacies end members based on genetically similar bulk and trace element distributions.

Visualization of PCA Data

Figure 4.2, below, is the PCA biplot achieved by the previous data processing and segmentation steps. Individual pXRF data points here are plotted in association of the color of the chemofacies grouping (k-means) they are contained within. The labeled arrows are the weights, or loadings that each element has on principal components one (PC-1) and two (PC-2).

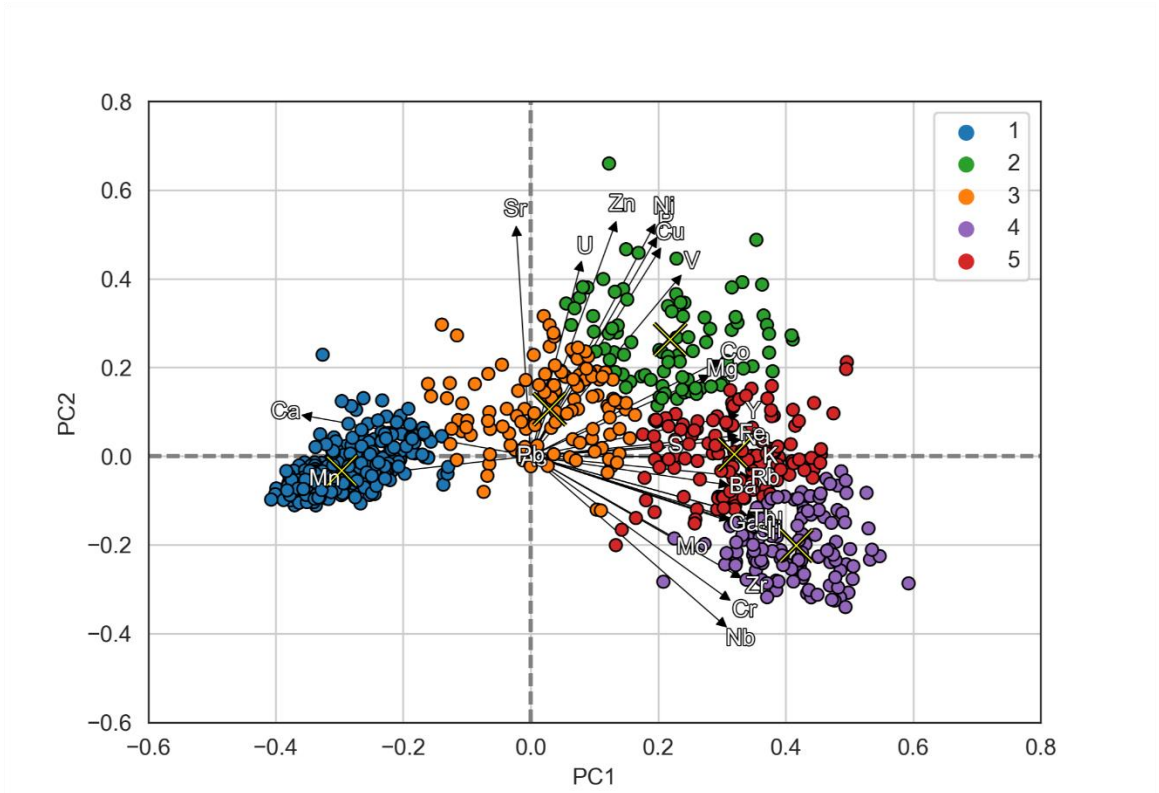

Figure 4.3: PCA Biplot of the Gulf Dix pXRF dataset. Chemofacies are labeled and colored, and k-means centers for each grouping is denoted by the black and yellow ‘X’ symbols. Arrows indicate the loading of the labeled element on the principal component axes.

The extent of the loading that a given element has on the principal components is visualized by the relative angle and length of that element's respective arrow. For example, the blue cluster (Chemofacies 1) is strongly loaded by calcium and manganese. Roughly opposite calcium are the arrows for silicon and aluminum. All other groups experience some degree of loading by silicon, with chemofacies 2, 4, and 5 all residing within positive PC-1 values, and are therefore the most strongly correlated with Si and Al, and the least strongly correlated with Ca. Chemofacies 3, in orange, covers a spread of both negative and positive PC-1 values, indicating that this is a transitionary chemofacies with loading from both calcium and silicon.

From a first order mineralogic context, blue chemofacies are likely to be associated with the calcite-dominated carbonate buildups (Ca-enriched), and the orange chemofacies associated with more mixed argillaceous-carbonate facies. In the following section this observation is compared to a lithological core description over the same interval (Figure 4.4). The box plot distributions of Si, Al, and Ca within the Gulf Dix dataset combined with comparisons to the lithologic core description support the premise that minerals control the concentrations of major elements in sedimentary systems (Figure 4.5).

Principal component two is more heavily loaded by trace elements. Co, V, and U are commonly used as indicators of bottom-water redox conditions, while Ni, Cu, and Zn are associated with surface water productivity (Breit and Wanty, 1991; Hastings et al., 1996; Holland, 1984; Saito and Moffett, 2002; Saito et al., 2002; Tribovillard et al., 2006). Production of organic matter and its subsequent preservation or oxidization is critical in understanding mudrock depositional systems. Additionally, trace elements Th, Ti, Zr, and Rb are proxies of detrital influence (Calvert and Pedersen, 2006). Following these proxies, the purple cluster (Chemofacies 4) is strongly loaded by Rb, Zr, Th, and Ti indicating

detrital flux and the most terrigenous and shale rich, detrital-enriched, intervals of the core (Figure 4.4).

Following the chemical loadings within each chemofacies grouping, these observations can be used to interpret 1-D depth series along the core (Figure 4.4). This effort of establishing a workflow to combine evaluation of both bulk mineralogic trends (PCA-1) and trace element oceanographic trends (PCA-2) for visualization on the same plot enables a path for the integrated interpretation of a number of key depositional system drivers, including sediment sourcing and evolving ocean water chemistry.

From Figure 4.4, the blue chemofacies (Chemofacies 1) correlates with clean carbonate intervals as interpreted in the lithologic core description, ranging from oncolite rudstones in the Upper Cow Creek Member and echinoid packstones in the Lower Glen Rose. In comparison, Chemofacies 4 is associated with the most detrital-enriched terrigenous mudstone intervals, such as the Pine Island Shale Member. The raw Ca and Al curves, as well as a computed gamma ray log, are also plotted in order to offer trendline comparisons to the chemofacies classifications.

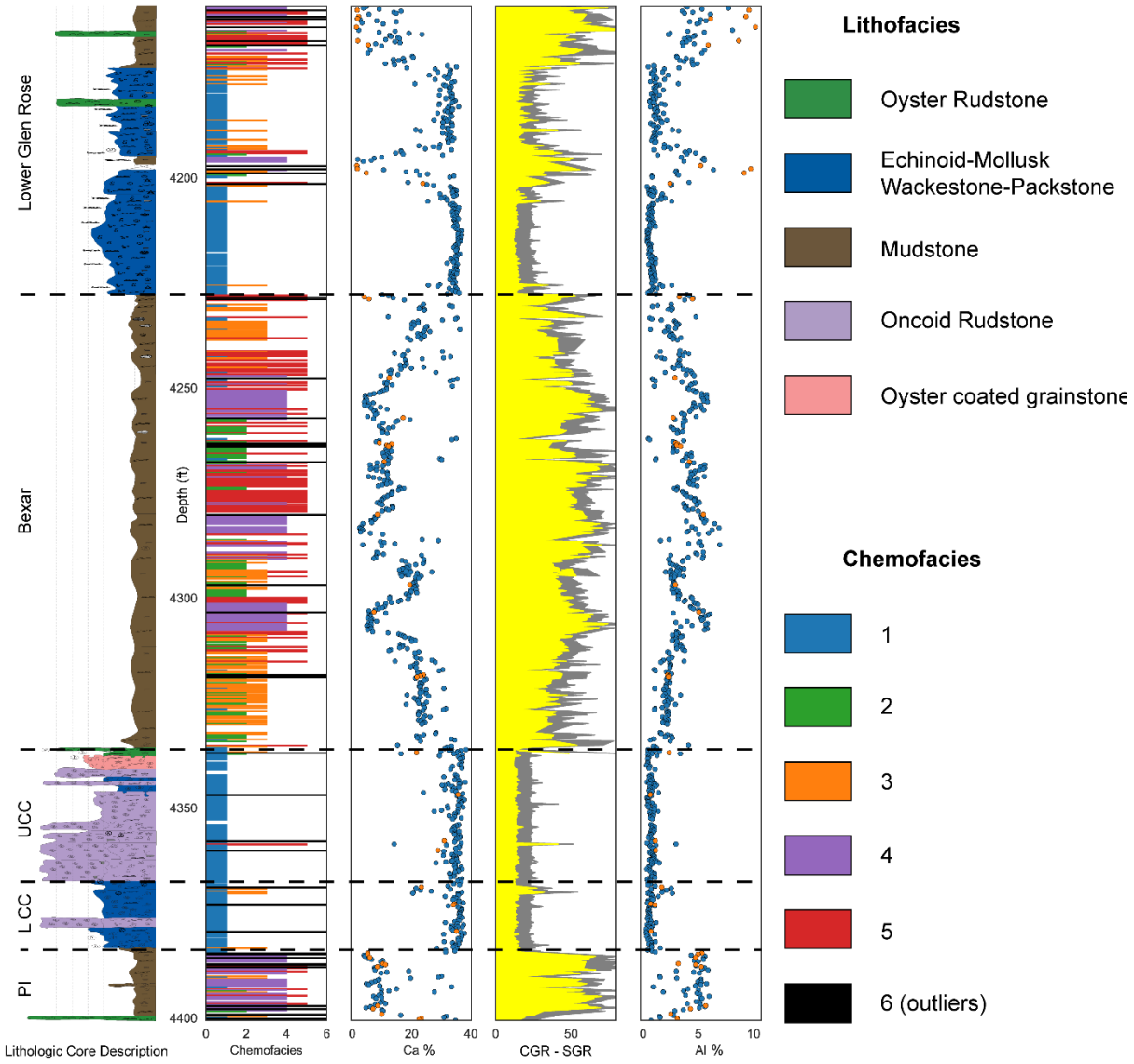

Figure 4.4: Series of 1D plots for the Gulf Dix core, including lithological core description, chemofacies, Ca, CGR-SGR, and Al plots. Analytical outlier data points are orange. (Core description after Phelps, 2011)

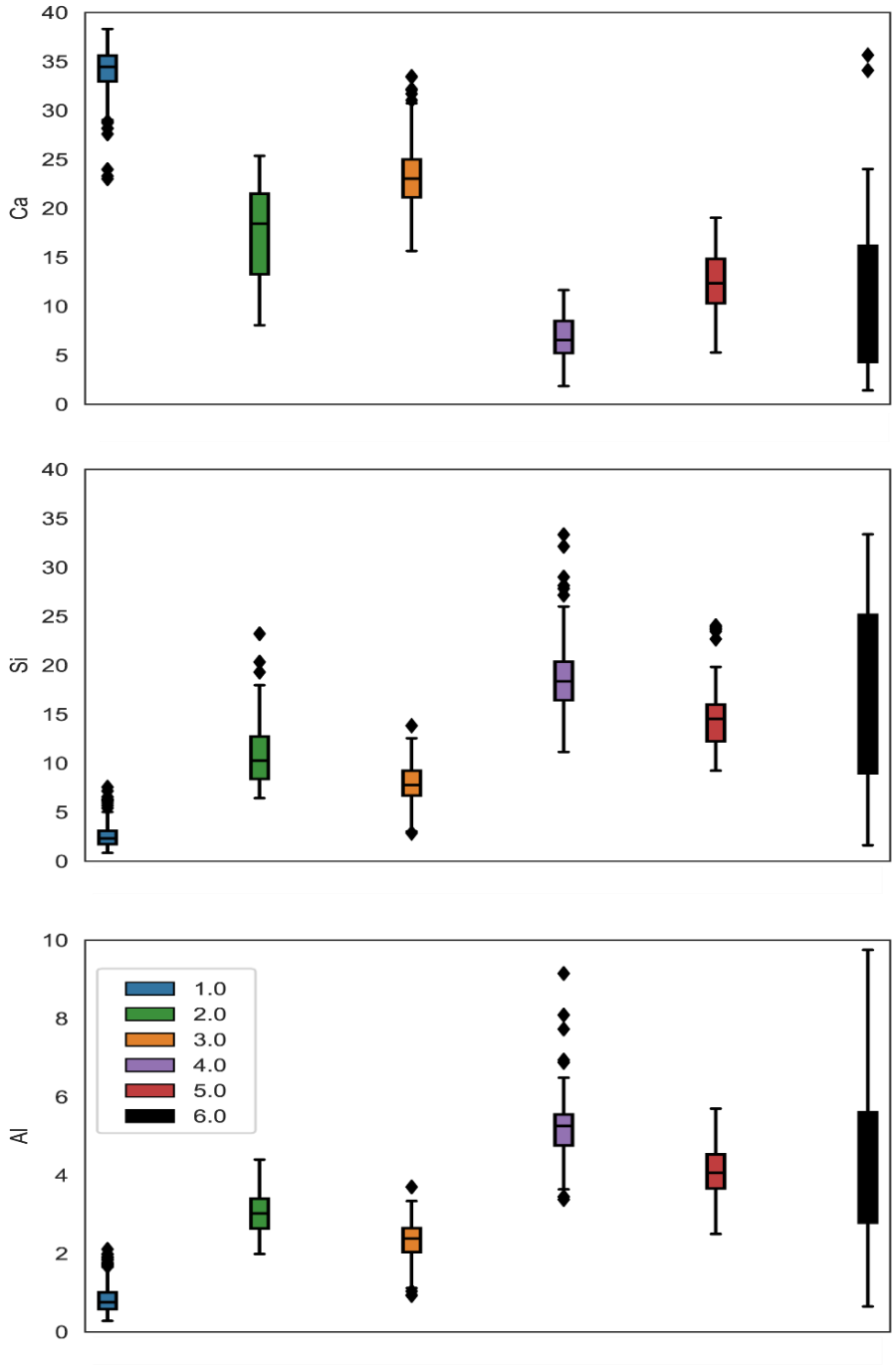

Figure 4.5: Box plots of elemental distributions within the Gulf Dix dataset by chemofacies groupings, including Ca, Si, and Al.

Elemental box plots of the Gulf Dix dataset organized by chemofacies illustrate the mean values and distributions of the mineralogy captured within each chemofacies, and provides an alternative perspective into what is essentially loading of PC-1. Chemofacies 1 and 2 expectedly have the highest Ca concentrations and by inverse association, the lowest Si concentrations. Chemofacies 4 is the most enriched with respect to Al, followed by chemofacies 5 and 2. These plots once again illustrate the separation between chemofacies 1 and the group comprised of chemofacies 2, 4, and 5 in terms of mineralogy, and point to the value in PC-2 to investigate further separation between chemofacies 2, 4, and 5. Chemofacies 6, the outlier group, unsurprisingly has a wide distribution, dissimilar to the other constrained groupings. Datapoints classified in this outlier chemofacies are those that are found dissimilar to any of the other individual five chemofacies classifications.

Deep Learning Neural Network

The application of Artificial Neural Networks (ANN) and the implementation of deep learning algorithms allows for the development of computational models that are characterized by invoking multiple processing layers to interrogate representations of data with multiple levels of abstraction. Neural nets are able to discover nuanced relationships in large datasets by using a series of propagation algorithms to refine internal parameters used to compute data representation in each layer based on the previous layer (McCulloch and Pitts, 1943; Farley and Clark, 1954; LeCun et al., 2015) (Figure 4.6).

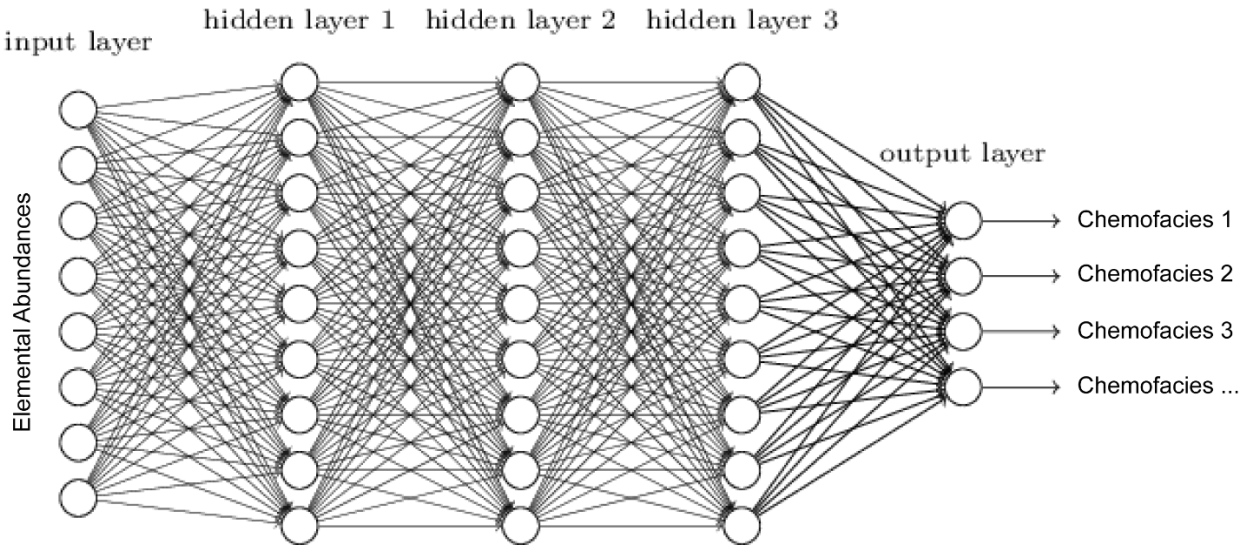

Figure 4.6: Example design of the input, hidden layers, and output layers of a neural network. The input layer in this case is comprised of major and trace elemental abundance data, with the end goal, or output layer, of a resultant chemofacies classification. (Modified after Nielsen, 2015).

The structure of a neural network is loosely modelled after neuron structure in a biological brain. Connection points, called neurons, are connected by a series of weighted inputs and activation functions so that all neurons are connected through a series of layers within the model structure. This structure and algorithmic approach intends to replicate the way that humans learn, particularly within the realm of pattern recognition. Neural networks powered by modern computational resources are able to in many situations outperform human expert capacities for pattern recognition, especially in complex and multidimensional problem sets when paired with a high volume of data (Buetti-Dinh, 2019).

The learning aspect of a deep learning neural network comes from the subjection of the model to input data. These data are called the training dataset. The training dataset for this study consists of the unsupervised clusters developed using principal component analysis of the Gulf Dix pXRF dataset (outlined above). Each labeled (i.e., chemofacies cluster number) can be interrogated across all of its elemental concentrations to develop a new neural model. This neural model is then used to predict chemofacies across all pXRF data. For this study, the DNN was given a shuffled input dataset of pXRF elemental abundance data for the Gulf Dix core. Thirty percent of the dataset is randomly selected for the test dataset, and 70 percent is used in the training dataset. The neural network consists of 30 input layers (pXRF elemental concentrations), 3 hidden layers each composed of ten neurons, and six outputs (chemofacies classifications). A rectified linear unit (ReLU) activation function was applied to the hidden layers, and softmax function was applied to the output layer in order to retrieve the confidence interval with respect to the chemofacies predicted by the neural model. A maximum of 2000 forward and backward propagations were applied and the resultant output chemofacies predictions are compared to the chemofacies designations provided by the original PCA and k-means segmentation

methodology. A back-propagation algorithm is then applied, which is effectively the essence of deep learning neural networks. Back-propagation is the practice of fine tuning the weights of hidden layers within the neural network iteratively based on the attempt to minimize the error rate between the training dataset and predicted values on the next forward-propagation. Once properly tuned, the system will converge on a global minimized error. A well-designed neural network and training dataset combination can then reliably be applied to new datasets separate from the training dataset, but within the same geological system. Figure 4.7 shows the resultant confusion matrix of the deep learning neural network, after training, being applied to the original dataset. There is a high level of agreement between the target values and the values predicted by the neural network, indicating that the neural network was successful in learning from the training dataset. Figure 4.8 shows a side by side comparison of the original PCA segmentation and the neural network, with the lithological core description for reference. Again, there is good agreement between the training dataset and the neural network, and this gives confidence that the neural network can be applied to other pXRF datasets.

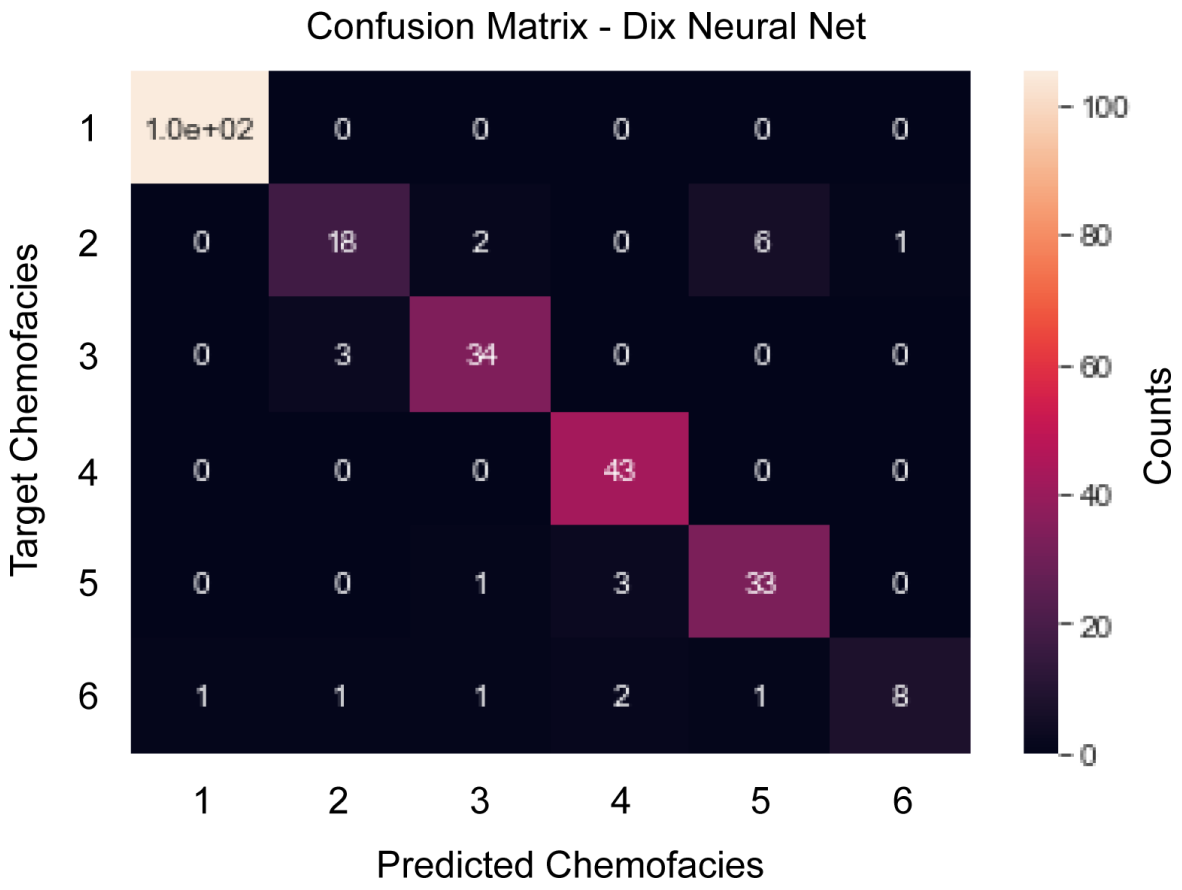

Figure 4.7: Confusion matrix of the artificial neural network trained on the Gulf Dix data. The predicted chemofacies versus target chemofacies from the training dataset are compared.

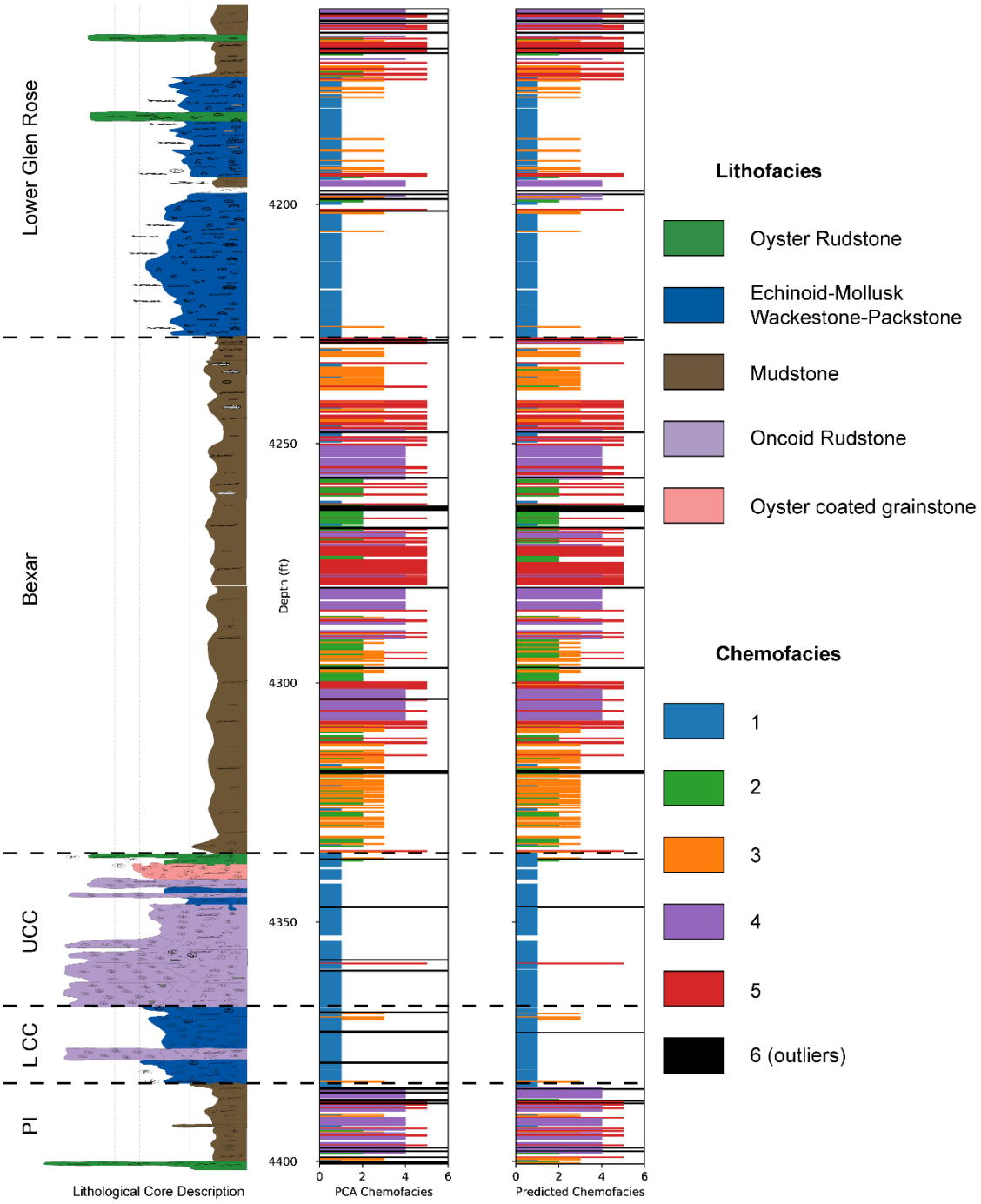

Figure 4.8: Comparison between lithologic core description, PCA chemofacies training dataset, and the resultant predicted chemofacies produced by the trained neural network. (Core description after Phelps, 2011).

Accuracy of the neural model could potentially be improved through several methods. Recent findings in other fields have shown that grouped ensembles of deep learning models outperform any individual neural net when the ensemble is used in unison (Fawaz et al., 2019). Another direction for further improvement of the neural model would be furthered by preparation of the training dataset. One potential confounding principle inherent in the neural net presented in this work is that pXRF data points flagged as outliers were not removed from the training dataset ahead of usage as a training dataset. This may have introduced an error vector that could be minimized by the identification and reclassification of outliers into labeled categories more representative of what they are, which may for example include the identification and reclassification of some outliers as ash layers. In fact, the ideal training dataset may be a compiled and curated series of pXRF points most representative of end member chemofacies from an aggregated set of cores. In this way, the neural model is iteratively improved with the addition of more core control, and the training dataset moves towards a unified model of the target geologic system, from reservoir to field scale applications. The neural model would also benefit from this implicit increase in training dataset size, wherein a greater number of curated data points representative of the end member chemofacies would fortify the multiple linear regressions performed and the weighting assigned within the forwards and backwards propagation algorithms during deep learning.

CHEMOFACIES CLASSIFICATION SCHEME

The chemofacies classification discussed below refers to the k-means segmentation shown on the PCA biplot of the Dix core (Figure 4.3). This chemofacies scheme is consistent across all wells in the pXRF suite due to training and application of the deep neural net to the remaining datasets.

Chemofacies 1 – Carbonate-dominated

The first chemofacies is characterized by a high loading of Ca and Mn. This chemofacies is associated with generally clean carbonate intervals, having low mud content, and lacking argillaceous or detrital enrichment. Oceanographically, this chemofacies is interpreted to have been deposited within a well circulated, oxygenated water column, and is associated with a productive carbonate factory, either in-place or transported.

Chemofacies 2 – Dysoxic calcareous terrigenous mudstone

Chemofacies 2 is characterized by a combined loading of several redox sensitive elemental proxies, including Cu, V, Co, and U, which point to at least dysoxic and up to suboxic bottom-water redox conditions during deposition (Tyson, 1991; Holland, 1984; Breit and Wanty, 1991; Hastings et al., 1996; Saito et al., 2002; Saito and Moffett, 2002). This chemofacies is also depleted of Calcium and enriched in Si-Al, and is therefore more closely associated with a calcareous to terrigenous mudstone lithofacies.

Chemofacies 3 – Oxic mixed argillaceous calcareous mudstone-wackestone

Chemofacies 3 is an intermediary between the Ca and Mn loaded Chemofacies 1 and the Si-Al loaded Chemofacies 2, 4, and 5. This chemofacies is associated with mixed argillaceous and calcareous mudstone and wackestone lithofacies. Oceanographically, this chemofacies is interpreted to have been deposited within a generally well circulated and oxygenated water column.

Chemofacies 4 – Euxinic detrital-enriched mudstone

Chemofacies 4 is characterized by a combined loading of several detrital elemental proxies, including Rb, Zr, Th, and Ti which indicates a heightened detrital flux (Calvert

and Pedersen, 2006). Furthermore, enrichment in Mo could point to intermittent to sustained euxinic bottom-water conditions (Meyers et al., 2005; Tribovillard, 2006). The implication for euxinic bottom-water conditions is the presence of free H_2S in the sediment water interface, often leading to the formation of pyrite framboids within the sediment.

Chemofacies 5 – Suboxic argillaceous mudstone

Chemofacies 5 is an intermediary between the euxinic Chemofacies 4 and the dysoxic to suboxic chemofacies 2. This facies is depleted in Ca and is instead detrital-enriched.

Chemofacies 6 (Outliers)

The final, sixth chemofacies is a bin for analytical outlier datapoints, that at present are not considered during chemofacies analysis. These are datapoints that were considered by the DNN to fall outside of reasonable bounds of similarity with any of the five endmember chemofacies.

CORE ANALYSIS

With the establishment of a unified chemofacies scheme, these groupings can then be used to explore chemofacies stacking patterns, chemofacies partitioning, and enables these observations to be carried forward and directly compared between wells, something that has previously been a severe limitation of pXRF data applications. In the section below, a series of five cores have been selected that span ranges in both strike and dip direction and feature a sampling of both shoreline-distal and shoreline-proximal lithofacies. Aggregated chemofacies partitioning trends across the available pXRF dataset is further discussed in Chapter 5.

Dix Chemofacies

Chemofacies quantification of the Gulf Dix well shown in Figure 4.9 displays a high degree of complexity and nuance, particularly within the Pine Island and Bexar Members. In the Bexar member, there are three distinct pulses of detrital-enriched, euxinic sediment (chemofacies 4) punctuated by intermittent dysoxic-suboxic conditions (chemofacies 2) and suboxic conditions (chemofacies 5) before cleaning upwards at the top of the Bexar Member from argillaceous carbonates (chemofacies 3) to clean carbonates (chemofacies 1) in the overlying Lower Glen Rose Member. This intra-formation mudstone variability of the Bexar Member directly contrasts with the chemofacies expression of the Pine Island Member, which dominantly consists of detrital enriched and euxinic chemofacies 4. The facies stacking pattern exhibited in the Lower and Upper Cow Creek Members is consistently dominated by chemofacies 1, showing carbonate enrichment. However, fine-tuned analysis and interpretation of this Cow Creek chemofacies and how they relate to the lithofacies will be further explored in Chapter 5.

The confidence interval of the neural model is high, averaging 93%, which is to be expected for the Dix, since a portion of this dataset was used to train the neural model. Comparisons to other wells in the data set will maintain this high level of confidence, with the system-wide confidence interval mean at 83%.

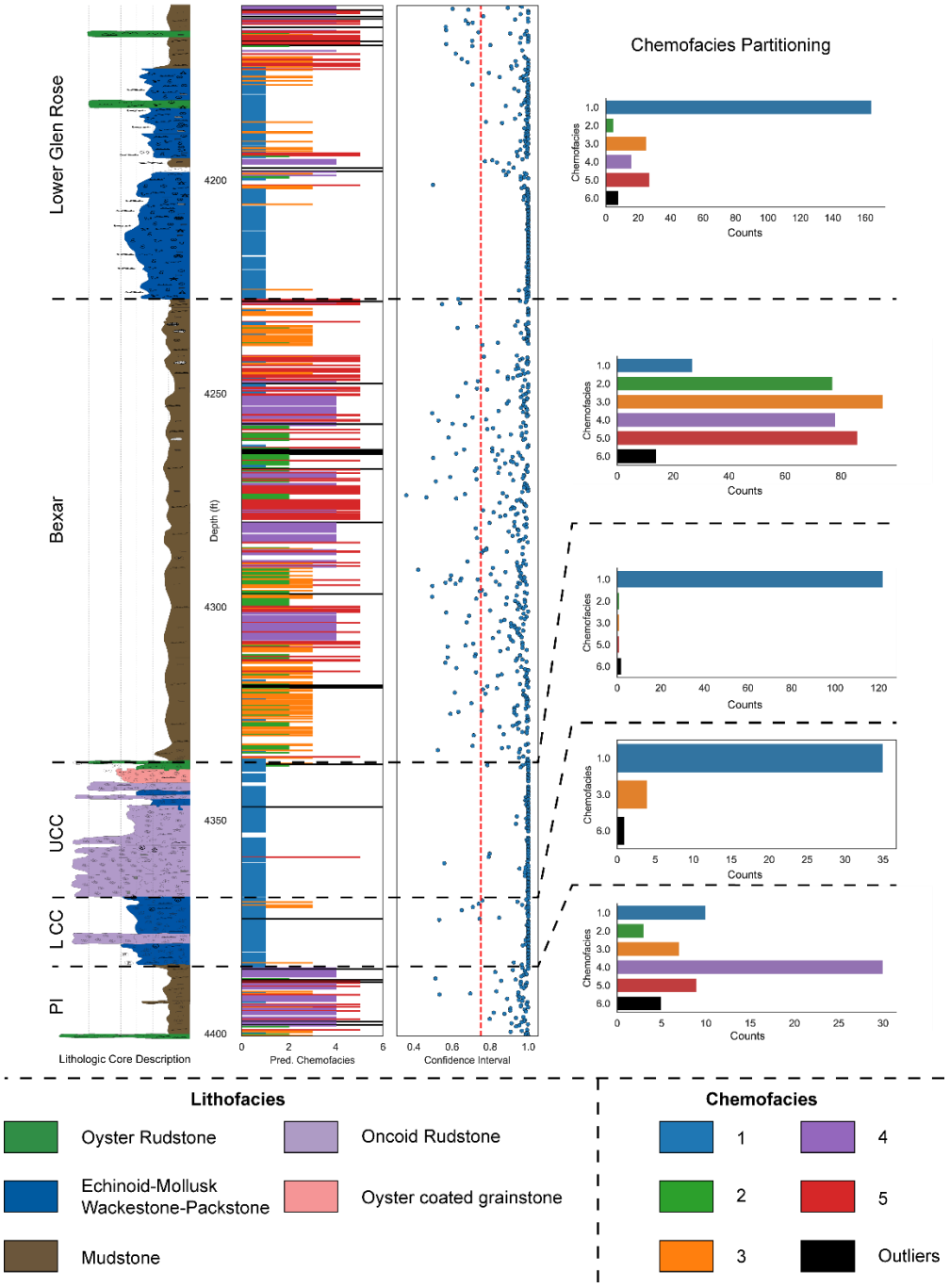

Figure 4.9: Core description, predicted chemofacies, neural network confidence intervals, and chemofacies partitioning within each respectively labeled Member. Gulf Dix. (Core description after Phelps, 2011).

Mercer Chemofacies

The Magnolia Mercer well is similar to the Dix core in terms of chemofacies stacking patterns and partitioning, which is to be expected considering their relative proximity (13 km) and the shared location on the shelf, depositionally. Within the Bexar, largely the same pattern emerges, with a series of suboxic to euxinic detrital pulses followed by a transition into the carbonate dominated Lower Glen Rose above. The Pine Island is again found to be consistently dominated by chemofacies 4 and characterized by sustained euxinic conditions. The mean confidence interval for the Mercer dataset is 87%.

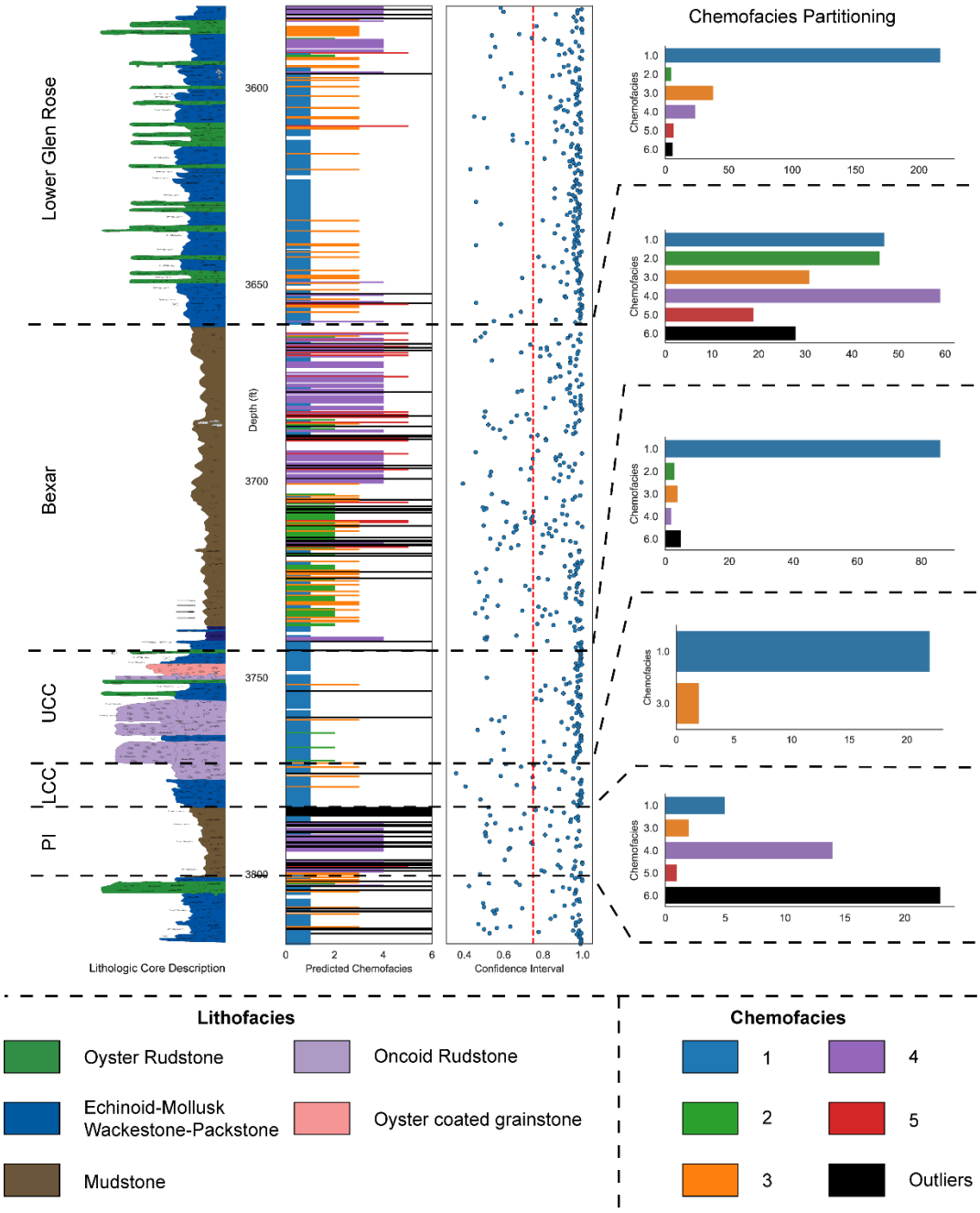

Figure 4.10: Core description, predicted chemofacies, neural network confidence intervals, and chemofacies partitioning within each respectively labeled Member. Magnolia Mercer. (Core description after Phelps, 2011).

Sirianni Chemofacies

The Tenneco #1 Sirianni is located in Frio County, in the Pearsall Arch area. Figure 4.11 shows the application of the neural model to the Sirianni dataset. The Lower Cow Creek Member here is characterized as quite argillaceous, more so than what is typically seen in the San Marcos Arch area, and fluxes between oxic and suboxic conditions, before cleaning up into the highly dominated chemofacies 1 in the Upper Cow Creek stromatoporoids-coralgal reef buildup. The Bexar is characterized by suboxic conditions at the base, followed by a few pulses of euxinia and cyclic suboxia, before cleaning upwards into the oxygenated shoal-water carbonate complexes characteristic of the Bexar composite sequence in the Pearsall Arch area. The mean confidence interval for this well is 90%, which gives confidence for the comparisons drawn between the Pearsall Arch and San Marcos Arch pXRF datasets using this method.

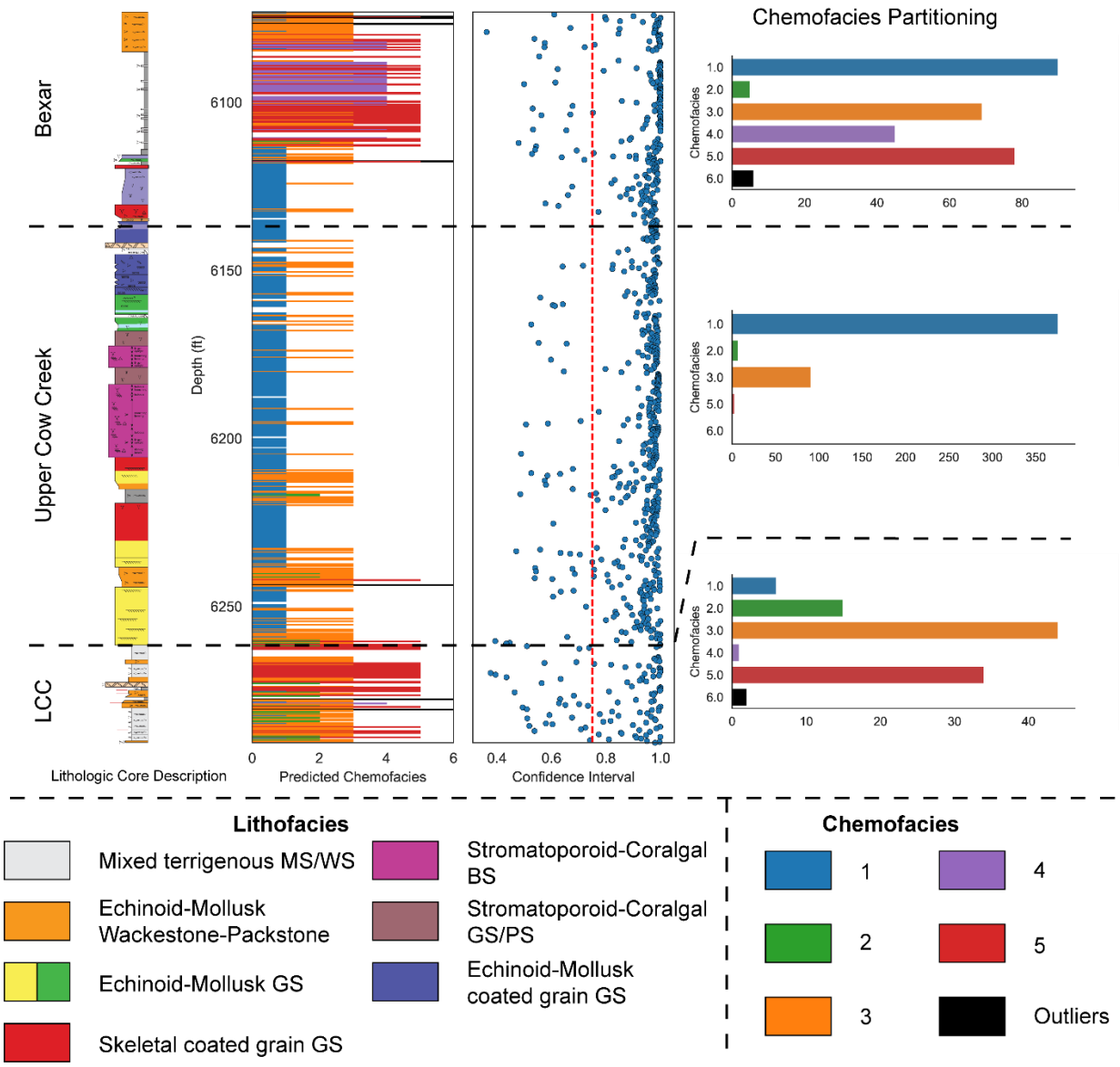

Figure 4.11: Core description, predicted chemofacies, neural network confidence intervals, and chemofacies partitioning within each respectively labeled Member. Tenneco #1 Sirianni. (Core description after Playton).

Guadalupe River Damsite #7-1 Chemofacies

The Guadalupe River Damsite #7-1 well, located in Kendall County, is a shoreline-proximal well. Due to the proximal nature of this well, the deep neural network is encountering lithofacies that are not included in the training dataset (such as shoreface sandstones) since it was trained on the Dix well, located on a more distal position on the shelf. Interestingly, the neural model still performs well regardless, with a mean confidence interval of 92%. Here the Pine Island Shale chemofacies partitioning is very similar to that observed in the Dix and Mercer wells, with a dominance of chemofacies 4, indicating that euxinic conditions persisted and pushed all the way updip to nearshore environments. The Upper Cow Creek is diluted by siliciclastic influx, and this trend can be observed within the chemofacies partitioning, where the calcium-enriched chemofacies 1 is actually surpassed due to the Ca-depleted sandstones in the lower portion of the Lower Cow Creek.

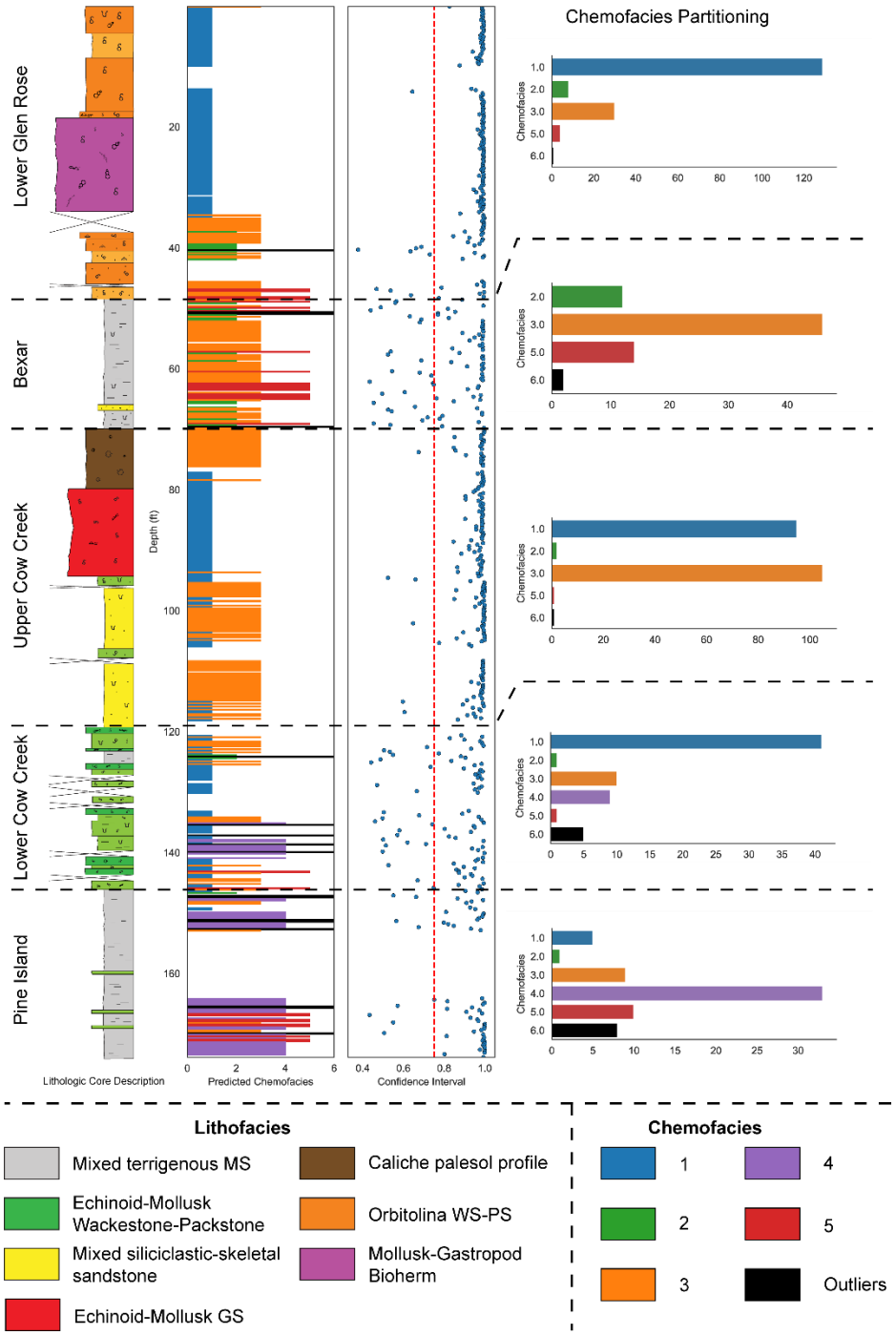

Figure 4.12: Core description, predicted chemofacies, neural network confidence intervals, and chemofacies partitioning within each respectively labeled Member. Guadalupe River Damsite 7-1.

Canyon Dam Chemofacies

The Canyon Dam is another shoreline-proximal well, located in Comal County. Again, the Pine Island Member is associated with a dominant partitioning of chemofacies 4, showing consistent encroachment of euxinic conditions across the San Marcos Arch. Similarly to the Guadalupe River Damsite #7-1 well, nearshore siliciclastics end up becoming the dominant chemofacies in the Upper Cow Creek Member. The mean confidence interval of the neural model was 94%, further showing a high level of applicability of the chemofacies scheme originally derived from the Dix well across the dataset.

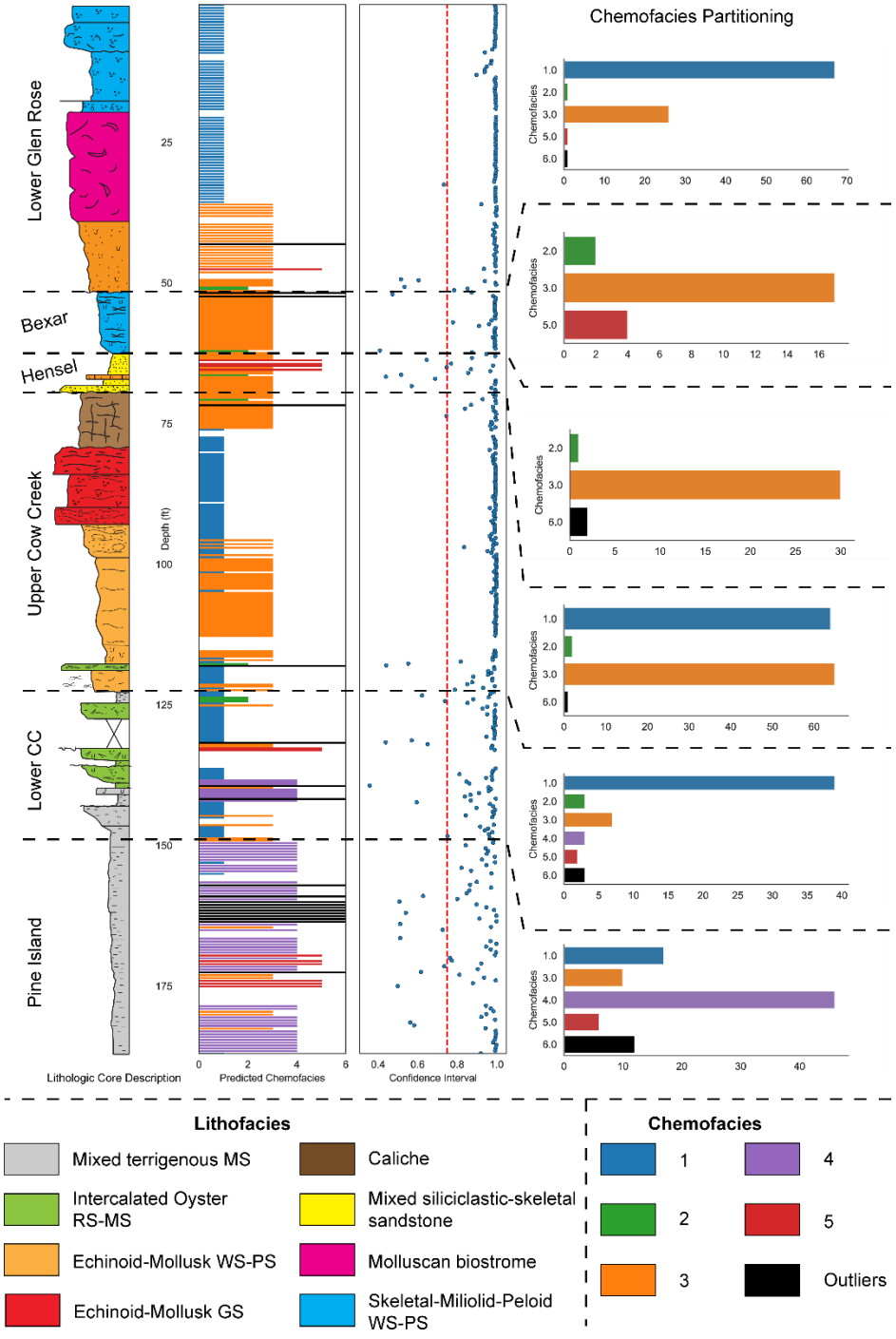

Figure 4.13: Core description, predicted chemofacies, neural network confidence intervals, and chemofacies partitioning within each respectively labeled Member. Canyon Dam. Core description after Kerans.

Chapter 5: Depositional Setting and Oceanic Anoxic Events

DEPOSITIONAL SETTING OF THE PEARSALL FORMATION

The onset of global peak OAE-1a environmental stressors are likely to have been rapid, on the scale of ~27 to 44 kyr, with subsequently slow recovery, with effects lasting more than 1.0 Myr after the peak (Li et al., 2008). The Pearsall Formation was profoundly affected by OAE-1a, a set of forcings which manifested in the deposition of the Pine Island shale but also in the prevailing oceanographic conditions that persisted through the Cow Creek until the end-Cow Creek subaerial exposure event. Transgression and mudstone deposition in the Bexar Member followed this sequence boundary. Primary oceanographic recovery from OAE-1a was thereby punctuated in an incomplete state, with a secondary phase of recovery beginning with the Bexar composite sequence, which continued to develop in the ensuing Glen Rose composite sequence.

Terminology and designations drawn for oceanographic conditions in the following figures (oxic, dysoxic, suboxic, anoxic) are adapted after Canfield and Themdrup (2009), and Tyson and Pearson (1991). Those distinctions are as follows: (1) dysoxic conditions are associated with nitrogenous reduction processes and dysaerobic biofacies associations; (2) suboxic conditions are associated with manganous and ferruginous reduction processes and quasi-anaerobic biofacies; (3) euxinic conditions associated with sulfidic reduction processes and anaerobic biofacies. Dominant chemofacies derived from compiled chemofacies analysis of all cores, supported by physical stratigraphic observations, were used to create maps of the overall oceanographic depositional conditions experienced during the deposition of each member.

Pine Island Member chemofacies partitioning

The Pine Island Member is heavily dominated by chemofacies 4 in the San Marcos Arch and Pearsall Arch areas, even in the most shoreline-proximal wells. This consistent chemofacies partitioning indicates sustained euxinic bottom-water conditions and can be attributed to poor oceanographic circulation as far shoreward as the San Marcos Arch and the margins of the Llano uplift. In comparison, data from the Pearsall Arch area are much more heterogeneous, with high-frequency cycling between chemofacies 4 and 5, indicating cyclic suboxic and euxinic conditions. While this area does not appear to reach fully oxygenated bottom-water conditions, the data indicate a degree of open ocean water interchange with the euxinic interior water body. This difference in water geochemistry, even during peak OAE-1a stressed conditions, lends credence to both the importance of ocean water circulation in the prevailing geochemistry of the regional water column, and the idea that the more advanced Cow Creek Member recovery achieved in the Pearsall Arch area may have started with more advantageous starting conditions from Pine Island time.

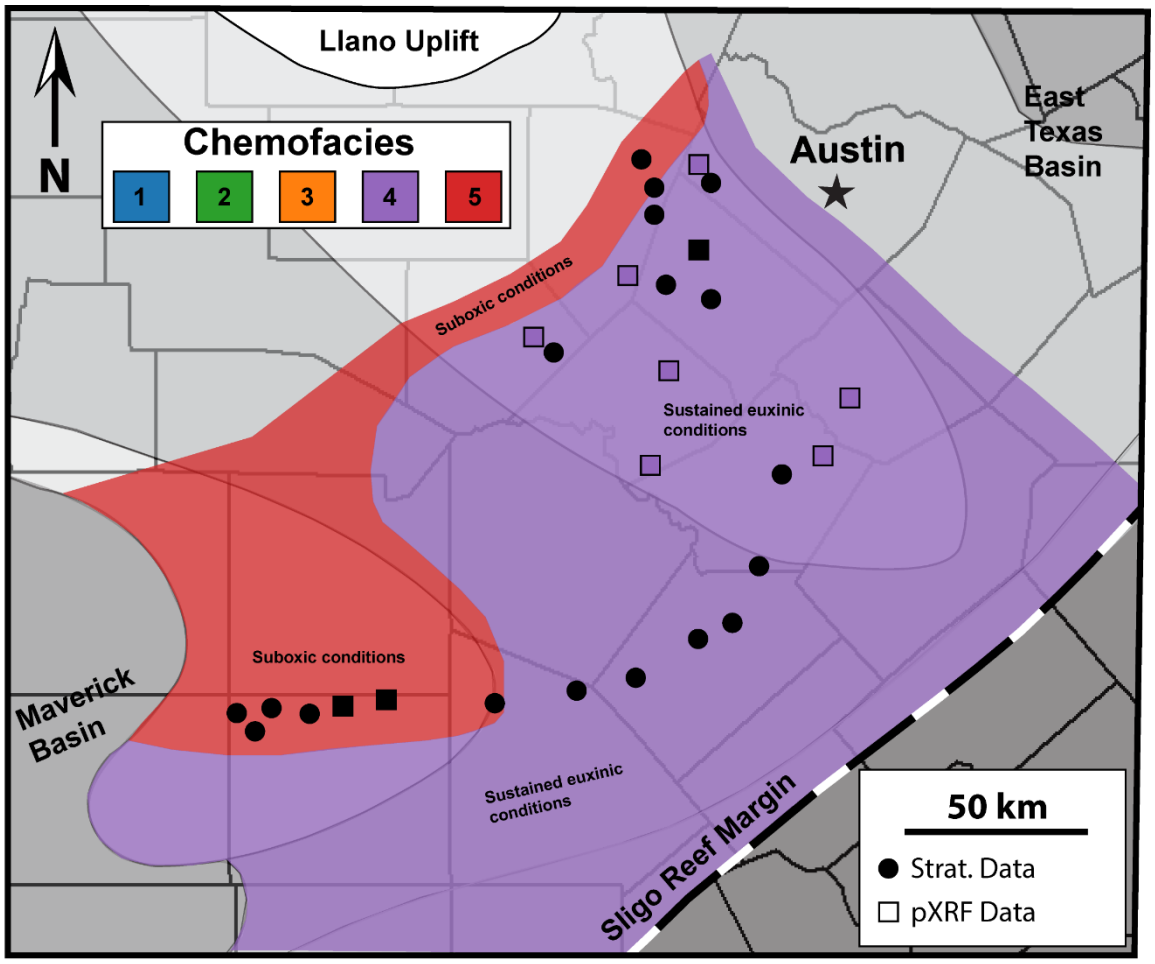

Figure 5.1: Pine Island Member depositional condition map, with conceptual water body oxygenation zones derived from local pXRF and stratigraphic datapoints.

Cow Creek chemofacies partitioning

The Cow Creek Member subset of the pXRF datasets show chemofacies partitioning consistently dominated by chemofacies 1, indicating prevalence of Ca enriched, clean carbonate facies (Figures 4.9, 4.10, 5.2). This observation is reinforced by lithofacies characterization of the shallow water shoreface carbonate factory proximally. Distal wells are instead characterized by an oncolitic carbonate factory. The depositional implications held by these facies, and the chemofacies assignment prescribed, need to be investigated more carefully in order to properly interpret these results.

The geological significance of oncoids as an environmental indicator is somewhat poorly understood. However, oncoids have been observed to be in close relationship to mass extinction events interpreted as recording rapid colonization and ecological expansion of microbes in highly stressed environments (Qvarnstrom, 2012; Zhang et al., 2014). Petrographic analysis for this study illustrates that a diverse, and specialized paleoecologic community is represented by the Cow Creek oncoids. Oncoid laminae are commonly colonized by encrusting forams and serpulid worm tubes. The encrusting communities between oncoids and other hard substrates (e.g. firm-grounds) has been shown to be very similar (Wilson and Palmer, 1990; Taylor and Wilson, 2003). In the Polish Jura, oncoids of middle Jurassic age have a similarly complex epibiont association, with 22 distinct organism classes being found to encrust the oncoids (Zaton et al., 2011). These organisms included encrusting foraminifera, corals, worm tubes, bryozoans, bivalves, and brachiopods.

Oncolites in the San Marcos area are highly pyritic and red stained in comparison to oncolites in the Pearsall Arch area. Oncoid cortices contain a prevalent amount of pyrite throughout (up to 10%), indicating periods of growth consistent with euxinic bottom-water conditions. Free sulfide associated with euxinic conditions is consistent with the formation

of pyritic framboids observed within the growth-cortices of the oncoid grains (Zhang et al., 2015). Subsequent cycling between euxinic and suboxic conditions would then allow for the oxidization of the iron in the pyrite framboids, leading to the pervasive red staining observed in the San Marcos Arch oncoids. This comparison between regions indicates a more severely oxygen-depleted water column persisting around the San Marcos Arch during Cow Creek Member deposition. The micritic matrix is notably lacking of pyrite, differentiating the matrix and the constituent coated grains. Furthermore, shelter cavities related to percolation of mud from the surface down through the oncoids is common throughout all thin sections analyzed. These observations indicate that the matrix emplacement is from late infiltration, post-dating the reducing conditions experienced during oncolite accumulation. This case signifies the importance of using an integrated workflow when using pXRF data, where an understanding of the physical stratigraphy and petrography must be used in unison with geochemistry. While pXRF data can reveal great insight into the geochemical portion of carbonate stratigraphy, especially in mud dominated packages, it is important to recognize the depositional context and what that means for the interpretation of the elemental abundance data. In this case, with the pXRF instrument collecting scans of the mud-dominated matrix of the oncoid rudstone lithofacies, the geochemical data is going to be representative of the oxygenated deposition of the mud, rather than the euxinic deposition and growth of the oncoids themselves. For this reason, the map in Figure 5.2 displays the Mercer and Dix wells as being deposited within a zone of cyclic suboxic and euxinic conditions, rather than chemofacies 1. Oceanographic conditions then improve updip depositionally, towards cyclic dysoxic conditions and finally fully oxygenated conditions in shoreline proximal settings. This patterned hierarchy of oceanographic conditions is expected to be consistent between both the San Marcos and Pearsall areas, with poorer oceanographic conditions extending further

into the platform interior shown schematically as an embayment between the two relative paleotopographic features (Figure 5.2).

Furthermore, the deposition of Cow Creek stromatoporoid-coralgal patch reefs in the Pearsall Arch area, such as the buildup observed in the Tenneco #1 Sirianni in Frio County, is interpreted to be the result of sufficient accommodation space and ocean water circulation that allowed for the nucleation and aggradation of reefal assemblages in localized oligotrophic and oxygenated oceanographic conditions, which is reinforced by the observations gained by analysis and comparisons between the oncoids representative of each locale.

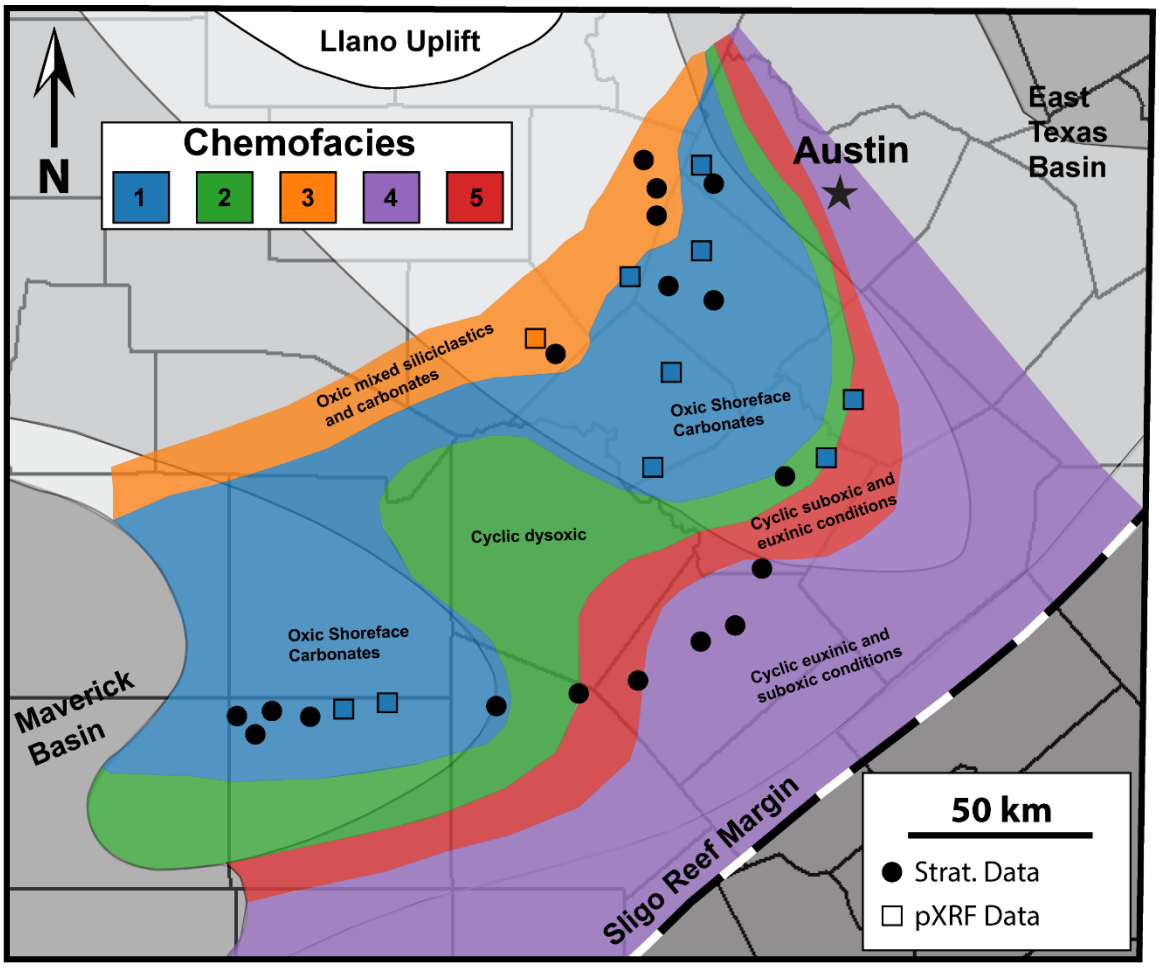

Figure 5.2: Cow Creek Member depositional condition map, with conceptual water body oxygenation zones derived from local pXRF and stratigraphic datapoints.

Bexar chemofacies partitioning

The Bexar Member is the most heterogeneous in terms of chemofacies partitioning. Within the Dix well for example, several pulses of euxinia and subsequent suboxic to dysoxic cycling are observed (Figure 4.9). Chemofacies stacking patterns in the Bexar provide a stark example as to the nuanced geochemical variability that is otherwise largely invisible in a standard physical core characterization. Despite highly detailed and technically proficient core logging techniques, this organization and visualization of the pXRF data is able to increase the value of the stratigraphic interpretation and framework that would be otherwise lost in the largely visually nondescript mudstone sequence.

Similar to the Pine Island deposition, dysoxic-suboxic-euxinic bottom-water conditions encroached higher onto both the San Marcos and Pearsall Arch areas, albeit to a much lesser severity (Figure 5.3). Suppression of the carbonate factory once again persisted on the San Marcos Arch, with even oxic chemofacies intervals being characterized by argillaceous and detrital enrichment rather than calcium enrichment. Contrary to the consistently argillaceous deposition during the Bexar on the San Marcos Arch, Bexar deposition on the Pearsall arch is characterized by discrete third order sequences, with shoaling upward carbonate complexes prograding into the Maverick basin. Schematic extent of these shoal-water complexes is delineated by chemofacies 1, indicating clean carbonate deposition in well oxygenated bottom-water conditions.

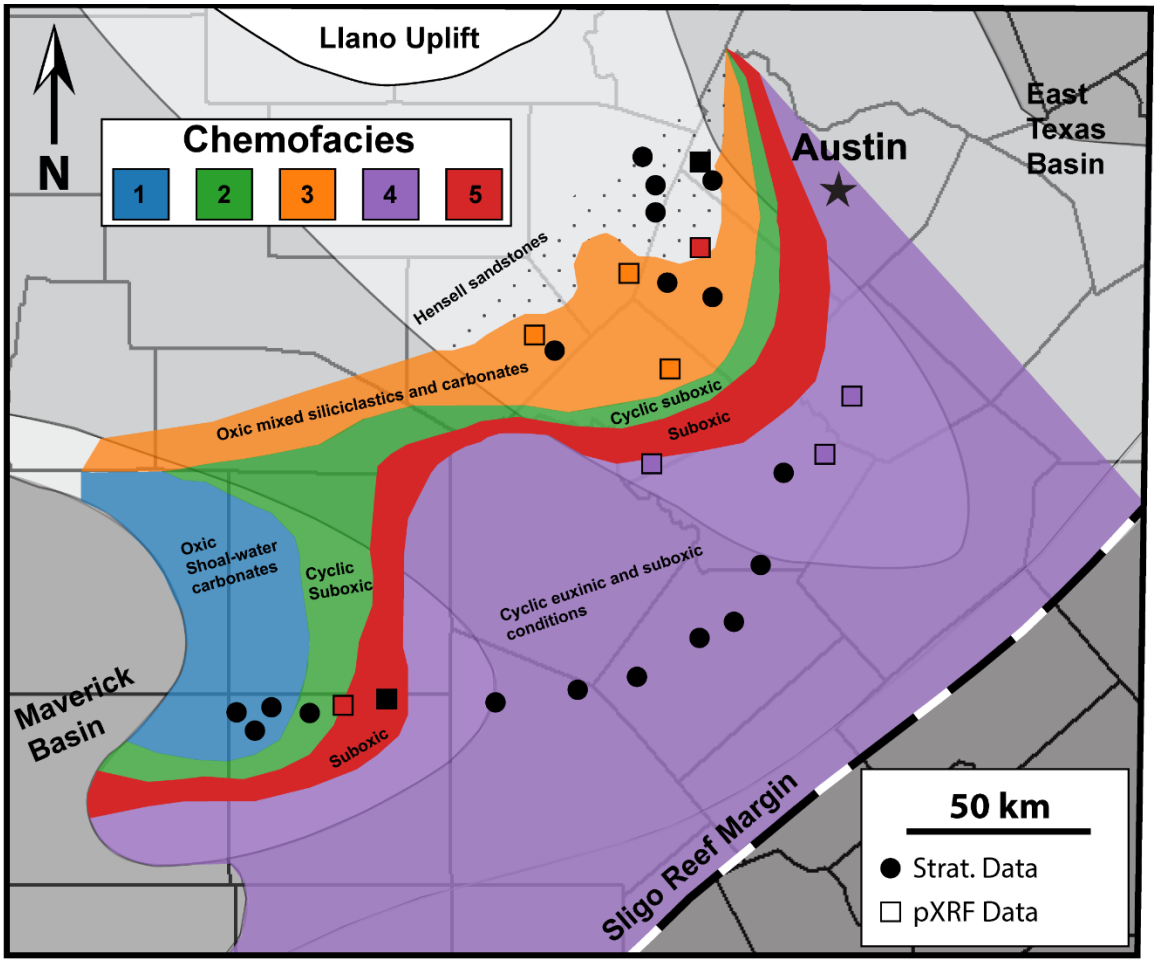

Figure 5.3: Bexar Member depositional condition map, with conceptual water body oxygenation zones derived from local pXRF and stratigraphic datapoints.

DEPOSITIONAL SETTING OF THE LOWER GLEN ROSE MEMBER

The Lower Glen Rose Formation represents the second phase of recovery and equilibrium phase following the end Cow-Creek subaerial exposure event as well as minor ecological forcings of the OAE-1b event. Unlike the partial recovery recorded by the Cow Creek Member of the Pearsall Formation (before the end-Cow Creek subaerial exposure event), the Lower Glen Rose system is successful in achieving complete recovery of the carbonate factory. A broad shallow-shelf influenced by local coral-rudist patch reef development marks the return to a system that is able to fill available accommodation and eventually progrades to the former shelf margin (Bay, 1982; Aconcha, 2008; Phelps et al., 2014; this study). Lower Glen Rose coral-rudist patch reef development identified in this study are likely near-coeval with other patch reef complexes identified in the Maverick Basin, and patch reef complexes at Paul Spur in Arizona (Scott and Warzeski, 1993; Hartshorne, 1989; Hattori et al., 2019). This healthy and diverse carbonate factory of the later recovery phase is continued through the Upper Glen Rose Member until the ultimate re-establishment of a reef-rimmed platform with a rudist-dominated margin in the Stuart City Formation.

Lower Glen Rose chemofacies partitioning

Chemofacies and stratigraphic interpretation of the Lower Glen Rose Formation lead to the conceptual map shown in Figure 5.4. By this stage of the recovery story, we can see the decrease in aerial extent of all non-oxygenated zones, observed by the shift in chemofacies partitioning as well as a clear increase of carbonate lithofacies within the carbonate factory of Glen Rose time. Oxic conditions now occupy most of the San Marcos and Pearsall Arch areas, and more argillaceous facies observed in the Schmidt well are still consistent to have formed under well circulated oceanographic conditions.

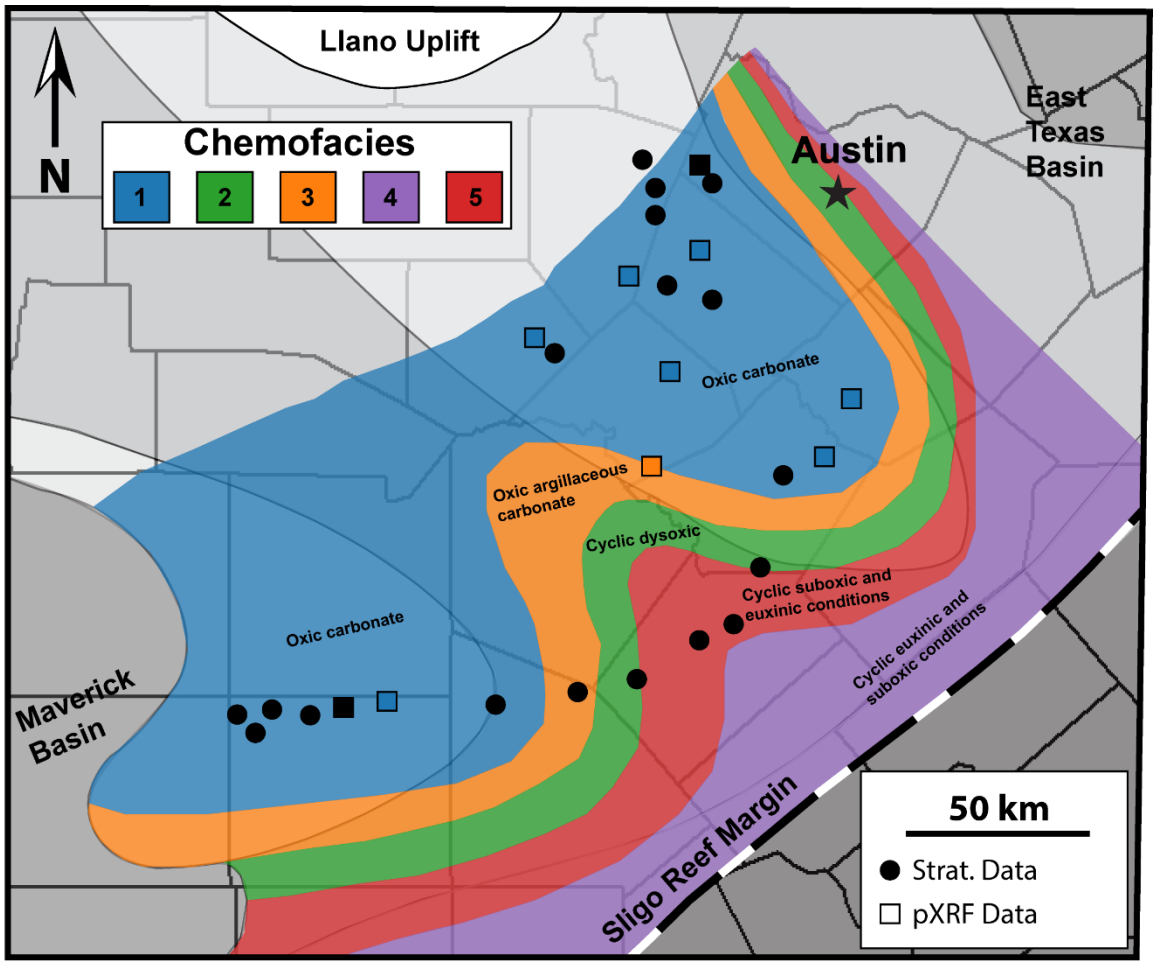

Figure 5.4: Lower Glen Rose Member depositional condition map, with conceptual water body oxygenation zones derived from local pXRF and stratigraphic datapoints.

Chapter 6: Conclusions

This study aimed to document the recovery of the Comanche platform from OAE-1a, and to clarify the stratal architecture of the Aptian and Albian composite sequences between the San Marcos Arch and the Pearsall Arch. The regional cross section presented in this work encompasses three composite sequences: The James (Aptian) composite sequence, the Bexar (Aptian-Albian) composite sequence, and the Glen Rose (Albian) composite sequence, in agreement with the pre-existing Comanchean sequence stratigraphic framework outlined by Phelps et al., (2014).

In addition, the study sought to supplement physical stratigraphic observations with analysis of the growing portfolio of pXRF data available at the Bureau of Economic Geology. Generation of new, and the compilation of pre-existing pXRF data available for the Pearsall Formation as well as recent development of the CorePy project has led to the establishment of a workflow using deep learning to directly compare multivariate statistical learnings gained from Principal Component Analysis and segmentation of one well, to neighboring wells. This direct comparison between pXRF datasets has otherwise been difficult to approach, due to the high dimensionality of combined major and trace elemental abundance datasets, and the general limitations associated with using any singular trace element proxy for depositional environment inferences, as well as the individualized nature of PCA segmentation methods per dataset (Dean et al., 2012; Gebregiorgis et al., 2020). Despite being applied to a highly complex system, early implementation of deep learning was able to populate an internally consistent chemofacies classification scheme across shelf environments with an overall confidence interval of 82%.

The impact that OAE-1a had on the Comanche Platform in South Texas was observed to be asymmetric, with a sharp and presumably rapid demise tied to the onset and

rise of peak OAE stressed conditions and full suppression of the carbonate factory (deposition of the Pine Island Shale). The recovery signal, however, is a significantly longer-lived process. The first reef builders following the OAE-1a driven crisis are coral stromatoporoids patch reefs, such as those seen in the Sirianni and Wilbeck cores, not rudist reefs. In fact, rudist reefs and bioherms do not begin to appear until into the Lower Glen Rose Member. It is not until deposition of the Upper Glen Rose-equivalent Stuart City margin that a caprinid-rich carbonate factory akin to the pre-OAE-1a Sligo reef margin returns to dominance. Similarly, the echinoid-mollusk faunal assemblage characteristic of proximal and distal Cow Creek Member deposition generally persists until the Lower Glen Rose Member, with very slow and incremental increases in faunal diversity.

Variability between the San Marcos Arch and the Pearsall Arch lends support to the notion that different regions within the same platform are likely to experience a disparate severity of ecological forcings from OAEs, even those with a globally documented signature such as OAE-1a. An early hypothesis that the starting conditions of carbonate factory recovery in both San Marcos Arch and Pearsall Arch areas were identical same following peak OAE-1a conditions was refuted, with pXRF data and stratigraphic observations suggesting that the two regions experienced significantly different oceanographic conditions during Pine Island deposition, with reduced severity of anoxia in the Pearsall area. On a regional scale, two areas may go on to experience different phases of carbonate factory recovery due to either the initial reduced impact of the OAE, or a set of variables facilitating early nucleation and more complete carbonate accumulation in subsequent stages of carbonate factory recovery. This variability may be due to a combination of oceanographic circulation patterns, the degree of shelf restriction, the degree of terrigenous influx, and basin geometry. In the case of the Southern Texas expression of OAE-1a, it appears that the Pearsall Arch area was able to reach a more full

recovery of the carbonate factory during the James composite sequence due to a combination of available accommodation space and a more well circulated water column in comparison to the San Marcos Arch area. Indeed, the complexity of OAE records are not simply seen in the "anoxic shales" they became infamous for but is also documented and persistent through the nuanced geochemical signals and the evolution of dominating carbonate factory components, with a significant amount of superimposed regional variability inherent even in globally recognized perturbations such as OAE-1a.

Through statistical interrogation of pXRF data using CorePy, five chemofacies were identified. These chemofacies represent genetically similar assemblages of elemental abundance present in the core sequences. The Dix core was chosen as a type-core, which was then used as a training dataset for a deep learning neural network. The novel approach of using a neural model to take established chemofacies from a type-core and applying a self-consistent chemofacies framework across available core control represents a large step forward in the quantification, comparison, and applied usage of pXRF data as a tool for the characterization of highly complex systems. This workflow provides a means of leveraging learnings taken from the data processing and segmentation provided by principal component analysis and provides a statistical means to identify chemofacies between wells.

The deep learning model performed with an overall confidence interval of 89.7%. This confidence interval includes the application of the neural network to more shoreline-proximal cores in the San Marcos Arch area that contain lithofacies assemblages that are not present in the Gulf Dix dataset used to train the neural model. In the future, the training dataset should include examples of all chemofacies end members, and therefore, care should be taken to include clean siliciclastic intervals associated with the Hensel Formation in shoreline-proximal wells in the Northern San Marcos Arch area. The core implementations nonetheless show promise not only as a proof of concept workflow but as

the possible way forward within the discipline of pXRF data analysis. Neural networks allow for cross well comparison of PCA organized data to a level that has previously not been possible, and features inherent risking of assigned chemofacies, through the explicit generation of a confidence interval for the categorical distinction prescribed to each and every pXRF scan.

While furthered and nuanced neural model refinement is outside of the scope of this written study, the design philosophy and code architecture of CorePy is arranged in a way that is flexible to all input pXRF datasets and facilitates future feature expansions and neural model evolutions and enhanced training techniques. One example of a future expansion of this integrative methodology could include the ability for export of 1-D chemofacies logs to industry standard well log visualization software to allow for the development and population of a 3D geologic model with chemofacies. This would allow existing 3D subsurface models to incorporate high resolution chemofacies trends and relationships that may help inform important source and reservoir property characteristics for any given asset with pXRF datasets. Within this scheme, the assignment and classification of rock intervals by chemofacies is the starting point, rather than the end goal, which would instead be to build upon this classification scheme through the correlation and fitting of rock and fluid properties to chemofacies in order to develop fully integrative subsurface models.

Appendix

Appendix materials can be accessed via the online thesis repository.

References

Aconcha, E.S., Kerans, C. and Zeng, H. 2008. Seismic Geomorphology Applied to Lower Glen Rose Patch Reefs in the Maverick Basin, Southwest Texas. Transactions - Gulf Coast Association of Geological Societies, 58: 3-23.

Amodio, S., V. Ferreri, B. D'Argenio, H. Weissert, and M. Sprovieri, 2008, Carbon-isotope stratigraphy and cyclostratigraphy of shallow-marine carbonates: the case of San Lorenzello, Lower Cretaceous of southern Italy: Cretaceous Research, v. 29, no. 5–6, p. 803–813.

Amsbury, D. L., 1996, Pearsall (Aptian Cretaceous) Subsurface to Outcrop Sequence Stratigraphy, Central Texas: v. 46, p. 1–7.

Amsbury, D. L., 1974, Stratigraphic petrology of Lower and Middle Trinity rocks on the San Marcos platform, south-central Texas: Geoscience and man, v. 8, p. 1–35.

Arthur, M. A., W. E. Dean, and L. M. Pratt, 1988, Geochemical and climatic effects of increased marine organic carbon burial at the Cenomanian/Turonian boundary, 6192: Nature, v. 335, no. 6192, p. 714–717.

Arthur, M. A., and B. B. Sageman, 1994, Marine black shales: depositional mechanisms and environments of ancient deposits: Annual Review of Earth and Planetary Sciences, v. 22, no. 1, p. 499–551.

Arthur, M. A., W. E. Dean, and D. A. V. Stow, 1984, Models for the deposition of Mesozoic-Cenozoic fine-grained organic-carbon-rich sediment in the deep sea: Geological Society, London, Special Publications, v. 15, no. 1, p. 527–560.

Arthur, M. A., and S. O. Schlanger, 1979, Cretaceous "oceanic anoxic events" as causal factors in development of reef-reservoired giant oil fields: AAPG bulletin, v. 63, no. 6, p. 870–885.

Bay, A. R., 1982, Evolution and Porosity of Carbonate Shoaling Cycles Lower Cretaceous-Lower Glen Rose, South Texas. Transactions – Gulf Coast Association of Geological Societies, 32: 101-119.

Bay Jr, T. A., 1977, Lower Cretaceous stratigraphic models from Texas and Mexico: Applications to subsurface Exploration (Eds D.G. Bebout and R.G. Loucks), Report of Investigations No 89, pp. 12-30. University of Texas at Austin, Bureau of Economic Geology, Austin, TX.

Bebout, D. G., 1977, Sligo and Hosston Depositional Patterns, Subsurface of South Texas. Report of Investigations – Texas, University, Bureau of Economic Geology, 79-96.

Bebout, D. G., and R. G. Loucks, 1977, Cretaceous carbonates of Texas & Mexico: applications to subsurface exploration: Texas Bureau of Economic Geology Report of investigations No 89, Austin, TX, 332 pp.

Bebout, D. G., and R. A. Schatzinger, 1978, Distribution and geometry of an oolite-shoal complex-Lower Cretaceous Sligo Formation, South Texas: Gulf Coast Assoc. Geol. Socs: Trans, v. 28, p. 33–45.

Berner, R. A., 1984, Sedimentary pyrite formation: An update: Geochimica et Cosmochimica Acta, v. 48, no. 4, p. 605–615.

Bover-Arnal, T., R. Salas, J. Guimerà, and J. A. Moreno-Bedmar, 2014, Deep incision in an Aptian carbonate succession indicates major sea-level fall in the Cretaceous: Sedimentology, v. 61, no. 6, p. 1558–1593.

Bralower, T. J., E. CoBabe, B. Clement, W. V. Sliter, C. L. Osburn, and J. Longoria, 1999, The record of global change in mid-Cretaceous (Barremian-Albian) sections from the Sierra Madre, northeastern Mexico: The Journal of Foraminiferal Research, v. 29, no. 4, p. 418–437.

Bralower, T. J., P. D. Fullagar, C. K. Paull, G. S. Dwyer, and R. M. Leckie, 1997, Mid-Cretaceous strontium-isotope stratigraphy of deep-sea sections: Geological Society of America Bulletin, v. 109, no. 11, p. 1421–1442.

Bralower, T. J., 1988, Calcareous nannofossil biostratigraphy and assemblages of the Cenomanian-Turonian boundary interval: Implications for the origin and timing of oceanic anoxia: Paleoceanography, v. 3, no. 3, p. 275–316.

Breit, G. N., and R. B. Wanty, 1991, Vanadium accumulation in carbonaceous rocks: a review of geochemical controls during deposition and diagenesis: Chemical Geology, v. 91, no. 2, p. 83–97.

Buetti-Dinh, A. et al., 2019, Deep neural networks outperform human expert's capacity in characterizing bioleaching bacterial biofilm composition: Biotechnology Reports, v. 22, p. e00321.

Burkholder, J., and D. Lumsden, 1973, Petrographic analysis of a subsurface portion of the Glen Rose Formation (Lower Cretaceous), South Texas. Transactions – Gulf Coast Association of Geological Societies, 23: 278-287.

Calvert, S. E., and T. F. Pedersen, 2007, Chapter fourteen elemental proxies for palaeoclimatic and palaeoceanographic variability in marine sediments: interpretation and application: Developments in Marine Geology, v. 1, p. 567–644.

Clarke, L. J., and H. C. Jenkyns, 1999, New oxygen isotope evidence for long-term Cretaceous climatic change in the Southern Hemisphere: Geology, v. 27, no. 8, p. 699–702.

Coogan, A. H., 1977, Early and middle Cretaceous Hippuritacea (rudists) of the Gulf Coast. In: Cretaceous Carbonates of Texas and Mexico: Applications to Subsurface Exploration (Eds D.G. Bebout and R.G. Loucks), Texas Bureau of Economic Geology Report of Investigations No 89, pp. 32-70.

Cook, T. D., 1979, Exploration history of south Texas Lower Cretaceous carbonate platform: AAPG Bulletin, v. 63, no. 1, p. 32–49.

Dean, J., G. Corrado, R. Monga, K. Chen, M. Devin, M. Mao, M. Ranzato, A. Senior, P. Tucker, and K. Yang, 2012, Large scale distributed deep networks, *in* Advances in neural information processing systems: p. 1223–1231.

Dunham, R.J. 1962. Classification of carbonate rocks according to depositional texture: in (Ham, W.E., eds.), Classification of carbonate rocks: AAPG Memoir 1: 62-84.

Erba, E., 1994, Nannofossils and superplumes: the early Aptian "nannoconid crisis": Paleoceanography, v. 9, no. 3, p. 483–501.

Erba, E., 2004, Calcareous nannofossils and Mesozoic oceanic anoxic events: Marine Micropaleontology, v. 52, no. 1, p. 85–106.

Erba, E., C. Bottini, H. J. Weissert, and C. E. Keller, 2010, Calcareous Nannoplankton Response to Surface-Water Acidification Around Oceanic Anoxic Event 1a: Science, v. 329, no. 5990, p. 428–432.

Ewing, T. E., and N. C. Rosen, 2003, Review of the tectonic history of the lower Rio Grande border region, south Texas and Mexico, and implications for hydrocarbon exploration: Society of Independent Professional Earth Scientists Newsletter, v. 40, p. 16–21.

Ewing, T. E., 2010, Pre-Pearsall geology and exploration plays in South Texas. Transactions – Gulf Coast Association of Geological Societies, 60: 241-260.

Farley, B. G., and W. A. Clark, 1954, Simulation of self-organizing systems by digital computer: Trans. IRE Prof. Group Inf. Theory.

Fawaz, H. I., G. Forestier, J. Weber, L. Idoumghar, and P.-A. Muller, 2019, Deep Neural Network Ensembles for Time Series Classification: 2019 International Joint Conference on Neural Networks (IJCNN), p. 1–6.

Föllmi, K. B., A. Godet, S. Bodin, and P. Linder, 2006, Interactions between environmental change and shallow water carbonate buildup along the northern Tethyan margin and their impact on the Early Cretaceous carbon isotope record: Paleoceanography, v. 21, no. 4.

Föllmi, K. B., H. Weissert, M. Bisping, and H. Funk, 1994, Phosphogenesis, carbon-isotope stratigraphy, and carbonate-platform evolution along the Lower Cretaceous northern Tethyan margin: Geological Society of America Bulletin, v. 106, no. 6, p. 729–746.

Forgotson Jr, J. M., 1957, Stratigraphy of Comanchean Cretaceous Trinity Group: AAPG Bulletin, v. 41, no. 10, p. 2328–2363.

Forkner, R., X. Sun, and C. Kerans, 2019, Impacts of Apto-Albian OAE on the Comanche Shelf, Central Texas, *in* 2019 AAPG Annual Convention and Exhibition.

Frey, F. A., D. Weis, H.-J. Yang, K. Nicolaysen, H. Leyrit, and A. Giret, 2000, Temporal geochemical trends in Kerguelen Archipelago basalts: evidence for decreasing magma supply from the Kerguelen plume: Chemical Geology, v. 164, no. 1–2, p. 61–80.

Goldhammer, R.L. and C.A. Johnson, 2001, Middle Jurassic-Upper Cretaceous Paleogeographic evolution and sequence-stratigraphic framework of the Northwest Gulf of Mexico rim. In: The western Gulf of Mexico basin; tectonics, sedimentary basins, and petroleum systems (Eds C. Bartolini, R.T. Buffler and A. Cantu-Chapa), AAPG Memoir 75, pp. 45-81. American Association of Petroleum Geologists: Tulsa, OK, United States, Tulsa, OK.

Gebregiorgis, D., L. Giosan, E. C. Hathorne, P. Anand, K. Nilsson-Kerr, A. Plass, A. Lückge, S. C. Clemens, and M. Frank, 2020, What Can We Learn From X-Ray Fluorescence Core Scanning Data? A Paleomonsoon Case Study: Geochemistry, Geophysics, Geosystems, v. 21, no. 2, p. e2019GC008414.

Grötsch, J., I. A. N. Billing, and V. Vahrenkamp, 1998, Carbon-isotope stratigraphy in shallow-water carbonates: implications for Cretaceous black-shale deposition: Sedimentology, v. 45, no. 4, p. 623–634.

Hartshorne, P. M., 1989, Facies architecture of a Lower Cretaceous coral-rudist patch reef, Arizona: Cretaceous Research, v. 10, no. 4, p. 311–336.

Hastings, D. W., S. R. Emerson, and A. C. Mix, 1996, Vanadium in foraminiferal calcite as a tracer for changes in the areal extent of reducing sediments: Paleoceanography, v. 11, no. 6, p. 665–678.

Hattori, K. E., C. Kerans, and R. C. Martindale, 2019, Sequence Stratigraphic and Paleoecologic Analysis of an Albian Coral-Rudist Patch Reef, Arizona, USA: Palaios, v. 34, no. 12, p. 600–615.

Herrle, J. O., P. Kößler, O. Friedrich, H. Erlenkeuser, and C. Hemleben, 2004, High-resolution carbon isotope records of the Aptian to Lower Albian from SE France and the Mazagan Plateau (DSDP Site 545): a stratigraphic tool for paleoceanographic and paleobiologic reconstruction: Earth and Planetary Science Letters, v. 218, no. 1–2, p. 149–161.

Holland, H. D., 1984, The chemical evolution of the atmosphere and oceans: Princeton University Press.

Hotelling, H., 1933, Analysis of a complex of statistical variables into principal components.: Journal of educational psychology, v. 24, no. 6, p. 417.

Huck, S., N. Rameil, T. Korbar, U. Heimhofer, T. D. Wieczorek, and A. Immenhauser, 2010, Latitudinally different responses of Tethyan shoal-water carbonate systems to the Early Aptian oceanic anoxic event (OAE 1a): Sedimentology, v. 57, no. 7, p. 1585–1614.

Hull, D. C., 2011, Stratigraphic architecture, depositional systems, and reservoir characteristics of the Pearsall shale-gas system, Lower Cretaceous, South Texas, thesis.

Inden, R. F., and C. H. Moore, 1983, Beach Environment. AAPG Memoir, 33: 211-265.

Jenkyns, H. C., 1995, Carbon-isotope stratigraphy and paleoceanographic significance of the Lower Cretaceous shallow-water carbonates of Resolution Guyot, Mid-Pacific Mountains, *in* Proceedings of the Ocean Drilling Program, Scientific Results: Ocean Drilling Program, College Station, p. 99–104.

Jenkyns, H. C., 2010, Geochemistry of oceanic anoxic events: REVIEW: Geochemistry, Geophysics, Geosystems, v. 11, no. 3, p. n/a-n/a.

Kerans, C., 2002, Styles of rudist buildup development along the northern margin of the Maverick Basin, Pecos River canyon, Southwest Texas. Transactions – Gulf Coast Association of Geological Sciences.

Kerans, C. and R.G. Loucks, 2002, Stratigraphic setting and controls on occurrence of high-energy carbonate beach deposits; Lower Cretaceous of the Gulf of Mexico. Transactions – Gulf Coast Association of Geological Societies, 52: 517-526.

Kerans, C., C Zahm, and others, The Aptian Composite Sequence in Texas – Shoreline to Deep Shelf Profile of OAE 1A, BEG Reservoir Characterization Research Laboratory Annual Field Guide, Guidebook 2014, 57 p.

Larson, R. L., 1991, Latest pulse of Earth: Evidence for a mid-Cretaceous superplume: Geology, v. 19, no. 6, p. 547–550.

Larson, T. E., R.G. Loucks, E. J. Sivil, C. K. Zahm, submitted (2020), Austin Chalk chemomineral facies classification through integrated data analytics and high-resolution x-ray fluorescence characterization, AAPG Bulletin.

Leckie, R. M., T. J. Bralower, and R. Cashman, 2002, Oceanic anoxic events and plankton evolution: Biotic response to tectonic forcing during the mid-Cretaceous: Paleoceanography, v. 17, no. 3, p. 13-1-13–29.

LeCun, Y., Y. Bengio, and G. Hinton, 2015, Deep learning, 7553: Nature, v. 521, no. 7553, p. 436–444.

Li, Y.-X., T. J. Bralower, I. P. Montañez, D. A. Osleger, M. A. Arthur, D. M. Bice, T. D. Herbert, E. Erba, and I. Premoli Silva, 2008, Toward an orbital chronology for the early Aptian Oceanic Anoxic Event (OAE1a, ~120 Ma): Earth and Planetary Science Letters, v. 271, no. 1, p. 88–100.

Lozo, F. E., and C. I. Smith, 1964, Revision of Comanche Cretaceous stratigraphic nomenclature, southern Edwards Plateau, southwest Texas.

Lozo, F. E., and F. L. Stricklin Jr, 1956, Stratigraphic notes on the outcrop basal Cretaceous, central Texas.

Loucks, R.G., 1976, Pearsall Formation, Lower Cretaceous, south Texas: depositional facies and carbonate diagenesis and their relationship to porosity, The University of Texas at Austin, Austin, 362 pp.

Loucks, R. G., 1977, Porosity development and distribution in shoal-water carbonate complexes–subsurface Pearsall Formation (Lower Cretaceous) south Texas.

Maurer, F., F. S. P. van Buchem, G. P. Eberli, B. J. Pierson, M. J. Raven, P.-H. Larsen, M. I. Al-Husseini, and B. Vincent, 2013, Late Aptian long-lived glacio-eustatic lowstand recorded on the Arabian Plate: Terra Nova, v. 25, no. 2, p. 87–94.

Mancini, E. A., and T. M. Puckett, 2002, Transgressive-regressive cycles in Lower Cretaceous strata, Mississippi Interior Salt Basin area of the northeastern Gulf of Mexico, USA: Cretaceous Research, v. 23, no. 3, p. 409–438.

Mancini, E. A., and R. W. Scott, 2006, Sequence stratigraphy of Comanchean Cretaceous outcrop strata of northeast and south-central Texas: Implications for enhanced petroleum exploration.

Menegatti, A. P., H. Weissert, R. S. Brown, R. V. Tyson, P. Farrimond, A. Strasser, and M. Caron, 1998, High-resolution δ13C stratigraphy through the early Aptian "Livello Selli" of the Alpine Tethys: Paleoceanography, v. 13, no. 5, p. 530–545.

Meyers, S. R., B. B. Sageman, and T. W. Lyons, 2005, Organic carbon burial rate and the molybdenum proxy: Theoretical framework and application to Cenomanian-Turonian oceanic anoxic event 2: Paleoceanography, v. 20, no. 2.

McCulloch, W. S., and W. Pitts, 1943, A logical calculus of the ideas immanent in nervous activity: The bulletin of mathematical biophysics, v. 5, no. 4, p. 115–133.

Moore, C. H., 1996, Anatomy of a sequence boundary-Lower Cretaceous Glen Rose/Fredericksburg, Central Texas Platform.

Nielsen, M. A., 2015, Neural networks and deep learning: Determination press San Francisco, CA.

Orgeron, S. A., 1995, Salt Tectonism of the US Gulf Coast Basin: New Orleans Geological Society.

Owens, L., and C. Kerans, 2010, Revisiting the Cow Creek Limestone: Facies Architecture and Depositional History of a Greenhouse Strandplain.

Parente, M., G. Frijia, M. D. Lucia, H. C. Jenkyns, R. G. Woodfine, and F. Baroncini, 2008, Stepwise extinction of larger foraminifers at the Cenomanian-Turonian boundary: A shallow-water perspective on nutrient fluctuations during Oceanic Anoxic Event 2 (Bonarelli Event): Geology, v. 36, no. 9, p. 715–718.

Pearson, K., 1901, LIII. On lines and planes of closest fit to systems of points in space: The London, Edinburgh, and Dublin Philosophical Magazine and Journal of Science, v. 2, no. 11, p. 559–572.

Pedregosa, F., G. Varoquaux, A. Gramfort, V. Michel, B. Thirion, O. Grisel, M. Blondel, P. Prettenhofer, R. Weiss, and V. Dubourg, 2011, Scikit-learn: Machine learning in Python: the Journal of machine Learning research, v. 12, p. 2825–2830.

Perkins, B.F., 1974, Paleoecology of a rudist reef complex in the Comanche Creteceous Glen Rose Limestone of central Texas: Geosciences and Man, v. 8, p. 131-174.

Phelps, R. M., C. Kerans, R. O. B. P. Da-Gama, J. Jeremiah, D. Hull, and R. G. Loucks, 2015, Response and recovery of the Comanche carbonate platform surrounding multiple Cretaceous oceanic anoxic events, northern Gulf of Mexico: Cretaceous Research, v. 54, p. 117–144.

Phelps, R. M., C. Kerans, R. G. Loucks, R. O. B. P. Da-Gama, J. Jeremiah, and D. Hull, 2014, Oceanographic and eustatic control of carbonate platform evolution and sequence stratigraphy on the Cretaceous (Valanginian–Campanian) passive margin, northern Gulf of Mexico: Sedimentology, v. 61, no. 2, p. 461–496.

Phelps, R. M., 2011, Middle-Hauterivian to Lower-Campanian sequence stratigraphy and stable isotope geochemistry of the Comanche platform, south Texas, thesis.

Pindell, J. L., and L. Kennan, 2001, Kinematic evolution of the Gulf of Mexico and Caribbean, *in* Transactions of the Gulf Coast Section Society of Economic Paleontologists and Mineralogists (GCSSEPM) 21st Annual Bob F. Perkins Research Conference, Petroleum Systems of Deep-Water Basins, Houston, Texas, December: p. 2–5.

Qvarnström, M., 2012, An interpretation of oncoid mass-occurrence during the Late Silurian Lau Event, Gotland, Sweden: Dissertations in Geology at Lund University.

Raiswell, R., and R. A. Berner, 1985, Pyrite formation in euxinic and semi-euxinic sediments: American Journal of Science, v. 285, no. 8, p. 710–724.

Saito, M. A., and J. W. Moffett, 2002, Temporal and spatial variability of cobalt in the Atlantic Ocean: Geochimica et Cosmochimica Acta, v. 66, no. 11, p. 1943–1953.

Saito, M. A., J. W. Moffett, S. W. Chisholm, and J. B. Waterbury, 2002, Cobalt limitation and uptake in Prochlorococcus: Limnology and Oceanography, v. 47, no. 6, p. 1629–1636.

Scholle, P. A., and M. A. Arthur, 1980, Carbon Isotope Fluctuations in Cretaceous Pelagic Limestones: Potential Stratigraphic and Petroleum Exploration Tool: AAPG Bulletin, v. 64, no. 1, p. 67–87.

Scott, R. W., 1993, Cretaceous Carbonate Platform, US Gulf Coast: Chapter 9. (Eds T.J.A. Simo, R.W. Scott and J.P Masse), AAPG Memoir 56, pp. 97-109).

Scott, R. W., and E. R. Warzeski, 1993, An Aptian-Albian shelf ramp, Arizona and Sonora. P. 71-79.

Scott, R. W., D. G. Benson, R. W. Morin, B. L. Shaffer, and F. E. Oboh-Ikuenobe, 2003, Integrated Albian-lower Cenomanian chronostratigraphy standard, Trinity River section, Texas, *in* US Gulf Coast Cretaceous stratigraphy and paleoecology: Gulf Coast Section, Society of Economic Paleontologists and Mineralogists, Bob F. Perkins Memorial Conference: p. 277–334.

Scott, R.W., A.M. Molineux, H. Loeser, and E.A. Mancini. 2007, Lower Albian sequence stratigraphy and coral buildups; Glen Rose Formation, Texas, U.S.A. In: Cretaceous Rudists and Carbonate Platforms: Environmental Feedback (Ed R.W. Scott) Society for Sedimentary Geology Special Publication, 87: 181-191.

Scott, R.W., W. Schlager, B. Fouke, and S.A. Nederbragt, 2000, Are Mid-Cretaceous Eustatic Events Recorded in Middle East Carbonate Platforms. In: Middle East Models of Jurassic/Cretaceous Carbonate Systems (Eds A.S. Alsharan and R.W. Scott), SEPM Special Publication 69, p 77-88.

Schlager, W., 1981, The paradox of drowned reefs and carbonate platforms: GSA Bulletin, v. 92, no. 4, p. 197–211.

Schlager, W., 1991, Depositional bias and environmental change—important factors in sequence stratigraphy: Sedimentary Geology, v. 70, no. 2–4, p. 109–130.

Schlanger, S. O., and H. C. Jenkyns, 1976, Cretaceous Oceanic Anoxic Events: Causes and Consequences: Geologie en Mijnbouw, v. 55, no. 3–4.

Stramma, L., G. C. Johnson, J. Sprintall, and V. Mohrholz, 2008, Expanding oxygen-minimum zones in the tropical oceans: science, v. 320, no. 5876, p. 655–658.

Stricklin, F.L., Jr., C.I. Smith, F.E. Lozo, 1971, Stratigraphy of Lower Cretaceous Trinity deposits of central Texas. Texas Bureau of Economic Geology Report of Investigations, 71. University of Texas at Austin, Austin, TX, 63 p.

Stricklin, F.L., Jr., and D.L. Amsbury, 2003, Depositional environments on a low-relief carbonate shelf, middle Glen Rose Limestone, central Texas: Geoscience and Man, v. 8, p. 53-66.

Stricklin, F. L., and D. L. Amsbury, 1974, Depositional Environments of a Low-relief Carbonate Shelf, Middle Glen Rose Limestone, Central Texas: School of Geoscience, Louisiana State University.

Taylor, P. D., and M. A. Wilson, 2003, Palaeoecology and evolution of marine hard substrate communities: Earth-Science Reviews, v. 62, no. 1, p. 1–103.

Tribovillard, N., T. J. Algeo, T. Lyons, and A. Riboulleau, 2006, Trace metals as paleoredox and paleoproductivity proxies: An update: Chemical Geology, v. 232, no. 1, p. 12–32.

Vahrenkamp, V. C., F. S. P. Van Buchem, M. I. Al-Husseini, F. Maurer, and H. J. Droste, 2010, Chemostratigraphy of the Lower Cretaceous Shu'aiba Formation: A δ13C reference profile for the Aptian Stage from the southern Neo-Tethys Ocean: Publ, v. 4, no. 1, p. 107–137.

Waite, L. E., 2009, Edwards (Stuart City) shelf margin of south Texas: new data, New Concepts: Tulsa Geological Society.

Ward, W.C. and W.B. Ward, 2007, Stratigraphy of middle part of Glen Rose Formation (Lower Albian), Canyon Lake Gorge, Central Texas, U.S.A. In: Cretaceous Rudists and Carbonate Platforms: Environmental Feedback (Ed R.W. Scott), SEPM Special Publication, 87: p. 193-210.

Weissert, H., A. Lini, K. B. Föllmi, and O. Kuhn, 1998, Correlation of Early Cretaceous carbon isotope stratigraphy and platform drowning events: a possible link? Palaeogeography, Palaeoclimatology, Palaeoecology, v. 137, no. 3–4, p. 189–203.

Wilson, M. A., and T. J. Palmer, 1990, A review of evolutionary trends in carbonate hardground communities: The Paleontological Society Special Publications, v. 5, p. 137–152.

Winker, C. D., and R. T. Buffler, 1988, Paleogeographic evolution of early deep-water Gulf of Mexico and margins, Jurassic to Middle Cretaceous (Comanchean): AAPG bulletin, v. 72, no. 3, p. 318–346.

Wissler, L., H. Funk, and H. Weissert, 2003, Response of Early Cretaceous carbonate platforms to changes in atmospheric carbon dioxide levels: Palaeogeography, Palaeoclimatology, Palaeoecology, v. 200, no. 1–4, p. 187–205.

Wooten, J. W., and W. E. Dunaway, 1977, Lower Cretaceous carbonates of central south Texas: a shelf-margin study.

Young, K., 1986, Cretaceous, marine inundations of the San Marcos platform, Texas: Cretaceous Research, v. 7, no. 2, p. 117–140.

Zhang, W. H., X. Y. Shi, D. J. Tang, and X. Wang, 2014, Mass-occurrence of oncoids in the Early-Middle Cambrian transition at western margin of North China Platform: A response of microbial community to shallow marine anoxia: Journal of Palaeogeography, v. 16, no. 3, p. 305–318.

Zhang, W., X. Shi, G. Jiang, D. Tang, and X. Wang, 2015, Mass-occurrence of oncoids at the Cambrian Series 2–Series 3 transition: Implications for microbial resurgence following an Early Cambrian extinction: Gondwana Research, v. 28, no. 1, p. 432–450.

Zatoń, M., B. Kremer, L. Marynowski, M. A. Wilson, and W. Krawczyński, 2012, Middle Jurassic (Bathonian) encrusted oncoids from the Polish Jura, southern Poland: Facies, v. 58, no. 1, p. 57–77.